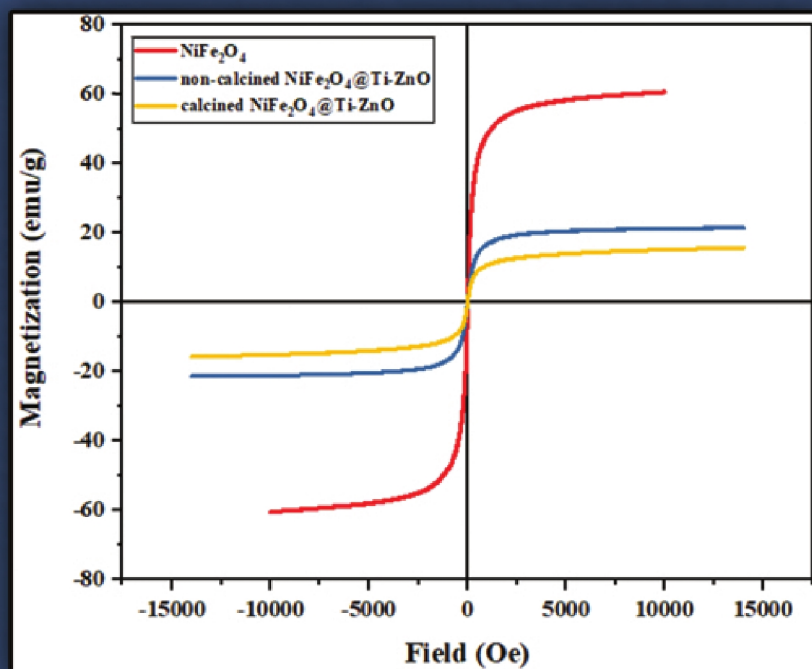


# Advanced Ceramics Progress



Materials and Energy  
Research Center



Iranian Ceramic Society

*In The name of God*

---

# *Advanced Ceramics Progress*

---

## **DIRECTOR-IN-CHARGE**

A. R. Khavandi

## **EDITOR-IN-CHIEF**

M. R. Rahimipour

## **EXECUTIVE MANAGER**

M. Razavi

## **EDITORIAL BOARD**

- |       |   |       |  |
|-------|---|-------|--|
| A. R. | Aghaei, Materials and Energy Research Center        | M. M. | Mohebi, Imam Khomeini University                 |
| P.    | Alizadeh, Tarbiat Modares University                | M. R. | Rahimipour, Materials and Energy Research Center |
| T.    | Ebadzadeh, Materials and Energy Research Center     | M.    | Razavi, Materials and Energy Research Center     |
| M. A. | Faghihi Sani, Sharif University of Technology       | E.    | Salahi, Materials and Energy Research Center     |
| M.    | Ghassemi Kakroudi, University of Tabriz             | M.    | Salehi, Isfahan University of Technology         |
| A. R. | Khavandi, Iran University of Science and Technology | Ş.    | Ţălu, Technical University of Cluj-Napoca        |

## **EDITORIAL ADVISORY BOARD**

F.S. Torknik

## **ENGLISH LANGUAGE EDITOR**

M. Sabzevari

## **TECHNICAL STAFF**

E. Pouladi, V. Hajabdolali, R. Chaluei

## **DISCLAIMER**

The publication of articles in *Advanced Ceramics Progress* does not imply that the editorial board, editorial advisory board, reviewers or the publisher accept, approve or endorse the data and conclusions of authors.

**Advanced Ceramics Progress** (ISSN 2423-7477) (e-ISSN 2423-7485)

Web Site: [www.acerp.ir](http://www.acerp.ir), E-mail: [office@acerp.ir](mailto:office@acerp.ir)

Tel: +98 (0) 26 36280040-7 ext.: 382, Fax: +98 (0) 26 36201888

Tel:+98 (0)21 88771626-7 ext.: 8931, Fax: +98 (0)21 88773352

Materials and Energy Research Center (MERC); Iranian Ceramic Society (ICERS)

## CONTENTS

<b>Zahra Abdi</b> <b>Adrine Malek Khachatourian</b> <b>Ali Nemati</b>	Studying the Effect of Calcination on the Optical and Magnetic Properties of NiFe <sub>2</sub> O <sub>4</sub> @ZnO:Ti Nanoparticles	1-7
<b>Maryam Hajiebrahimi</b> <b>Sanaz Alamdari</b> <b>Omid Mirzaee</b> <b>Mohammad Tajally</b>	Luminescence Investigation of Ce Doped ZnO/CdWO <sub>4</sub> Nanocomposite	8-12
<b>Elmira Sadeghilar</b> <b>Soghra Mirershadi</b> <b>Farhad Sattari</b>	Design and Study of the Photodetection Performance of Photodetector Based on CH <sub>3</sub> NH <sub>3</sub> PbBr <sub>3</sub> Organic-Inorganic Hybrid	13-17
<b>Aida Faeghinia</b> <b>Touradj Ebadzadeh</b>	The Effect of Microwave Settings on HAp Sintering	18-21
<b>Ghader Hosseinzadeh</b>	Preparation of Nanocomposite of TiO <sub>2</sub> Nanoparticles and CuS Nanoflakes for Visible-Light Photocatalytic Decomposition of Nitenpyram Pesticide	22-28
<b>Vali Dalouji</b> <b>Nasim Rahimi</b> <b>Ali Reza Souri</b>	Cu/Co Bilayers: Study of the Surface Topography, Optical Dispersion Parameters, and Transitions of Carriers	29-38





Materials and Energy Research Center

MERC

Contents lists available at [ACERP](#)

Advanced Ceramics Progress

Journal Homepage: [www.acerp.ir](http://www.acerp.ir)

## Original Research Article

# Studying the Effect of Calcination on the Optical and Magnetic Properties of NiFe<sub>2</sub>O<sub>4</sub>@ZnO:Ti Nanoparticles

Zahra Abdi <sup>a</sup>, Adrine Malek Khachatourian <sup>b</sup>, \* Ali Nemati <sup>c</sup><sup>a</sup> MSc, Department of Materials Science and Engineering, Sharif University of Technology, Tehran, Tehran, Iran<sup>b</sup> Assistant Professor, Department of Materials Science and Engineering, Sharif University of Technology, Tehran, Tehran, Iran<sup>c</sup> Professor, Department of Materials Science and Engineering, Sharif University of Technology, Tehran, Tehran, Iran\* Corresponding Author Email: [khachatourian@sharif.edu](mailto:khachatourian@sharif.edu) (A. Malek Khachatourian)URL: [https://www.acerp.ir/article\\_159438.html](https://www.acerp.ir/article_159438.html)

## ARTICLE INFO

## ABSTRACT

## Article History:

Received 22 september 2022

Received in revised form 19 October 2022

Accepted 24 October 2022

## Keywords:

Magnetic Nanoparticles  
Heterogeneous Nucleation  
Hydrothermal Method  
Band Gap Engineering  
Saturation Magnetization

In this study, novel magnetically separable NiFe<sub>2</sub>O<sub>4</sub>@ZnO:Ti nanospheres were synthesized using the heterogeneous nucleation of ZnO:Ti (Ti-doped ZnO) nanoparticles on NiFe<sub>2</sub>O<sub>4</sub> polycrystalline nanospheres through the hydrothermal method. Structural and microstructural properties of the synthesized polycrystalline nanospheres were investigated through Fourier-Transform Infrared Spectra (FTIR), X-Ray Diffraction (XRD), Transmission Electron Microscopy (TEM), and Field Emission Scanning Electron Microscopy (FESEM) using an Energy-Dispersive X-ray (EDX) spectrometer. The effect of calcination on the magnetic and optical properties was also studied. The optical features of the synthesized nanoparticles were recorded using UV-Vis spectroscopy, indicating the absorption peak in the visible region. The band gap energy of pure ZnO, ZnO:Ti, and NiFe<sub>2</sub>O<sub>4</sub>@ZnO:Ti before and after calcination was calculated as 3.21 eV, 2.92 eV, 2.44 eV, and 2.04 eV, respectively. Further, Vibrating Sample Magnetometer (VSM) was employed to examine the magnetic features, and the saturation magnetization (Ms) values of NiFe<sub>2</sub>O<sub>4</sub> and NiFe<sub>2</sub>O<sub>4</sub>@ZnO:Ti non-calcined and calcined were obtained as 63.6 emu/g, 21.3 emu/g, and 15.3 emu/g, respectively. The findings revealed that calcination of NiFe<sub>2</sub>O<sub>4</sub>@ZnO:Ti nanospheres improved the optical properties and reduced the band gap energy. However, NiFe<sub>2</sub>O<sub>4</sub> combination with nonmagnetic matrix and calcination of NiFe<sub>2</sub>O<sub>4</sub>@ZnO:Ti nanoparticles decreased the Ms value and response to the external magnetic field.

<https://doi.org/10.30501/acp.2022.363261.1101>

## 1. INTRODUCTION

Considerable attention has been recently drawn to semiconductor nanomaterials and spinel ferrite nanocrystals due to their wide applications such as photocatalytic degradation of dyes, photoelectric devices, adsorption-membrane filtration, and sensors due to their excellent optical and magnetic features [1,2]. A remarkable semiconductor, Zinc oxide (ZnO), has been

frequently used in recent years due to its high potential of charge carriers between the conduction band and valence band under light energy. Nevertheless, the wide band gap energy (~ 3.37 eV) and excitation under UV radiation that forms only about 10 percent of solar light are significant drawbacks of ZnO nanoparticles [3,4]. Many strategies, namely doping different atoms and coupling with other compounds, were suggested to improve the optical properties of these nanoparticles. Doping

Please cite this article as: Abdi, Z., Malek Khachatourian, A., Nemati, A., "Studying the Effect of Calcination on the Optical and Magnetic Properties of NiFe<sub>2</sub>O<sub>4</sub>@ZnO:Ti Nanoparticles", *Advanced Ceramics Progress*, Vol. 8, No. 3, (2022), 1-7. <https://doi.org/10.30501/acp.2022.363261.1101>

2423-7485/© 2022 The Author(s). Published by MERC.

This is an open access article under the CC BY license (<https://creativecommons.org/licenses/by/4.0/>).

transition metals such as Fe, Ni, and Cu into the ZnO crystal structure reduces the band gap energy level and modifies the electronic structure. When the nanomaterials like CuO, CeO<sub>2</sub>, and ZnFe<sub>2</sub>O<sub>4</sub> couple with ZnO nanoparticles, a new band gap energy level is formed for easy separation of photoinduced electrons in the visible light region [5-9]. Spinel ferrite MFe<sub>2</sub>O<sub>4</sub> (M = Mn, Fe, Co, Ni, ...) nanomaterials with high chemical stability and large surface area are characterized by remarkable superparamagnetic properties [10-12]. In addition, coupling spinel ferrite nanomaterials with semiconductors help reduce the band gap energy and easy separation of catalysts under an external magnetic field. Garima Vaish et al. [13]. synthesized MgFe<sub>2</sub>O<sub>4</sub>/TiO<sub>2</sub> nanocomposites using the economic ultra-sonication method and identified appropriate magnetic and optical properties for magnetic, photocatalytic, and optoelectronic devices.

The present study aimed to synthesize novel magnetic NiFe<sub>2</sub>O<sub>4</sub>@ZnO:Ti nanoparticles using an in-situ hydrothermal method and evaluate the effects of calcination on nanocomposite optical and magnetic properties. Monodisperse spherical NiFe<sub>2</sub>O<sub>4</sub> nanoparticles exhibit high water solubility and large saturation magnetization (Ms) due to Polyacrylamide (PAM) as a hydrophilic polymer in the hydrothermal process. Doping titanium atoms modify the band gap energy of ZnO nanoparticles. Further, coupling ZnO:Ti (Ti-doped ZnO) nanoparticles with NiFe<sub>2</sub>O<sub>4</sub> nanospheres improves the optical properties and exhibits magnetic properties. Subsequently, magnetic and optical features of NiFe<sub>2</sub>O<sub>4</sub>@ZnO:Ti nanospheres were studied before and after calcination at 500 °C by UV-Vis spectroscopy and VSM analysis.

## 2. MATERIALS AND METHODS

### 2.1. Materials

Nickel (II) chloride (NiCl<sub>2</sub>·6H<sub>2</sub>O), PAM, Mn=150000 (C<sub>3</sub>H<sub>5</sub>NO)<sub>n</sub>, iron (III) chloride (FeCl<sub>3</sub>·6H<sub>2</sub>O), sodium citrate (Na<sub>3</sub>C<sub>6</sub>H<sub>5</sub>O<sub>7</sub>·2H<sub>2</sub>O), urea (CH<sub>4</sub>N<sub>2</sub>O), and ethanol (C<sub>2</sub>H<sub>6</sub>O) were purchased from Merck Company (Germany) to prepare NiFe<sub>2</sub>O<sub>4</sub> nanoparticles. Potassium hydroxide (KOH), methanol (CH<sub>3</sub>OH), zinc acetate dihydrate (Zn(CH<sub>3</sub>COO)<sub>2</sub>·2H<sub>2</sub>O), and Titanium Isopropoxide (TTIP) (C<sub>12</sub>H<sub>28</sub>O<sub>4</sub>Ti) were also bought from Merck Company to fabricate ZnO:Ti nanoparticles.

### 2.2. Synthesis of NiFe<sub>2</sub>O<sub>4</sub>

The super-paramagnetic NiFe<sub>2</sub>O<sub>4</sub> nanoparticles were synthesized through a modified hydrothermal method [14]. FeCl<sub>3</sub>·6H<sub>2</sub>O (1 mmol) and NiCl<sub>2</sub>·6H<sub>2</sub>O (0.5 mmol) were added into 40 mL distilled water. Then, sodium citrate (3 mmol), urea (6 mmol), and PAM (0.3 g) were dissolved in the resultant solution, respectively. The green obtained solution was stirred continuously until

PAM was entirely disintegrated. After a specific time, the resulting solution was poured into a Teflon-lined autoclave and maintained for 12 hours in an oven at 200 °C. Then, the brownish solution was centrifuged, washed several times with ethanol and distilled water, and left in an oven at 60 °C for three hours.

### 2.3. Synthesis of NiFe<sub>2</sub>O<sub>4</sub>@ZnO:Ti Nanoparticles

A hydrothermal technique was employed to fabricate NiFe<sub>2</sub>O<sub>4</sub>@ZnO:Ti nanospheres. In a typical preparation, zinc acetate dihydrate (1.25 mmol) was dispersed in 40 mL methanol, and potassium hydroxide (2 mmol) was added to this solution to adjust pH = 8. Then, 7.5 wt. % of TTIP was put into the solution and stirred vigorously. Next, 0.04 g of the as-prepared magnetic NiFe<sub>2</sub>O<sub>4</sub> nanoparticles was sonicated and poured into the above solution. The mixture was refluxed for five hours at 70 °C. Once the reaction was completed, the obtained solution was hydrothermally processed in a Teflon-lined stainless-steel autoclave for 12 hours at 180 °C. The synthetic powders were gathered by centrifugation, washed several times with deionized water (DI), and maintained in an oven at 60 °C. Of note, ZnO and ZnO:Ti nanoparticles were also synthesized without a NiFe<sub>2</sub>O<sub>4</sub> core with the same method as that used for the reference powders.

### 2.4. Characterization

The X-Ray Diffraction (XRD) patterns of the powder were obtained using a multipurpose X-ray diffractometer (PANalytical X'Pert Pro MPD) with Cu K<sub>α</sub> radiation (λ = 1.5406 Å). In addition, Fourier-Transform Infrared spectroscopy (FTIR; Perkin Elmer-Spectrum 65) was employed to study the functional groups of the samples. The microstructure and chemical composition of the samples were investigated using (TEM; Philips EM208S-100 kV) and (FE-SEM; TESCAN company, MIRA3) with an Energy-Dispersive X-ray Spectrometer (EDS). The magnetic features were evaluated by a vibrating sample magnetometer (VSM; MDK company). In addition, a UV-Vis spectrophotometer (JENWAY 6705) was utilized to assess the optical properties.

## 3. RESULTS AND DISCUSSION

### 3.1. XRD Analysis

Fig. 1 depicts the XRD patterns of ZnO, ZnO:Ti, NiFe<sub>2</sub>O<sub>4</sub>, and NiFe<sub>2</sub>O<sub>4</sub>@ZnO:Ti nanoparticles to study the crystalline structure and phase identification. In the XRD pattern of pure ZnO (Fig. 1a), the diffraction peaks were observed at 2θ = 31.8°, 34.5°, 36.3°, 47.6°, 56.7°, 62.9°, 66.4°, 68.0°, and 69.2° attributed to (100), (002), (101), (102), (110), (103), (200), (112), and (201) crystal planes of typical hexagonal wurtzite phase (JCPDS file no. 36-1451) [15]. After doping Ti, the same peaks were detected in the XRD pattern of ZnO:Ti, and insignificant

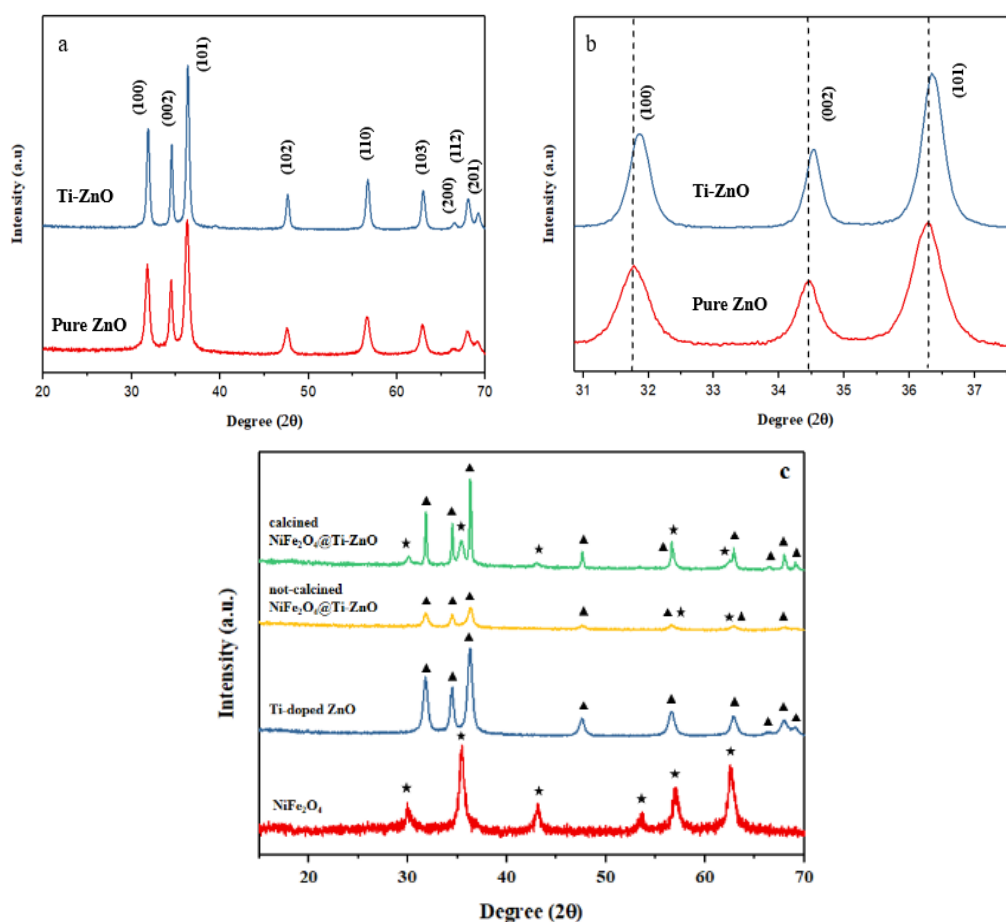


**Figure 1.** XRD patterns of (a-b) pure ZnO and ZnO:Ti, and (c) non-calcined and calcined NiFe<sub>2</sub>O<sub>4</sub>@ZnO:Ti

peak shifting occurred due to the diversity of the ionic radius between Ti<sup>4+</sup> (0.068 nm) and Zn<sup>2+</sup> (0.074 nm) (Fig. 1b). As demonstrated in Fig. 1c, the diffraction peaks of NiFe<sub>2</sub>O<sub>4</sub> revealed 2θ = 29.9°, 35.4°, 43.2°, 53.5°, 56.8°, 62.7° refer to (220), (311), (400), (422), (511), and (440) crystal planes, thus proving the formation of pure spinel phase (JCPDS file no. 19-0629) [16]. Further, the mean grain sizes (D) of ZnO, ZnO:Ti, and NiFe<sub>2</sub>O<sub>4</sub> nanoparticles were measured through the Scherrer equation [17]:

$$D = \frac{k\lambda}{\beta \cos \theta} \quad (1)$$

where k denotes the shape factor whose value was measured as approximately 0.9, λ the wavelength of X-ray, θ the Bragg's diffraction angle, and β the diffraction peak width at the half maximum (FWHM). Table. 1 lists the obtained grain sizes of the powders. The XRD pattern of NiFe<sub>2</sub>O<sub>4</sub>@ZnO:Ti nanoparticles (Fig. 1c) shows the same diffraction peaks of the NiFe<sub>2</sub>O<sub>4</sub> and ZnO:Ti nanoparticles without any extra peaks, thus confirming the thorough formation of NiFe<sub>2</sub>O<sub>4</sub>@ZnO:Ti

nanospheres. However, in the XRD pattern of the calcined NiFe<sub>2</sub>O<sub>4</sub>@ZnO:Ti, the diffraction peaks of NiFe<sub>2</sub>O<sub>4</sub> and ZnO:Ti appeared distinctly with higher intensity than that of the peaks of non-calcined nanoparticles.

### 3.2. FTIR Analysis

The functional groups of NiFe<sub>2</sub>O<sub>4</sub>, ZnO:Ti, and NiFe<sub>2</sub>O<sub>4</sub>@ZnO:Ti nanoparticles were assessed using the FTIR spectroscopy (Fig. 2). For all the prepared samples spectra, the O–H stretching vibration band appeared at about 3400 cm<sup>-1</sup>. In the FTIR spectrum of NiFe<sub>2</sub>O<sub>4</sub>, Fe–O stretching at 595 cm<sup>-1</sup>, NH<sub>2</sub> deformation bands at 1656 cm<sup>-1</sup>, and CH<sub>2</sub> deformation band at 1410 cm<sup>-1</sup> were detected that were attributed to the presence of the PAM in the process of synthesis [18]. The characteristic peak at 526 cm<sup>-1</sup> is relevant to the Zn–O stretching band, and the main characteristic peaks at 1348 cm<sup>-1</sup>, 1419 cm<sup>-1</sup>, and 1626 cm<sup>-1</sup> related to the C=O mode of zinc acetate were observed in the FTIR spectrum of ZnO:Ti [19]. Eventually, all the characteristic peaks of NiFe<sub>2</sub>O<sub>4</sub> and ZnO:Ti nanoparticles appeared in the non-calcined NiFe<sub>2</sub>O<sub>4</sub>@ZnO:Ti spectrum.

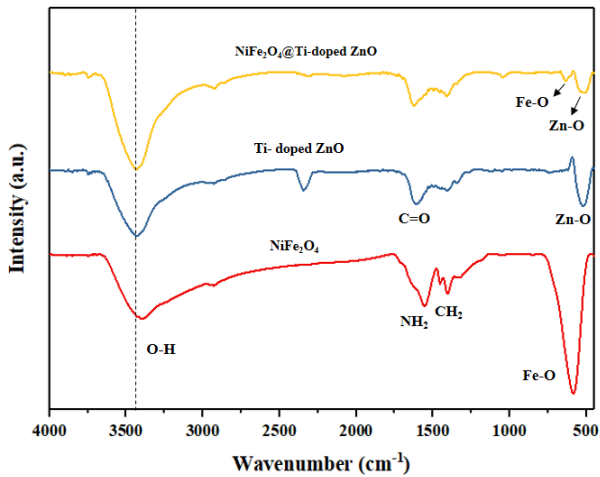


**Figure 2.** FTIR spectrum of  $\text{NiFe}_2\text{O}_4$ ,  $\text{ZnO:Ti}$ , and non-calcined  $\text{NiFe}_2\text{O}_4@\text{ZnO:Ti}$

### 3.3. Microstructure Analysis

The microstructure, chemical composition, and surface morphology of the as-prepared samples were analyzed using FE-SEM and EDS analyses. As shown in Fig. 3a,

the  $\text{ZnO:Ti}$  nanoparticles are characterized by similar spherical morphology with the mean particle size of 27 nm. The FESEM images of  $\text{NiFe}_2\text{O}_4$  (Fig. 3b) indicated well-distribution spherical nanoparticles with the mean particle size of 200 nm. In addition, the presence of PAM and citrate in the hydrothermal process led to the formation of monodisperse nanospheres and prevented random aggregation of  $\text{NiFe}_2\text{O}_4$  nanoparticles. Fig. 3c vividly illustrates the deposition of  $\text{ZnO:Ti}$  nanoparticles into the  $\text{NiFe}_2\text{O}_4$  nanospheres and coarsening of its surface. Moreover, the particle size of non-calcined  $\text{NiFe}_2\text{O}_4@\text{ZnO:Ti}$  increased up to around 230 nm. As demonstrated in Fig. 4, the FESEM e-maps of the Energy-Dispersive X-ray spectroscopy (EDS) of non-calcined  $\text{NiFe}_2\text{O}_4@\text{ZnO:Ti}$  proved the presence of Ni, Fe, O, Zn, and Ti with homogeneous distribution.

The EDS spectra of the sample also confirmed the presence of K atoms that attribute to KOH to adjust the pH. The clear morphological images of non-calcined  $\text{NiFe}_2\text{O}_4@\text{ZnO:Ti}$  nanoparticles were included in the TEM analysis (Fig. 5). The TEM images of powders confirmed the growth of a thin layer of  $\text{ZnO:Ti}$  nanoparticles on the polycrystalline spherical  $\text{NiFe}_2\text{O}_4$  nanoparticles.

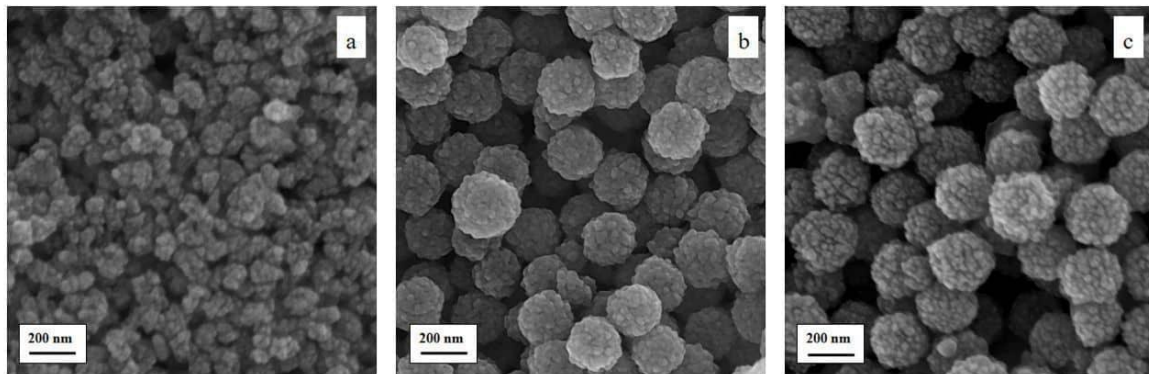


**Figure 3.** FE-SEM images of (a)  $\text{ZnO:Ti}$  (b)  $\text{NiFe}_2\text{O}_4$ , and (c) non-calcined  $\text{ZnO:Ti}@\text{NiFe}_2\text{O}_4$

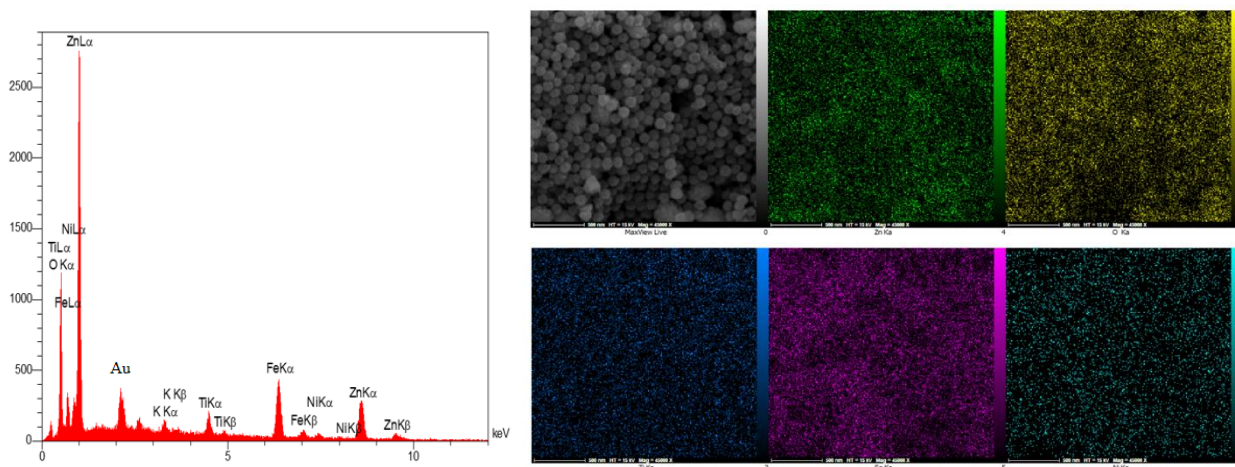


**Figure 4.** EDS spectrum and elemental mapping of non-calcined  $\text{ZnO:Ti}@\text{NiFe}_2\text{O}_4$

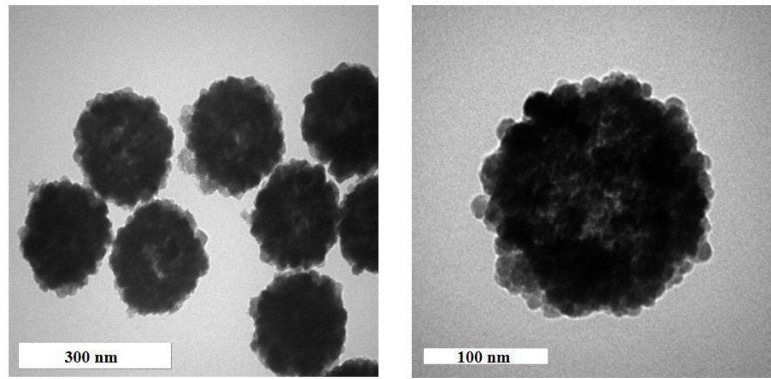


**Figure 5.** TEM images of non-calcined ZnO:Ti@NiFe<sub>2</sub>O<sub>4</sub> nanoparticles

### 3.4. UV-Vis Analysis

The optical features of ZnO, ZnO:Ti, and non-calcined and calcined NiFe<sub>2</sub>O<sub>4</sub>@ZnO:Ti nanoparticles were investigated using UV-Vis spectrometry. As shown in Fig. 6a, pure ZnO can be simulated in the ultraviolet region at 385 nm. However, the absorption peak of ZnO:Ti nanoparticles tuned to the visible region at 456 nm. For NiFe<sub>2</sub>O<sub>4</sub>@ZnO:Ti nanoparticles before and after calcination, the absorption peaks have redshift to the visible region at about 500 nm. The optical bandgap

energy ( $E_g$ ) of the samples was obtained using Tauc relation [20]:

$$(\alpha h\nu)^2 = A(h\nu - E_g) \quad (2)$$

where  $h\nu$  stands for the photon energy,  $\alpha$  the absorption coefficient, and  $A$  a constant. Fig. 6b illustrates the plot of  $(\alpha h\nu)^2$  as a function of  $h\nu$ . The band gap value of ZnO decreased after doping Ti, coupling with NiFe<sub>2</sub>O<sub>4</sub>, and calcination at 500 °C (as summarized in Table. 1).

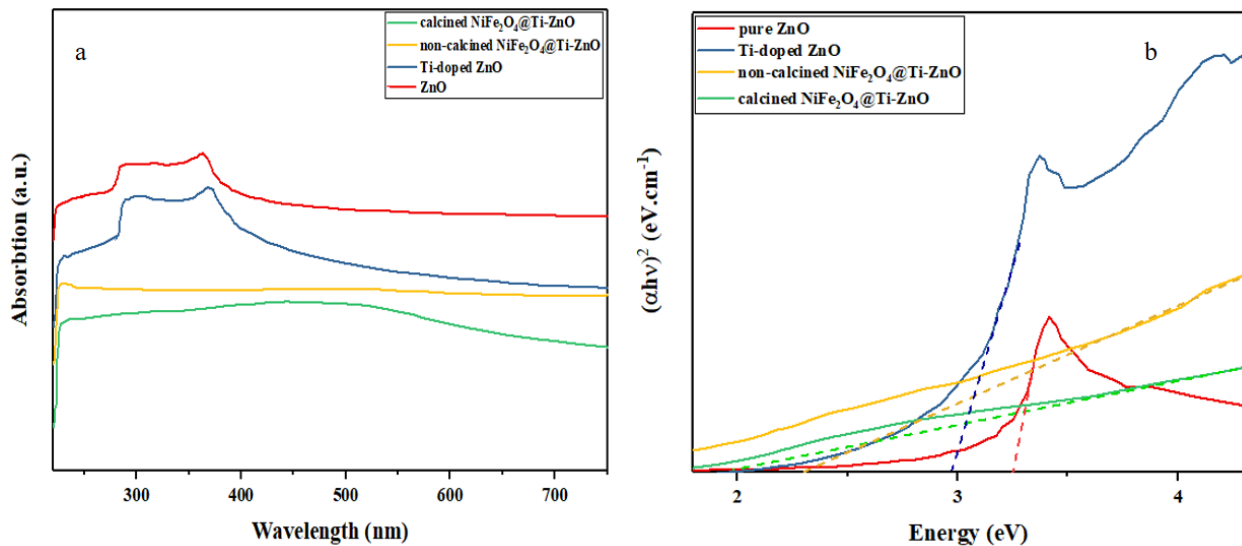


**Figure 6.** (a) UV-Vis spectrum and (b) Kubelka-Munk plots of samples

**TABLE 1.** Crystallite size (D), Particle size, Bandgap energies, Ms

Samples	Crystallite Size (nm)		Particle Size (nm)		Band Gap (eV)		Ms (emu/g)	
	XRD		SEM		UV-Visible Spectra		VSM	
NiFe <sub>2</sub> O <sub>4</sub>	11		200		-		63.6	
Pure ZnO	27		38		3.21		-	
Ti-Doped ZnO	14		27		2.92		-	
Non-Calcined NiFe <sub>2</sub> O <sub>4</sub> @Ti-doped ZnO	-		230		2.44		21.3	
Calcined NiFe <sub>2</sub> O <sub>4</sub> @Ti-doped ZnO	-		-		2.04		15.3	

According to the results, the bandgap of  $\text{NiFe}_2\text{O}_4@ZnO:\text{Ti}$  nanoparticles after calcination reached 2.04 eV. Of note, calcination significantly decreased the band gap energy because of the improvement in the substantial oxygen vacancy defects.

### 3.5. VSM Analysis

The magnetic features of  $\text{NiFe}_2\text{O}_4$ , non-calcined  $\text{NiFe}_2\text{O}_4@ZnO:\text{Ti}$ , and calcined  $\text{NiFe}_2\text{O}_4@ZnO:\text{Ti}$  were recorded using VSM analysis. Fig. 7 shows the magnetic hysteresis curves of all samples with no coercivity or definite remnant magnetization that exhibits superparamagnetic behavior at room temperature.

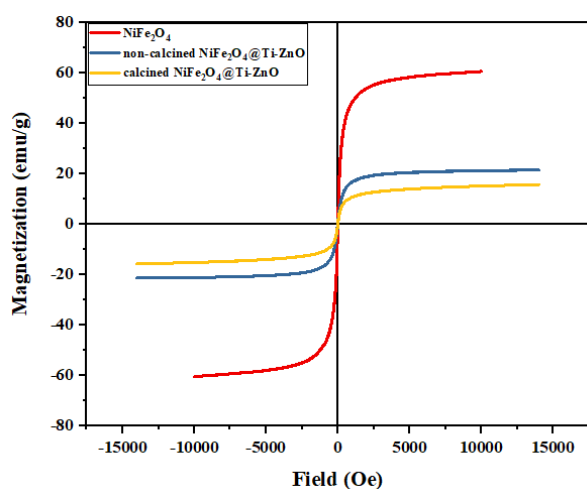


**Figure 7.** Magnetic hysteresis loops of the samples

Pure  $\text{NiFe}_2\text{O}_4$  nanoparticles are characterized by a high  $M_s$  value of 63.6 emu/g (applied field sweeping from  $-10$  K to  $10$  K Oe) due to their small crystallite size. Furthermore,  $\text{NiFe}_2\text{O}_4$  composition with  $ZnO:\text{Ti}$  as a non-magnetic material decreased  $M_s$  value to 21.3 emu/g (applied field sweeping from  $-15$  K to  $15$  K Oe). As a result of calcination on the magnetic features of  $\text{NiFe}_2\text{O}_4@ZnO:\text{Ti}$  nanoparticles, the  $M_s$  value was reduced by 15.1 emu/g (applied field sweeping from  $-15$  K to  $15$  K Oe) due to the increasing crystallite size, non-uniform particle distribution, and decreasing the surface to volume ratio.

## 4. CONCLUSION

The magnetically separable  $\text{NiFe}_2\text{O}_4@ZnO:\text{Ti}$  nanoparticles were successfully synthesized using one-step hydrothermal methods. The optical and magnetic features of the prepared samples were examined through the UV-Vis analysis, Kubelka-Munk plots, and VSM analysis. The  $\text{NiFe}_2\text{O}_4@ZnO:\text{Ti}$  nanoparticles can be excited in the visible region. Additionally, the band gap

value of pure  $ZnO$  decreased from 3.21 eV to 2.44 eV for  $\text{NiFe}_2\text{O}_4@ZnO:\text{Ti}$  nanoparticles. Improvement in the optical properties in the visible region and decrease in the band gap energy value by 2.04 eV were noticed followed by calcination of  $\text{NiFe}_2\text{O}_4@ZnO:\text{Ti}$ . In addition, the  $M_s$  value of superparamagnetic  $\text{NiFe}_2\text{O}_4$  reduced from 63.6 emu/g to 15.1 emu/g after coupling with  $ZnO:\text{Ti}$  and calcination at  $500^\circ\text{C}$ . However, the as-prepared nanoparticles exhibited an appropriate response to the external magnetic field.

It should be noted that  $\text{NiFe}_2\text{O}_4@ZnO:\text{Ti}$  nanoparticles exhibited proper photocatalytic performance, hence widely used in environmental applications and wastewater treatment. Moreover, the composition of these nanoparticles with graphene and different polymers could improve the photocatalytic activity under visible light.

## ACKNOWLEDGEMENTS

The authors would like to acknowledge Sharif University of Technology for supporting this research.

## NOMENCLATURE

$\alpha$	Absorption coefficient
A	A constant
$\beta$	Diffraction peak width at half maximum (FWHM)
D	Average grain size
$E_g$	Optical bandgap energy
Eq.	Equation
$h\nu$	Photon energy
k	Shape factor
$M_s$	Saturation magnetization
$\theta$	Natural logarithm of MSW generation
$\lambda$	Natural logarithm of population

## REFERENCES

- Reddy, D. H. K., Yun, Y. S., "Spinel ferrite magnetic adsorbents: alternative future materials for water purification?", *Coordination Chemistry Reviews*, Vol. 315, (2016), 90-111. <https://doi.org/10.1016/j.ccr.2016.01.012>
- Terna, A. D., Elemike, E. E., Mbonu, J. I., Osafire, O. E., Ezeani, R. O., "The future of semiconductors nanoparticles: Synthesis, properties and applications", *Materials Science and Engineering: B*, Vol. 272, (2021), 115363. <https://doi.org/10.1016/j.mseb.2021.115363>
- Caglar, M., Ilican, S., Caglar, Y., Yakuphanoglu, F., "Electrical conductivity and optical properties of  $ZnO$  nanostructured thin film.", *Applied Surface Science*, Vol. 255, No. 8, (2009), 4491-4496. <https://doi.org/10.1016/j.apsusc.2008.11.055>
- Noman, M. T., Amor, N., Petru, M., "Synthesis and applications of  $ZnO$  nanostructures (ZONSs): a review", *Critical Reviews in Solid State and Materials Sciences*, Vol. 47, No. 2, (2022), 99-141. <https://doi.org/10.1080/10408436.2021.1886041>
- Kayani, Z. N., Abbas, E., Saddiqe, Z., Riaz, S., Naseem, S., "Photocatalytic, antibacterial, optical and magnetic properties of Fe-doped  $ZnO$  nano-particles prepared by sol-gel", *Materials*

- Science in Semiconductor Processing*, Vol. 88, (2018), 109-119. <https://doi.org/10.1016/j.mssp.2018.08.003>
6. Karthik, K. V., Raghu, A. V., Reddy, K. R., Ravishankar, R., Sangeeta, M., Shetti, N. P., Reddy, C. V., "Green synthesis of Cu-doped ZnO nanoparticles and its application for the photocatalytic degradation of hazardous organic pollutants", *Chemosphere*, Vol. 287, (2022), 132081. <https://doi.org/10.1016/j.chemosphere.2021.132081>
  7. Zhang, Q., Zhao, X., Libing, D., Shen, H., Liu, R., "Controlling oxygen vacancies and enhanced visible light photocatalysis of CeO<sub>2</sub>/ZnO nanocomposites", *Journal of Photochemistry and Photobiology A: Chemistry*, Vol. 392, (2020), 112156. <https://doi.org/10.1016/j.jphotochem.2019.112156>
  8. Ahmed, A. A. A., Abdulwahab, A. M., Talib, Z. A., Salah, D., Flaifel, M. H., "Magnetic and optical properties of synthesized ZnO-ZnFe<sub>2</sub>O<sub>4</sub> nanocomposites via calcined Zn-Fe layered double hydroxide", *Optical Materials*, Vol. 108, (2020), 110179. <https://doi.org/10.1016/j.optmat.2020.110179>
  9. Khosravi, M. D., Ghahari, M., Shafiee Afarani, M., Arabi, A. M., "Synthesis of CuO and CuO/ZnO Composite Powders for Antibacterial, Photocatalytic, and Pigment-Related Applications", *Advanced Ceramics Progress*, Vol. 8, No. 1, (2022), 1-8. <https://doi.org/10.30501/acp.2022.329820.1082>
  10. Wang, L., Li, J., Wang, Y., Zhao, L., Jiang, Q., "Adsorption capability for Congo red on nanocrystalline MFe<sub>2</sub>O<sub>4</sub> (M = Mn, Fe, Co, Ni) spinel ferrites", *Chemical Engineering Journal*, Vol. 181, (2012), 72-79. <https://doi.org/10.1016/j.cej.2011.10.088>
  11. Amirimehr, A., Ghasemi, E., Fazlali, A., "Rheological Study of Nickel Ferrite Ferrofluid", *Advanced Ceramics Progress*, Vol. 1, No. 2, (2015), 29-33. <https://doi.org/10.30501/acp.2015.90745>
  12. Mmesele, O. K., Masunga, N., Kuvarega, A., Nkambule, T. T., Mamba, B. B., Kefeni, K. K., "Cobalt ferrite nanoparticles and nanocomposites: Photocatalytic, antimicrobial activity and toxicity in water treatment", *Materials Science in Semiconductor Processing*, Vol. 123, (2021), 105523. <https://doi.org/10.1016/j.mssp.2020.105523>
  13. Vaish, G., Kripal, R., Kumar, L., "Comprehensive study of magnetic and optoelectronic properties of MgFe<sub>2</sub>O<sub>4</sub>-TiO<sub>2</sub> nanocomposites", *Materials Chemistry and Physics*, Vol. 271, (2021), 124911. <https://doi.org/10.1016/j.matchemphys.2021.124911>
  14. Cheng, W., Tang, K., Sheng, J., "Highly Water-Soluble Superparamagnetic Ferrite Colloidal Spheres with Tunable Composition and Size", *Chemistry-A European Journal*, Vol. 16, No. 12, (2010), 3608-3612. <https://doi.org/10.1002/chem.201000014>
  15. Hong, R., Pan, T., Qian, J., Li, H., "Synthesis and surface modification of ZnO nanoparticles", *Chemical Engineering Journal*, Vol. 119, No. 2-3, (2006), 71-81. <https://doi.org/10.1016/j.cej.2006.03.003>
  16. Fu, L. S., Xu, C. Y., Wang, W. S., Jiang, J. T., Zhen, L., "Superparamagnetic nickel ferrite colloidal spheres for constructing magnetically responsive photonic crystals", *Materials Letters*, Vol. 81, (2012), 62-64. <https://doi.org/10.1016/j.matlet.2012.04.139>
  17. Patterson, A. L., "The Scherrer Formula for X-Ray Particle Size Determination", *Physical Review*, Vol. 56, No. 10, (1939), 978-982. <https://doi.org/10.1103/PhysRev.56.978>
  18. Leshuk, T., Krishnakumar, H., Gu, F., "Size-tunable Fe<sub>3</sub>O<sub>4</sub> spherical nanoclusters through a one-pot hydrothermal synthesis", *Journal of Nanoscience and Nanotechnology*, Vol. 15, No. 7, (2015), 5378-5383. <https://doi.org/10.1166/jnn.2015.9003>
  19. Vijayaprasath, G., Murugan, R., Mahalingam, T., Ravi, G., "Comparative study of structural and magnetic properties of transition metal (Co, Ni) doped ZnO nanoparticles", *Journal of Materials Science: Materials in Electronics*, Vol. 26, No. 9, (2015), 7205-7213. <https://doi.org/10.1007/s10854-015-3346-z>
  20. Ebrahimi, S., Yarmand, B., Naderi, N., "Effect of the Sulfur Concentration on the Optical Band Gap Energy and Urbach Tail of Spray-Deposited ZnS Films", *Advanced Ceramics Progress*, Vol. 3, No. 4, (2017), 6-12. <https://doi.org/10.30501/acp.2017.90759>



Materials and Energy Research Center

MERC

Contents lists available at ACERP

Advanced Ceramics Progress

Journal Homepage: [www.acerp.ir](http://www.acerp.ir)

## Original Research Article

Luminescence Investigation of Ce Doped ZnO/CdWO<sub>4</sub> NanocompositeMaryam Hajiebrahimi <sup>a</sup>, Sanaz Alamdari <sup>b</sup>, \*, Omid Mirzaee <sup>c</sup>, \*, Mohammad Tajally <sup>d</sup><sup>a</sup> MSc Student, Faculty of Materials and Metallurgical Engineering, Semnan University, Semnan, Semnan, Iran<sup>b</sup> Assistant Professor, Department of Nano Electronics, Faculty of Nanotechnology, Semnan University, Semnan, Semnan, Iran<sup>c</sup> Professor, Department of Ceramic, Faculty of Materials and Metallurgical Engineering, Semnan University, Semnan, Semnan, Iran<sup>d</sup> Associate Professor, Department of Industrial Metallurgy, Faculty of Materials and Metallurgical Engineering, Semnan University, Semnan, Semnan, Iran\* Corresponding Authors' Emails: [s.alamdari@semnan.ac.ir](mailto:s.alamdari@semnan.ac.ir) (S. Alamdari); [o\\_mirzaee@semnan.ac.ir](mailto:o_mirzaee@semnan.ac.ir) (O. Mirzaee)URL: [https://www.acerp.ir/article\\_159415.html](https://www.acerp.ir/article_159415.html)

## ARTICLE INFO

## ABSTRACT

## Article History:

Received 22 September 2022

Received in revised form 1 October 2022

Accepted 24 October 2022

## Keywords:

ZnO  
CdWO<sub>4</sub>  
Ce Dopant  
Nanocomposite  
Emission  
Optical Response

Novel luminous materials are always required in solid-state light-emitting diodes and displays applications. In this regard, the current study investigated the luminescence properties of cerium-doped zinc oxide/cadmium tungstate (ZnO/CdWO<sub>4</sub>: Ce) nanocomposite particles under proton, laser, and gamma-ray excitations. The XRD results revealed the simultaneous existence of monoclinic CWO and hexagonal ZnO. Doped nanocomposite particles under proton/laser irradiations displayed significant luminescence in the blue-green region compared with the pure nanocomposite. In addition, Thermo-Luminescence (TL) study of the doped pellet showed a stronger glow peak at 350-400 °C. According to the TEM, the doped nanoparticles had an average diameter of 70-150 nanometers. The existence of Zn, O, Cd, W, and Ce elements in the composites was confirmed by the EDX technique. The obtained results showed that the produced ZnO/CWO: Ce nanocomposite particles could be promising materials to be used in optoelectronic devices.

<https://doi.org/10.30501/acp.2022.363264.1102>

## 1. INTRODUCTION

Luminescent materials have drawn considerable attention owing to their applications in photonic, displays, and screen devices. Within this energy sphere, it is recommended that a wide range of insulators be used with the band gaps that are doped with optically active ions capable of emitting a visible luminescence with high quantum efficiency for all excited phosphors [1,2]. Luminescent materials may take up energy and then

release it as light. The process is called excitation and emission. The nature of the luminous substance is fixed by the physical form of the excitation energy. Many materials are able to both absorb and release different types of energy. In other words, they have the potential to serve in a variety of luminous media. Doping and modifications of the energy level structure in metal oxides are performed to enhance the optical behavior, hence desirable outcome. For instance, ZnO and CdWO<sub>4</sub> (CWO) are two oxide materials that have wide

Please cite this article as: Hajiebrahimi, M., Alamdari, S., Mirzaee, O., Tajally, M., "Luminescence Investigation of Ce Doped ZnO/CdWO<sub>4</sub> Nanocomposite", *Advanced Ceramics Progress*, Vol. 8, No. 3, (2022), 8-12. <https://doi.org/10.30501/acp.2022.363264.1102>

2423-7485/© 2022 The Author(s). Published by MERC.

This is an open access article under the CC BY license (<https://creativecommons.org/licenses/by/4.0/>).

applications in different industries [3-7]. Compared to the single structures, mixed oxide materials are characterized by different features due to the newly produced luminescence centers or defects. Although numerous studies have been conducted on ZnO and CWO nanostructures, only a few studies focused on the luminescence properties of ZnO/CWO [9-18]. Given that, the current study aims to prepare flexible scintillation Ce doped ZnO/CWO nanocomposite films and investigate ionization radiation sensitivity and photocurrent responses (under UV/alpha ray) [14]. In addition, this research discusses the luminescence properties of Ce doped ZnO/CdWO<sub>4</sub> nanocomposite particles under laser and gamma irradiation prepared through a simple method for photonic applications.

## 2. MATERIALS AND METHODS

Cadmium nitrate, ethylene glycol, sodium tungstate triethanolamine, sodium tungstate dihydrate, ethanol zinc acetate dihydrate, citric acid (99 %), (98 %), and cerium (III) nitrate hexahydrate were purchased from Merck and Sigma-Aldrich (99.99 % purity). First, ZnO NPs were synthesized via the sol-gel method, taking into account the instructions given in our previous work [10-13]. Then, CdWO<sub>4</sub> NPs were synthesized through the coprecipitation method [16]. Next, 25 cc of ethylene glycol was added to five grams of ZnO NPs containing 6.3 g of citric acid and deionized water. The synthesized CWO powder (1:1 ratio to ZnO) and cerium nitrate (2 at. %) were then added to the suspension, stirred again for three hours, and calcined at 600 ° C for four hours. Using a <sup>60</sup>Co gamma source, Thermo-Luminescence (TL) glow curve was recorded using a TLD reader for the prepared nanocomposite pellets. The luminescence characteristics of the nanocomposite were examined using a CW Nd: YAG laser excitation (1064 nm) linked to a focusing lens and a spectrometer. The produced nanocomposite particles were subjected to focused microbeam irradiation of protons with the energy of 2.2 MeV and current of 4 nA linked to the fluorescence spectrometer to assess Ion Beam-Induced Luminescence (IBIL).

## 3. RESULTS AND DISCUSSION

Figure 1 demonstrates the XRD pattern of the ZnO/CWO: Ce nanocomposite. According to the standard data, the crystal structure of wurtzite ZnO was revealed by the display of the primary ZnO peaks in the diffraction peaks of the pure ZnO (JCPDS card no. 36-1451 data) [5,10]. In addition, the diffraction peaks of the pure CWO sample can only be indexed as the monoclinic of CdWO<sub>4</sub>, (JCPDS card no. 14-0676) [16]. X-ray powder diffraction analysis of a ZnO/CWO: Ce nanocomposite confirmed the simultaneous presence of

both hexagonal ZnO and monoclinic CWO in the material [11].

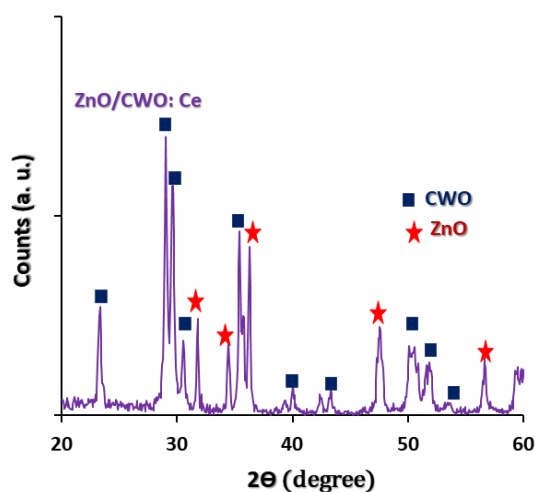


Figure 1. XRD pattern of CWO/ZnO: Ce

The morphology of the prepared doped nanocomposite was examined using the TEM image given in Figure 2. The prepared ZnO/CWO: Ce nanocomposite sample is composed of particles with spheroid, cubic, and rod-like morphologies with an average diameter of 70-150 nm.

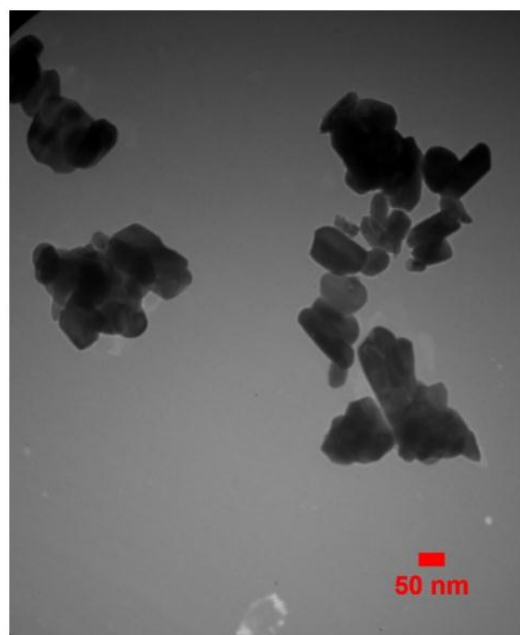
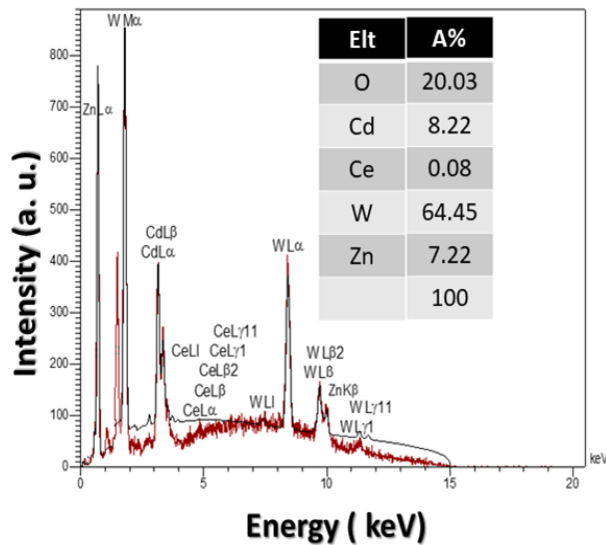


Figure 2. TEM images of the prepared doped nanocomposite particles

As observed in Figure 3, the EDX spectrum was used to verify the presence and relative abundance of the element of Zn, Cd, W, Ce, and O on the surface of the produced nanocomposite.



**Figure 3.** The energy-dispersive X-ray spectrum of the Ce doped nanocomposite

The optical properties of the synthesized samples were studied using ion beam/laser/gamma induced luminescence techniques. Figure 4 presents the schematic of the experimental setup under proton and CW Nd: YAG laser excitations (1064 nm).

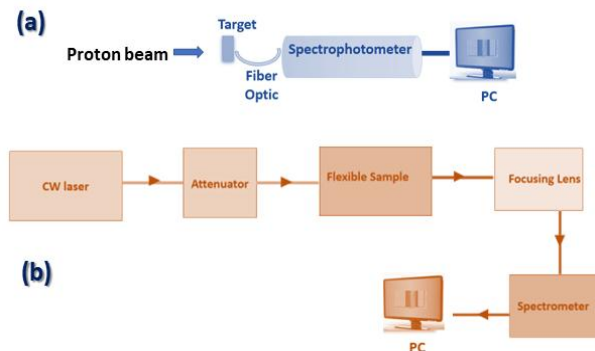


**Figure 4.** Brief schematic of the (a) IBIL and (b) Laser induced luminescence setups

Near-Band-Edge (NBE) emission in the ultraviolet and visible broadband emission in the visible range are both observed in luminescence spectra of ZnO [19-22]. The oxygen vacancies that generate a majority of the faults have a very low ionization energy. The band gap energy, band-to-band transitions, and exciton recombination of ZnO are the main reasons behind the formation of the UV emission peaks [22]. The major cause of the blue-green emission from the  $CdWO_4$  structure is the  $1A^1-3T^1$  transitions inside the  $WO_6$  complex [12,20]. In general, the anion complex  $WO_4^{2-}$  emits powerful blue-green radiation due to the charge-transfer type electronic transitions between oxygen and  $WO_4^{2-}$  inside the

complex [23].

Ce doping of the ZnO/CWO nanocomposite improved its luminosity. This enhancement may be attributable to the natural surface flaws of the host lattice, thus allowing for more efficient energy transfer to the Ce dopant. Ion Beam-Induced Luminescence (IBIL) characterization technique helps confirm the presence of impurities, flaws, and chemical compounds in the given material. As observed in Figure 5, when subjected to a focused proton beam, pure ZnO/CWO and Ce doped ZnO/CWO nanocomposites exhibit emission peaks at 500 nm. It is also observed that doped ZnO/CWO nanocomposite has the stronger luminescence than its counterparts. The luminescence spectra of the laser-excited prepared samples are given in Figure 6 according to which, the doped sample has stronger peaks than others in the 420-460 nm range as a result of the upconversion photon processes in the host ZnO/CWO. The scintillation and luminescence studies confirmed that ZnO/CWO: Ce could be a promising material to be used in lasers and other photonic devices.

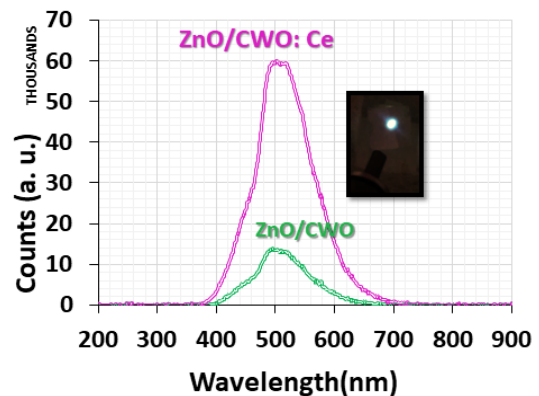


**Figure 5.** IBIL spectrum of pure and Ce doped ZnO/CWO nanocomposites

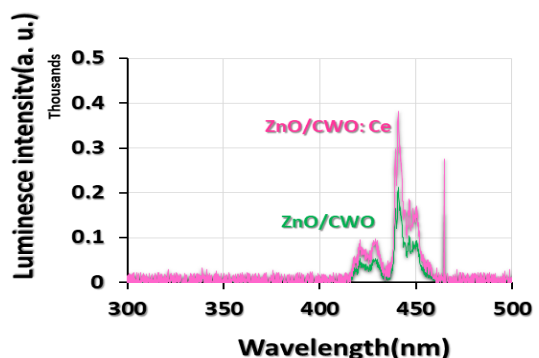


**Figure 6.** Luminescence spectrum of the pure and Ce doped ZnO/CWO nanocomposites under CW laser excitation

As observed in Figure 7, the prepared pellets were irradiated with  $^{60}Co$  gamma rays, and TL properties were

measured. In this figure, the TL emission curve of Ce Doped sample is stronger than the pure one, and its peaks are observed at 350-400 °C that could be related to luminescent centers. As shown in Figure 8, TL dose response of the synthesized doped pellet was studied over radiation absorbed dose. Here, the doped phosphor exhibits a nearly linear dose response.

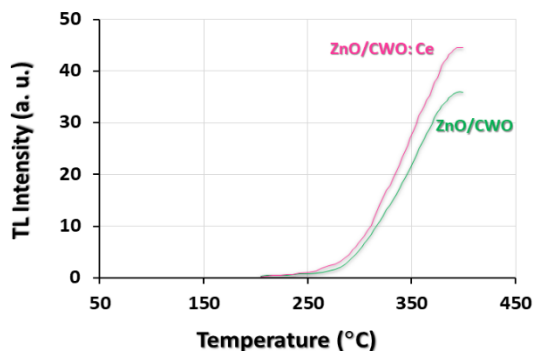


Figure 7. TL spectra of pure and Ce doped ZnO/CWO nanocomposite pellets

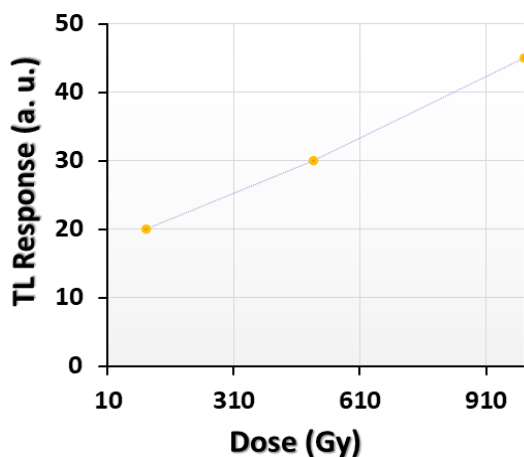


Figure 8. TL dose response of Ce doped ZnO/CWO nanocomposite pellet

#### 4. CONCLUSION

In the present study, two mixes of pure and Ce doped oxide nanocomposites were successfully prepared via a simple method. The XRD results confirmed the simultaneous existence of both monoclinic CWO and hexagonal ZnO. Doped nanocomposite particles under proton/laser irradiations displayed significant luminescence in the blue-green region. TL study of the ZnO/CWO: Ce pellet showed a relatively strong glow peak at 350-400 °C. The presence of Zn, O, Cd, W, and Ce elements in the composites was confirmed using the EDX technique. Doped phosphor exhibited a nearly linear gamma dose response. According to the findings,

the synthesized ZnO/CWO: Ce nanocomposite particles could be the appropriate potential components of optoelectronic devices.

#### ACKNOWLEDGEMENTS

The authors wish to acknowledge Semnan University for the all support throughout this work.

#### REFERENCES

- Enríquez-Sánchez, N., Vilchis-Nestor, A. R., Camacho-López, S., Camacho-López, M. A., Camacho-López, M., "Colloidal MnO<sub>x</sub> NPs/Carbon sheets nanocomposite synthesis by laser ablation in liquids", *Optics & Laser Technology*, Vol. 146, (2022), 107591. <https://doi.org/10.1016/j.optlastec.2021.107591>
- Dey, S., Kar, A. K., "Effect of acceptor concentration in the FRET controlled photoluminescence of PMMA-ZnO nanocomposite for the application of PLED device", *Optics & Laser Technology*, Vol. 136, (2021), 106811. <https://doi.org/10.1016/j.optlastec.2020.106811>
- Alamdari, S., Ghamsari, M. S., Tafreshi, M. J., "Novel scintillation properties by entrapping ZnO: Ga nanocrystals in epoxy polymer", *Progress in Nuclear Energy*, Vol. 130, (2020), 103495. <https://doi.org/10.1016/j.pnucene.2020.103495>
- Al-Hiti, A. S., Al-Masoodi, A. H. H., Harun, S. W., Yasin, M., Wong, W. R., "Tungsten trioxide (WO<sub>3</sub>) film absorber for generating soliton mode-locked pulses in erbium laser", *Optics & Laser Technology*, Vol. 131, (2020), 106429. <https://doi.org/10.1016/j.optlastec.2020.106429>
- Fortunato, E., Gonçalves, A., Pimentel, A., Barquinha, P., Gonçalves, G., Pereira, L., Ferreira, I., Martins, R. J. A. P. A., "Zinc oxide, a multifunctional material: from material to device applications", *Applied Physics A*, Vol. 96, No. 1, (2009), 197–205. <https://doi.org/10.1007/s00339-009-5086-5>
- Nunes, D., Pimentel, A., Gonçalves, A., Pereira, S., Branquinho, R., Barquinha, P., Fortunato, E., Martins, R., "Metal oxide nanostructures for sensor applications", *Semiconductor Science and Technology*, Vol. 34, No. 4, (2019), 043001. <https://doi.org/10.1088/1361-6641/ab011e>
- Ferreira, S. H., Morais, M., Nunes, D., Oliveira, M. J., Rovisco, A., Pimentel, A., Águas, H., Fortunato, E., Martins, R., "High UV and Sunlight Photocatalytic Performance of Porous ZnO Nanostructures Synthesized by a Facile and Fast Microwave Hydrothermal Method", *Materials*, Vol. 14, No. 9, (2021), 2385. <https://doi.org/10.3390/ma14092385>
- Tian, W., Li, J., "Size-dependent optical-electrical characteristics of blue GaN/InGaN micro-light-emitting diodes", *Applied Optics*, Vol. 59, No. 29, (2020), 9225-9232. <https://doi.org/10.1364/AO.405572>
- Liu, Z., Li, J. and Liu, X., "Novel functionalized BN nanosheets/epoxy composites with advanced thermal conductivity and mechanical properties", *ACS Applied Materials & Interfaces*, Vol. 12, No. 5, (2020), 6503-6515. <https://doi.org/10.1021/acsami.9b21467>
- Alamdari, S., Jafar Tafreshi, M., Sasani Ghamsari, M., "Preparation and characterization of gallium doped zinc oxide/polystyrene nanocomposite scintillator for alpha particles detection", *Applied Physics A*, Vol. 125, No. 6, (2019), 450. <https://doi.org/10.1007/s00339-019-2727-1>
- Alamdari, S., Ghamsari, M. S., Tafreshi, M. J., "Novel scintillation properties by entrapping ZnO: Ga nanocrystals in

- epoxy polymer”, *Progress in Nuclear Energy*, Vol. 130, (2020), 103495. <https://doi.org/10.1016/j.pnucene.2020.103495>
12. Alamdari, S., Sasani Ghamsari, M., Lee, C., Han, W., Park, H. H., Tafreshi, M. J., Afarideh, H., Ara, M. H. M., “Preparation and Characterization of Zinc Oxide Nanoparticles Using Leaf Extract of *Sambucus ebulus*”, *Applied Sciences*, Vol. 10, No. 10, (2020), 3620. <https://doi.org/10.1016/j.aprdiso.2021.110050>
  13. Alamdari, S., Ghamsari, M. S., Tafreshi, M. J., “Optimization of Gallium concentration to improve the performance of ZnO nanopowders for nanophotonic applications”, *Ceramics International*, Vol. 46, No. 4, (2020), 4484-4492. <https://doi.org/10.1016/j.ceramint.2019.10.175>
  14. Alamdari, S., Ara, M. H. M., Tafreshi, M. J., “Synthesize and optical response of ZnO/CdWO<sub>4</sub>: Ce nanocomposite with high sensitivity detection of ionizing radiations”, *Optics & Laser Technology*, Vol. 151, (2022), 107990. <https://doi.org/10.1016/j.optlastec.2022.107990>
  15. Lim, C. S., “Microwave-assisted synthesis of CdWO<sub>4</sub> by solid-state metathetic reaction”, *Materials Chemistry and Physics*, Vol. 131, No. 3, (2012), 714–718. <https://doi.org/10.1016/j.matchemphys.2011.10.039>
  16. Ziluei, H., Azimirad, R., Larijani, M. M., Ziaie, F., “Preparation and optimization of CdWO<sub>4</sub>-polymer composite film as an alpha particle counter”, *Nuclear Instruments and Methods in Physics Research Section A: Accelerators, Spectrometers, Detectors and Associated Equipment*, Vol. 852, (2017), 85-90. <https://doi.org/10.1016/j.nima.2017.01.015>
  17. Kumar, E. D., Thirumalai, K., Aravindhan, R., Swaminathan, M., Rao, J. R., Nair, B.U., “Visible light photocatalytic degradation of wattle extract: effect of mixing CdWO<sub>4</sub> over a semiconductive ZnO photocatalyst”, *RSC advances*, Vol. 5, No. 75, (2015), 60926-60937. <https://doi.org/10.1039/C5RA06926B>
  18. Fatima, B., Siddiqui, S. I., Nirala, R.K., Vikrant, K., Kim, K. H., Ahmad, R., Chaudhry, S. A., “Facile green synthesis of ZnO-CdWO<sub>4</sub> nanoparticles and their potential as adsorbents to remove organic dye”, *Environmental Pollution*, Vol. 271, (2021), 116401. <https://doi.org/10.1016/j.envpol.2020.116401>
  19. Yang, J., Gao, M., Yang, L., Zhang, Y., Lang, J., Wang, D., Wang, Y., Liu, H., Fan, H., “Low-temperature growth and optical properties of Ce-doped ZnO nanorods”, *Applied Surface Science*, Vol. 255, No. 5, (2008), 2646-2650. <https://doi.org/10.1016/j.apsusc.2008.08.001>
  20. Rondinone, A. J., Pawel, M., Travaglini, D., Mahurin, S., Dai, S., “Metastable tetragonal phase CdWO<sub>4</sub> nanoparticles synthesized with a solvothermal method”, *Journal of Colloid and Interface Science*, Vol. 306, No. 2, (2007), 281–284. <https://doi.org/10.1016/j.jcis.2006.10.064>
  21. Fatima, B., Siddiqui, S. I., Nirala, R. K., Vikrant, K., Kim, K. H., Ahmad, R., Chaudhry, S. A., “Facile green synthesis of ZnO-CdWO<sub>4</sub> nanoparticles and their potential as adsorbents to remove organic dye”, *Environmental Pollution*, Vol. 271, (2021), 116401. <https://doi.org/10.1016/j.envpol.2020.116401>
  22. Ghamsari, M. S., Alamdari, S., Razzaghi, D., Pirlar, M. A., “ZnO nanocrystals with narrow-band blue emission”, *Journal of Luminescence*, Vol. 205, (2019), 508–518. <https://doi.org/10.1016/j.jlumin.2018.09.064>
  23. Bardelli, L., Bini, M., Bizzeti, P. G., Carraresi, L., Danevich, F. A., Fazzini, T. F., Grinyov, B. V., Ivannikova, N. V., Kobychyev, V. V., Kropivnyansky, B. N., Maurenzig, P. R., “Further study of CdWO<sub>4</sub> crystal scintillators as detectors for high sensitivity 2β experiments: Scintillation properties and pulse-shape discrimination”, *Nuclear Instruments and Methods in Physics Research Section A: Accelerators, Spectrometers, Detectors and Associated Equipment*, Vol. 569, No. 3, (2006), 743-753. <https://doi.org/10.1016/j.nima.2006.09.094>
  24. Alamdari, S., Haji Ebrahimi, M., Mirzaee, O., Jafar Tafreshi, M., Majlesara, M. H., Tajali, M., Sasani Ghamsari, M. Mohammadi, A., “Cerium doped Tungsten-Based Compounds for Thermoluminescence Application”, *Progress in Physics of Applied Materials*, Vol. 2, No. 1, (2022), 35-40. <https://doi.org/10.22075/ppam.2022.27086.1028>



Materials and Energy Research Center

MERC

Contents lists available at ACERP

Advanced Ceramics Progress

Journal Homepage: [www.acerp.ir](http://www.acerp.ir)

## Original Research Article

# Design and Study of the Photodetection Performance of Photodetector Based on CH<sub>3</sub>NH<sub>3</sub>PbBr<sub>3</sub> Organic-Inorganic Hybrid

Elmira Sadeghilar<sup>a</sup>, Soghra Mirershadi<sup>b,\*</sup>, Farhad Sattari<sup>c</sup><sup>a</sup> MSc, Department of Physics, Faculty of Sciences, University of Mohaghegh Ardabili, Ardabil, Ardail, Iran<sup>b</sup> Associate Professor, Department of Engineering Sciences, Faculty of Advanced Technologies, University of Mohaghegh Ardabili, Namin, Ardail, Iran<sup>c</sup> Associate Professor, Department of Physics, Faculty of Sciences, University of Mohaghegh Ardabili, Ardabil, Ardabil, Iran\* Corresponding Author Email: [s.mirershadi@uma.ac.ir](mailto:s.mirershadi@uma.ac.ir) (S. Mirershadi)URL: [https://www.acerp.ir/article\\_159417.html](https://www.acerp.ir/article_159417.html)

## ARTICLE INFO

## ABSTRACT

## Article History:

Received 5 October 2022

Received in revised form 24 October 2022

Accepted 24 October 2022

## Keywords:

Photodetector  
Optoelectronic Device  
Perovskite  
Response

In this paper, the performance of photodetectors based on CH<sub>3</sub>NH<sub>3</sub>PbBr<sub>3</sub> organic-inorganic hybrid was evaluated, given their wide applications in different industries. This structure an appropriate for the active layer of photodetector device. Impressive results are concluded by changing the halogen atom and the energy gap of the hybrid structures. The obtained results reveal that the investigation of the appropriate organic cation and suitable halogen atom, as well as the concentration of the hybrids in the photodetectors, are necessary to find a suitable condition for an effective photodetectors. Exciting results are achieved by considering the Current-voltage (I-V) curves of darkness and light. The I-V curve with 1.8 wt. % concentration of CH<sub>3</sub>NH<sub>3</sub>PbBr<sub>3</sub> organic-inorganic hybrid shows the I<sub>sc</sub> of 1 μA and response of 0.027 μA/W. The device with 1.2 wt. % concentration showed I<sub>sc</sub> of 0.25 μA and response of 0.006 μA/W. Perovskites are optically configurable so that they acquire proper band gaps with high slope absorption edge and considerable efficiencies in collecting the charges produced by the light.

<https://doi.org/10.30501/acp.2022.364509.1105>

## 1. INTRODUCTION

Photodetectors are among the most interesting optical communication components that play a significant role in many fields such as spectroscopy and ultraviolet detection, to name a few [1]. These components convert optical signals into electrical signals. A photodetector consists of an optically active region connected to two metal electrodes. In order for the active region to absorb more radiant light, the thickness of this area should be

low. When light with adequate energy shines on the surface of the intended semiconductor which acts as an active layer, the electron pairs-generated holes are collected and generate an electric current [2].

The function of photodetectors depends on several important factors, one of which is the current response rate obtained through Equation (1).

$$R_i = I_{out}/P_{in} \quad (1)$$

Please cite this article as: Sadeghilar E., Mirershadi, S., Sattari, F., "Design and Study of the Photodetection Performance of Photodetector Based on CH<sub>3</sub>NH<sub>3</sub>PbBr<sub>3</sub> Organic-Inorganic Hybrid", *Advanced Ceramics Progress*, Vol. 8, No. 3, (2022), 13-17. <https://doi.org/10.30501/acp.2022.364509.1105>

2423-7485/© 2022 The Author(s). Published by MERC.

This is an open access article under the CC BY license (<https://creativecommons.org/licenses/by/4.0/>).

The response of a photodetector determines how much light current is produced due to light radiation with a certain wavelength [3]. In other words, responsiveness could be defined as the ratio of the output electrical signal (output current or  $I_{out}$ ) to the radiant optical power ( $P_{in}$ ).

Another important factor for photodetectors is the external quantum efficiency. The ratio of the electron pairs- generated holes by the photodetector to the number of photons irradiated on the photosensitive region is called quantum efficiency [4].

Dark current is an important parameter in the study of photodetectors. It is a small current that occurs without radiation falling on the photodetector in it. Most photodetectors need a secondary power source in order to detect light better that in turn incurs high costs. To solve this problem, a new kind of photodetectors which function without a secondary source of power was employed [5].

Although the concept of photovoltaic has been of interest to the researchers in recent years, it still has an inherent potential for constructing new detectors. These types of detectors are one of the most common electronic tools in optoelectronics due to the high speed of responsiveness [6]. Since one of the connections contains reverse bias, these tools have lower dark current than other photodetectors [7].

Figure 1 shows a schematic of photodetectors based on organic-inorganic perovskite which consists of two electrodes, a substrate, and a light-sensitive layer. This configuration is formed by layering perovskite with the thickness of 200 nanometers on the indium tin oxide substrate and also a conjunction of aluminum metal on the organic-inorganic perovskite.

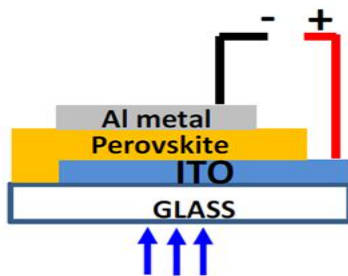


**Figure 1.** Schematic of photodetectors [8]

A great deal of efforts have been made in conducting ultraviolet detection with semiconductors that contain big energy gaps until now [9]. In recent years, two-dimensional substances have been widely utilized among which, graphene and black phosphorus are two of the best examples [10]. One-dimensional substances, such as carbon nanotubes, and one-dimensional metals have been widely used in recent years for conducting photodetectors owing to their mechanical and optoelectronic properties [11]. These substances include

features like a weak interlayer covalent bond, high mechanical resistance, high luminescence, strong quantum confinement, and adjustable band gap [12]. Commonly used electrodes in making photodetectors are gold (Au), silver (Ag), and indium tin oxide [13]. In practical applications, heat, light radiation, and humidity are the main factors that have a destructive effect on the performance of photodetectors. In order to prevent these uncalled-for effects, the encapsulation method in the photovoltaic industry is commonly used [14]. Modern photodetectors are mainly based on semiconductor materials with an adequate band gap that converts photons with different energies into electrical signals for the procession, reconstruction, and storage of images [13].

In the last few decades, organic substances have been used in many optoelectronic tools such as photodetectors owing to their cheapness and easy processability. However, in order to conduct organic-based optoelectronic tools, some other obstacles such as low mobility of charge carriers and chemical interactions should be taken into consideration. One of the suggested solutions to this problem is to use organic-inorganic hybrid materials which enjoy the benefits of both organic and inorganic compartments while overcoming either one's limitations. In recent years, there has been a significant interest surge in studies on conducting organic-inorganic hybrid perovskite structures in the solar cells field. In addition to this field, more research projects focused on the photodetectors based on organic-inorganic hybrids during the past two years due to the extraordinary optoelectronic features of these structures. Owing to such an exclusive function, optoelectronic tools based on these materials, such as photodetectors and optical transistors, have been developed and reviewed in recent years [15].

Three-dimensional organic-inorganic halogen hybrids are another common structure of hybrids. These hybrids contain the general formula  $AMX_3$ , where A is a monovalent cation and commonly Li, Na, K, Rb, Cs or an organic amine cation of proper size, and M the bivalent metals of the periodic table such as ( $Cu^{2+}$ ,  $Ni^{2+}$ ,  $Co^{2+}$ ,  $Fe^{2+}$ ,  $Mn^{2+}$ ,  $Pd^{2+}$ ,  $Cd^{2+}$ ,  $Ge^{2+}$ ,  $Sn^{2+}$ ,  $Eu^{2+}$ , and  $Pb^{2+}$ ), and X a halogen element [16].

## 2. MATERIALS AND METHODS

### 2.1. Synthesis of Perovskite Structures

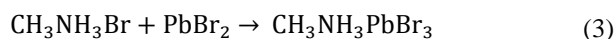
Synthesis of hybrid structures is the most primary and essential requirement in their examination, and they are usually synthesized through simple chemical methods. Organic-inorganic hybrid structures is generally synthesized in two steps namely the synthesis of amino salt and preparation of perovskite solution.

Lead dibromide salt ( $PbBr_2$ , sigma aldrich) with high purity as the mineral part and methylamine ( $CH_3NH_2$ ,

40 % solution in water, Merck) as the supplier of the organic part are used for the synthesis of  $\text{CH}_3\text{NH}_3\text{PbBr}_3$  organic-inorganic hybrid, as used in this research. In the first step, an amine salt is extracted by the reaction of stoichiometric amount of  $\text{CH}_3\text{NH}_2$  with hydrobromic acid (HBr, 47 %, Merck). Given that this reaction is highly exothermic, this step is done by placing a two-necked flask in a mixture of water and ice in order to reduce the reaction temperature. The synthesis equation of amino salt can be written as follows:



Then, solid  $\text{PbBr}_2$  is added to the produced solution, whose reaction equation is given below:



It is worth noting that organic-inorganic hybrid structures are transformed into an orange powder after 24 hours at the room temperature and one week at  $50^\circ\text{C}$ . All materials were used without further purification.

## 2.2. Design of Photodetector

In this research, photodetectors were constructed using an organic-inorganic hybrid  $\text{CH}_3\text{NH}_3\text{PbBr}_3$  substance with the weight percentages of 1.2 and 1.8 percent in dimethyl sulfoxide (DMSO,  $\geq 99.9\%$  Merck) solvent as the active region. Indium tin oxide and silver were used as anode and cathode, respectively. Indium tin oxide substrates with the thickness of one mm and dimensions of  $2 \times 2 \text{ cm}^2$  were purchased. These substrates were ultrasonicated with ethyl alcohol and distilled water for 10 minutes and then dried in an oven at  $70^\circ\text{C}$  for 15 minutes before use. The solution was prepared from solving synthesized organic-inorganic hybrid substances with the concentrations of 1.2 and 1.8 % by weight in DMSO solvent and then layered on the indium tin oxide substrates. Next, it was placed into the oven at a temperature of  $65^\circ\text{C}$  for 24 hours. Subsequently, silver was used to make the wire connections from cathode and anode and finally, characterize the current-voltage (I-V) of the built photodetector.

In order to characterize the synthesized hybrids and review the features of the crystal structure and determine their lattice parameters, X-Ray Diffraction (XRD) (Cu  $K\alpha$  X-ray radiation source-Ital structures model MPD 3000) with  $2\theta$  in the temperature range of  $2^\circ$ - $50^\circ$  was used. Furthermore, to evaluate the optical behavior of organic-inorganic hybrids, different approaches and equipment were used, among the most significant of which are Ultraviolet-Visible (UV-Vis) optical absorption and Diffusion Reflectance Spectroscopy (DRS) which were recorded via a Sinco S4100 spectrophotometer in the range of 200 to 800 nm at room

temperature. The photovoltaic parameters were obtained through measuring the I-V curves (sharif solar PGS10) under irradiation of AM1.5. A Mercury lamp (Philips 36W) was also used as an excitation source.

## 3. RESULTS AND DISCUSSION

Figure 2 shows the XRD pattern of the synthesized hybrid structures. The data analysis shows that the peaks observed at the angles of  $14.77^\circ$ ,  $20.97^\circ$ ,  $29.95^\circ$ ,  $42.9^\circ$ , and  $45.74^\circ$  correspond to the Miller plates with Miller indexes of (100), (110), (200), (210), (220), and (300) related to the cubic structure of  $\text{CH}_3\text{NH}_3\text{PbBr}_3$  with the lattice constant of 5.657 angstroms.

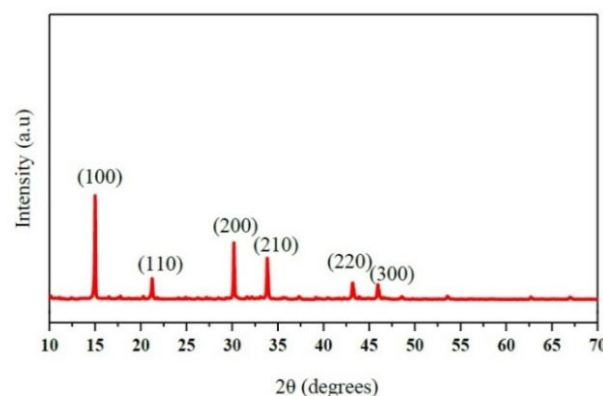


Figure 2. X-ray diffraction pattern of  $\text{CH}_3\text{NH}_3\text{PbBr}_3$

Figure 3 shows the absorption spectrum of the synthesized structure. This spectrum was obtained at the room temperature. As observed, this structure is characterized by high absorption rate at the wavelength of 522 nanometers.

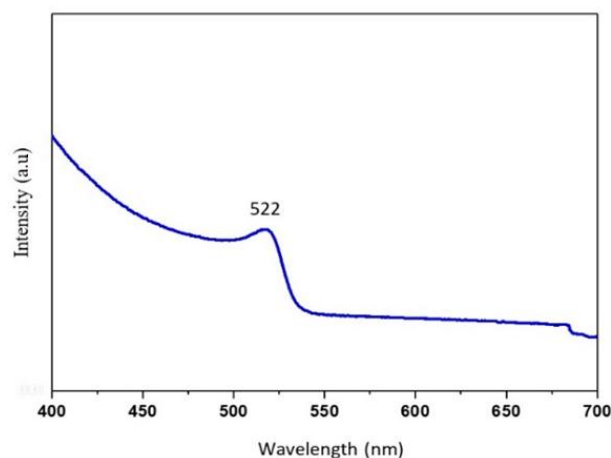
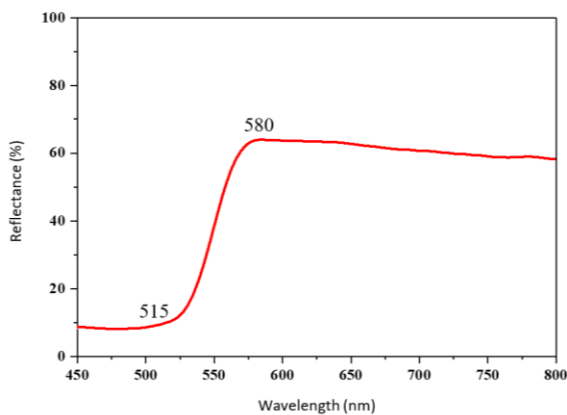


Figure 3. UV-visible absorption spectra of  $\text{CH}_3\text{NH}_3\text{PbBr}_3$

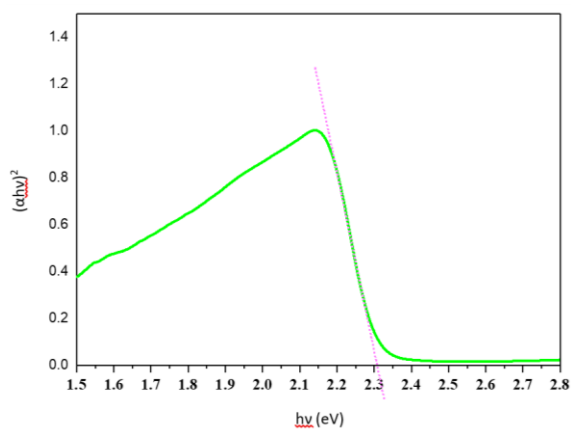
In order to determine the energy gap of the synthesized

hybrid structure, reflection diffusion spectroscopy was employed. Diffusion reflection spectroscopy shows the transfer of electrons from the valence band to the conduction band as a result of absorbing the energy of the descended photon, thus reducing the intensity of the light in the said wavelength. Accordingly, the relative percentage of the transmitted to the reflected light decreases. Figure 4 presents the diffuse reflection spectrum of  $\text{CH}_3\text{NH}_3\text{PbBr}_3$  perovskite structure according to which, at the wavelength of 580 nanometers, there is a sharp decrease in the intensity of the reflected light.



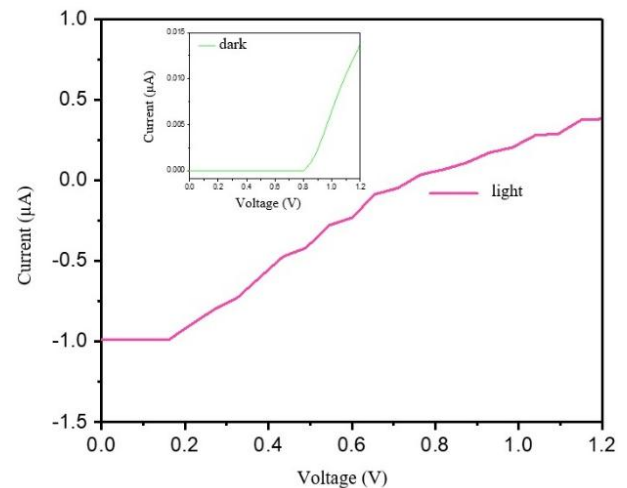
**Figure 4.** The diffuse reflection spectrum of  $\text{CH}_3\text{NH}_3\text{PbBr}_3$  perovskite structure

Moreover, in order to determine the energy gap through the theory of Mott and Davis [16], the curve of changes  $(\alpha h\nu)^2$  in the photon energy ( $h\nu$ ) is drawn in Figure 5. By drawing a tangent line to the graph in the linear region, the energy gap for the synthesized hybrid structure is determined. As demonstrated in Figure 5, the energy gap in the  $\text{CH}_3\text{NH}_3\text{PbBr}_3$  hybrid structure is 2.30 electron volts.



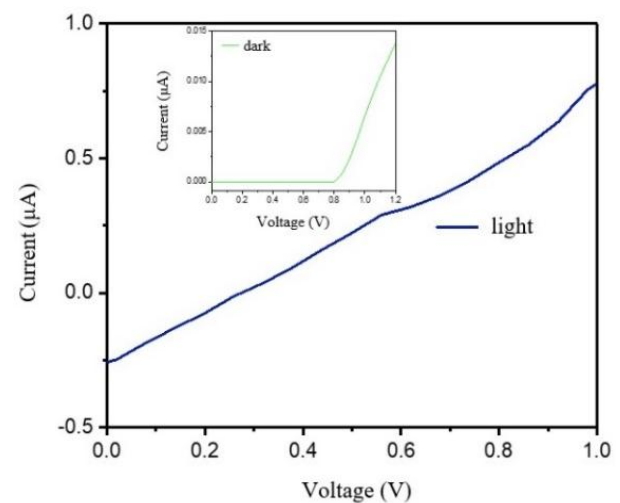
**Figure 5.** Curve of  $(\alpha h\nu)^2$  as function of photon energy ( $h\nu$ ) for the  $\text{CH}_3\text{NH}_3\text{PbBr}_3$

Figure 6 shows the I–V diagram of the photodetector based on  $\text{CH}_3\text{NH}_3\text{PbBr}_3$  organic-inorganic hybrid material made with 1.8 wt. % in dimethylsulfoxide solvent under both darkness and illumination. As observed in the diagram under illumination, the short-circuit current ( $I_{SC}$ ) for this photodetector is equal to  $1 \mu\text{A}$ , and the response rate of the current for this photodetector is equal to  $0.027 \mu\text{A/W}$  (Equation (1)). The graph under darkness also starts from zero and increases exponentially, considering that there is no light or radiation.



**Figure 6.** The current-voltage curve of photodetector based on an organic-inorganic hybrid material  $\text{CH}_3\text{NH}_3\text{PbBr}_3$  with 1.8 wt. % in dimethyl sulfoxide under both darkness and light

Figure 7 depicts the I–V curve of the photodetector made based on  $\text{CH}_3\text{NH}_3\text{PbBr}_3$  organic-inorganic hybrid material with 1.2 wt. % in DMSO solvent.



**Figure 7.** The current-voltage curve of photodetector based on an organic-inorganic hybrid material  $\text{CH}_3\text{NH}_3\text{PbBr}_3$  with 1.2 wt. % in dimethyl sulfoxide under both darkness and light

According to the I-V curves, the  $I_{SC}$  in this detector was calculated to be 0.25  $\mu A$ , and the current response for this detector was calculated to be 0.006  $\mu A/W$ , which is less than 1.8 wt. %. It can be concluded that the higher the short circuit current, the greater the surface area under the I-V diagram and the higher the response rate.

#### 4. CONCLUSION

The current study used  $CH_3NH_3PbBr_3$  organic-inorganic hybrid materials to design photodetectors in small dimensions. The current response rate was calculated for the photodetector based on  $CH_3NH_3PbBr_3$  hybrid material with 1.8 wt. % in DMSO solvent equal to 0.027  $\mu A/W$ , which showed the highest response among other photodetectors made in this research. The results revealed that with an increase in the concentration of perovskite material, the response rate for photodetectors would increase. Application of organic-inorganic hybrids led to the development of new generation photodetectors mainly due to the optically tunable nature of these materials. As a result, an adequate band gap was obtained, hence significant efficiency in collecting the load produced by light.

#### ACKNOWLEDGEMENTS

The authors thank the University of Mohaghegh Ardabili for their cooperation and support.

#### REFERENCES

- Huang, S. M., Huang, S. J., Yan, Y. J., Yu, S. H., Chou, M., Yang, H. W., Chang, Y. S., Chen, R. S., "Extremely high-performance visible light photodetector in the  $Sb_2SeTe_2$  nanoflake", *Scientific Reports*, Vol. 7, No. 1, (2017), 45413. <https://doi.org/10.1038/srep45413>
- Tang, Y., Cao, X., Chi, Q., "Two-dimensional halide perovskites for emerging new-generation photodetectors", In Nayak, P. K. (ed.), *Two-Dimensional Materials for Photodetector*; *InTech Open: London*, (2018), 75-101. <https://doi.org/10.5772/intechopen.71032>
- Bass, M., *Handbook of Optics: volume I - Geometrical and Physical Optics, Polarized Light, Components and Instruments*, 3<sup>rd</sup> Ed., McGraw-Hill Education, New York, (2010). <https://www.accessengineeringlibrary.com/content/book/9780071498890>
- Jansen-van Vuuren, R. D., Armin, A., Pandey, A. K., Burn, P. L., Meredith, P., "Organic photodiodes: the future of full color detection and image sensing", *Advanced Materials*, Vol. 28, No. 24, (2016), 4766-4802. <https://doi.org/10.1002/adma.201505405>
- Wang, Z., Yu, C., Zhong, W. D., Chen, J., Chen, W., "Performance of a novel LED lamp arrangement to reduce SNR fluctuation for multi-user visible light communication systems", *Optics express*, Vol. 20, No. 4, (2012), 4564-4573. <https://doi.org/10.1364/OE.20.004564>
- Peng, L., Hu, L., Fang, X., "Low-dimensional nanostructure ultraviolet photodetectors", *Advanced Materials*, Vol. 25, No. 37, (2013), 5321-5328. <https://doi.org/10.1002/adma.201301802>
- Bhattacharya, P., *Semiconductor Optoelectronic Devices*, 2<sup>nd</sup> Ed., Prentice-Hall, Inc., USA, (1997).
- Müller, A., Konstantinidis, G., Androulidaki, M., Dinescu, A., Stefanescu, A., Cismaru, A., Neculoiu, D., Pavelescu, E., Stavrinidis, A., "Front and backside-illuminated GaN/Si based metal-semiconductor-metal ultraviolet photodetectors manufactured using micromachining and nano-lithographic technologies", *Thin Solid Films*, Vol. 520, No. 6, (2012), 2158-2161. <https://doi.org/10.1016/j.tsf.2011.09.045>
- Yoon, K. H., Ahn, J. K., Cho, J. Y., "Optical characteristics of undoped and Mn doped ZnS films", *Journal of Materials Science*, Vol. 36, No. 6, (2001), 1373-1376. <https://doi.org/10.1023/A:1017599302802>
- Zhao, Q., Sheng, T., Wang, Y., Tang, Z., Chen, Y., Cai, L., Ling, H., "M2det: A single-shot object detector based on multi-level feature pyramid network", In *Proceedings of the AAAI Conference on Artificial Intelligence*, Vol. 33, No. 1, (2019), 9259-9266. <https://ojs.aaai.org/index.php/AAAI/article/view/4962/4835>
- Feng, Q., Huang, L., Han, G., Li, F., Li, X., Fang, L., Xing, X., Zhang, J., Mu, W., Jia, Z., Guo, D., "Comparison Study of  $\beta$ -Ga<sub>2</sub>O<sub>3</sub> Photodetectors on Bulk Substrate and Sapphire", In *IEEE Transactions on Electron Devices*, Vol. 63, No. 9, (2016), 3578-3583. <https://doi.org/10.1109/TED.2016.2592984>
- Deng, H., Yang, X., Dong, D., Li, B., Yang, D., Yuan, S., Qiao, K., Cheng, Y. B., Tang, J., Song, H., "Flexible and semitransparent organolead triiodide perovskite network photodetector arrays with high stability", *Nano Letters*, Vol. 15, No. 12, (2015), 7963-7969. <https://doi.org/10.1021/acs.nanolett.5b03061>
- Li, D., Dong, G., Li, W., Wang, L., "High performance organic-inorganic perovskite-optocoupler based on low-voltage and fast response perovskite compound photodetector", *Scientific Reports*, Vol. 5, No. 1, (2015), 7902. <https://doi.org/10.1038/srep07902>
- Ahmad, S., Hanmandlu, C., Kanaujia, P. K., Prakash, G. V., "Direct deposition strategy for highly ordered inorganic organic perovskite thin films and their optoelectronic applications", *Optical Materials Express*, Vol. 4, No. 7, (2014), 1313-1323. <https://doi.org/10.1364/OME.4.001313>
- Pradeesh, K., Baumberg, J. J., Prakash, G. V., "In situ intercalation strategies for device-quality hybrid inorganic-organic self-assembled quantum wells", *Applied Physics Letters*, Vol. 95, No. 3, (2009), 033309. <https://doi.org/10.1063/1.3186639>
- Papavassiliou, G. C., Mousdis, G. A., Raptopoulou, C. P., Terzis, A., "Preparation and Characterization of  $[C_6H_5CH_2NH_3]_2PbI_4$ ,  $[C_6H_5CH_2CH_2SC(NH_2)_2]_3PbI_5$  and  $[C_{10}H_7CH_2NH_3]PbI_3$  Organic-Inorganic Hybrid Compounds", *Zeitschrift für Naturforschung B*, Vol. 54, No. 11, (1999), 1405-1409. <https://doi.org/10.1515/znb-1999-1112>



Materials and Energy Research Center

MERC

Contents lists available at [ACERP](#)

Advanced Ceramics Progress

Journal Homepage: [www.acerp.ir](http://www.acerp.ir)

## Original Research Article

## The Effect of Microwave Settings on HAp Sintering

Aida Faeghinia <sup>a,\*</sup>, Touradj Ebadzadeh <sup>b</sup><sup>a</sup> Associate Professor, Department of Ceramic, Materials and Energy Research Center, Karaj, Iran<sup>b</sup> Professor, Department of Ceramic, Materials and Energy Research Center, Karaj, Iran\* Corresponding Author Email: [a.faeghinia@merc.ac.ir](mailto:a.faeghinia@merc.ac.ir) (A. Faeghinia)URL: [https://www.acerp.ir/article\\_162551.html](https://www.acerp.ir/article_162551.html)

## ARTICLE INFO

## Article History:

Received 15 June 2022

Received in revised form 22 August 2022

Accepted 30 August 2022

## Keywords:

Hydroxyapatite  
Sintering  
Two Steps  
SEM

## ABSTRACT

Hydroxyapatite (HAp,  $\text{Ca}_{10}(\text{PO}_4)_6(\text{OH})_2$ ), a calcium phosphate bio ceramic which is chemically similar to natural bone mineral, is widely used as a scaffolding material in bone tissue engineering. In this study, Hydroxyapatite (HAp) ceramics were sintered using microwave in one- and two-step heat treatment. The sintering temperatures in the first heat treatment step were in the range of 965-1000 °C without isothermal holding, and the power levels of the microwave were set at 600, 750, and 900 W. The temperatures in the second heat treatment step were 600, 735, and 860 °C. Of note, HAp-to-Tricalcium phosphate (TCP) phase transformation was not detected at 1000 °C; instead, the preferred growth of (211) planes corresponding to the circular morphology was observed. As observed in the XRD images, crystallite degradation occurred in two-step sintered samples. In addition, the SEM micrographs indicated that the open porosity in the two-step heat treated samples was more than that of samples which were heat treated in one step. In case the sintering temperature was set at 1000 °C, the maximum density values of 92 % and 95 % were obtained for one- and two-step sintered samples, respectively.

<https://doi.org/10.30501/acp.2022.368201.1110>

## 1. INTRODUCTION

Hydroxyapatite (HAp,  $\text{Ca}_{10}(\text{PO}_4)_6(\text{OH})_2$ ) is a calcium phosphate bioceramic that is chemically similar to the natural bone mineral which is widely used as a scaffolding material for bone tissue engineering [1-3]. Sintering is critical for porous HAp bioceramic scaffolds in that it determines their microstructural properties such as crystallinity, grain size density, and micro-porosity, which in turn affects their performance [4,5]. However, a significant concern regarding the HAp sintering is the necessity of providing lower sintering temperatures to ensure better bioactivity [5].

Higher temperature and longer sintering times are also

required to ensure higher mechanical strength while sintering these materials. The conventional sintering methods, such as muffle sintering which is characterized by high temperature, slow heating rate, and long holding time, cannot solve this contradiction.

Microwave processing is defined as the sintering of specimens by putting them in a microwave equipped with an external heating source. It enjoys the advantage of reaching the required temperatures for material sintering within a short period of time, thus resulting in a uniform and dense microstructure [1-3]. Most HAp powders contain needle-like particles that hinder densification. Guo et al. [6] fabricated HAp nano-bioceramics based on Spark Plasma Sintering (SPS) approach. Bose et al. [7]

Please cite this article as: Faeghinia, A., Ebadzadeh, T., "The Effect of Microwave Settings on HAp Sintering", *Advanced Ceramics Progress*, Vol. 8, No. 3, (2022), 18-21. <https://doi.org/10.30501/acp.2022.368201.1110>

2423-7485/© 2022 The Author(s). Published by MERC.

This is an open access article under the CC BY license (<https://creativecommons.org/licenses/by/4.0/>).

also fabricated nano-crystalline HAp bioceramics through the microwave process. Chen [8] developed a new technique called Two-Step Sintering (TSS) method, a promising and straightforward approach to obtaining dense low-cost nanoceramics using typical ovens. To date, TSS has been successfully applied to sintering of  $Y_2O_3-Al_2O_3$ . In this regard, to better understand the effects of different experimental conditions, the current study investigated several involved criteria namely the microwave, heating rate conditions, sintering steps, and temperatures.

## 2. MATERIALS AND METHODS

The starting powder in this research was hydroxyapatite  $Ca_5(PO_4)_3OH$  (MERCK, CAS No. 1306-

06-5) (HAp) with the particle size of  $< 160 \mu m$ . The powder was pressed by two-axial cold pressing in a stainless-steel mold at 200 MPa to form disk-shaped samples of 10 mm in diameter and 11 mm in height, according to the British Standard for compression tests (No. 7253). All samples were first sintered in a high-temperature microwave furnace (600, 750, and 900 W) in the air at 750, 860, 965, and 1000 °C (heating rate was 60 °C/min) without holding the sintering time. Some samples were heat-treated by microwave in two steps, as reported in Table 1. A home-made microwave furnace (900 W and 2.45 GHz) with an  $Al_2O_3$  insulation container was used for microwave heating. The temperature of the microwave furnace was controlled by an optical pyrometer (RAYR312MSCL2G temperature detector) with the temperature fluctuation of  $\pm 5$  °C.

**TABLE 1.** The Microwave Conditions for sintering of the different samples

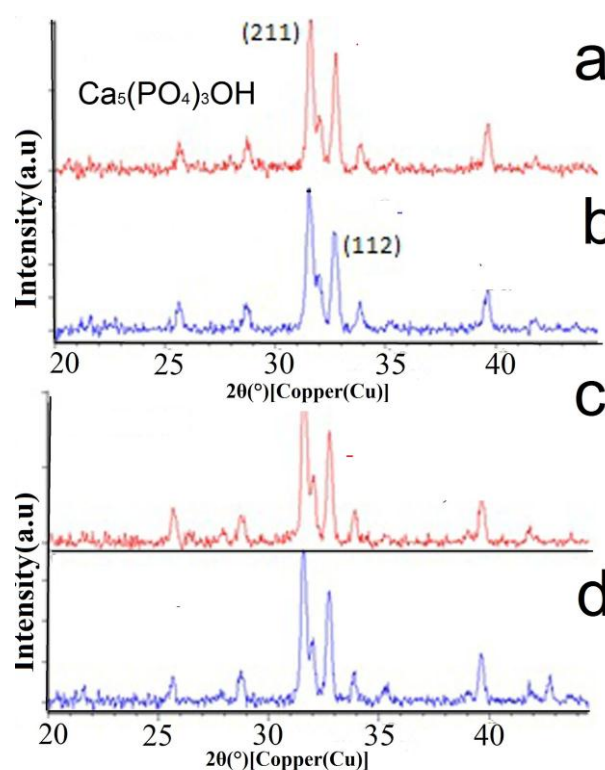
Microwave Conditions	1	2	3	4	5	6	7
Power Level	750	900	600	600	900	900	900
First Sintering Temperature	750	965	860	1000	1000	960	860
Sintering Time To Reach Maximum Temperature (min.)	75	125	22	47	14	9	13
Second Step Sintering Temperature (°C)		860				600	735

The physical properties of the sintered samples were also investigated in this study. The porosity of each sintered sample was determined by Archimedes method using distilled water. The lengths of samples before and after sintering were measured to calculate their linear shrinkage. All samples were analyzed using PANalytical X'Pert Pro powder diffractometer (Panalytical B.V., Almelo, Netherlands). The required data was collected continuously using an X'Celerator RTMS detector and a counting time equivalent to 100 s per point over  $2\theta = 5-70^\circ$  with the step size of  $2\theta = 0.03$  or  $0.016^\circ$ . The microstructure of the samples was then studied through Scanning Electron Microscopy (SEM, Quant a 200, FEI, Netherlands). The values of the magnification of the SEM parameters, accelerating voltage, and working distance were obtained in the ranges of 500-2000x, 3-20 kV, and 8-12  $\mu m$ , respectively.

## 3. RESULTS AND DISCUSSION

Figure 1 shows the XRD patterns of the samples sintered at 1000 and 965 °C according to which, the two-step heat treated samples were further heated followed by their first heating at 735 and 860 °C.

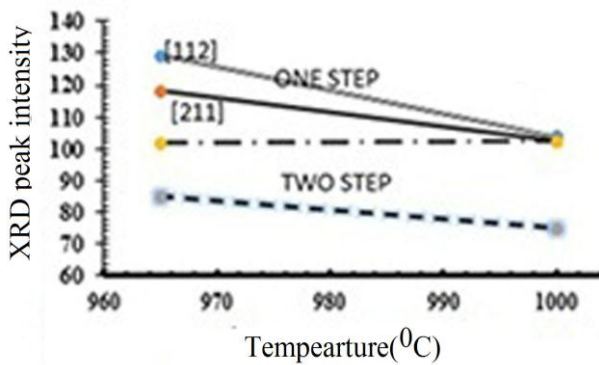
The results revealed the HAp peaks in the prevailing crystalline phase. Of note,  $\alpha$ -to- $\beta$  transformation of hydroxyl apatite, which was previously reported by Fu Xu [9], was not observed in the present study probably due to lack of isothermal heating at the sintering



**Figure 1.** XRD patterns of sintered samples by microwave at (a) one step (965 °C-900 W), (b) two steps (965 °C, 900 W-750 °C, 300 W), (c) one step (1000 °C, 900 W), and (d) two steps (1000 °C, 900 W-965 °C, 300 W)

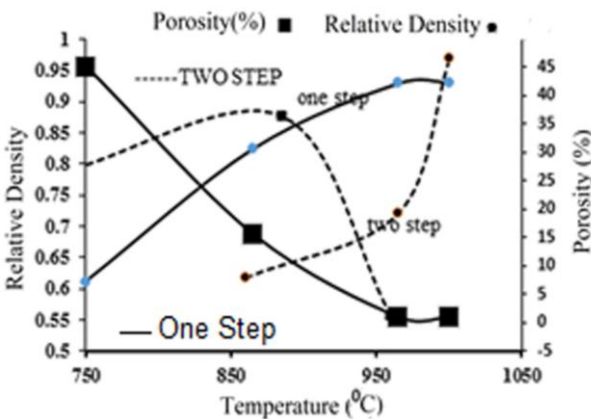
temperatures which suppressed this transformation. Sinitsyna [10] had already reported this phenomenon.

As observed, the peak intensity of (211) and (112) lattice planes decreased in the second heating step (Figure 2). In addition, the peak corresponding to (112) Millers plane family (at  $2\theta = 32.45^\circ$ ) is weaker than other ones in the case of two-step heat treatment, indicating the decreasing trend of the a-axis length in the HAp structure, as already mentioned in Reference [5]. In this regard, it can be concluded that the OH<sup>-</sup> vacancy increases upon increasing the steps of microwave sintering (OH<sup>-</sup> groups absorb the microwave radiation more than other ones). Pajchel [11] reported that OH<sup>-</sup> in nanocrystalline apatite would decrease by decreasing crystal size.



**Figure 2.** The relative intensities of the XRD peaks in (211) and (112) indexes of the sintered samples by microwave at 900 W in one- and two-step heat treatments

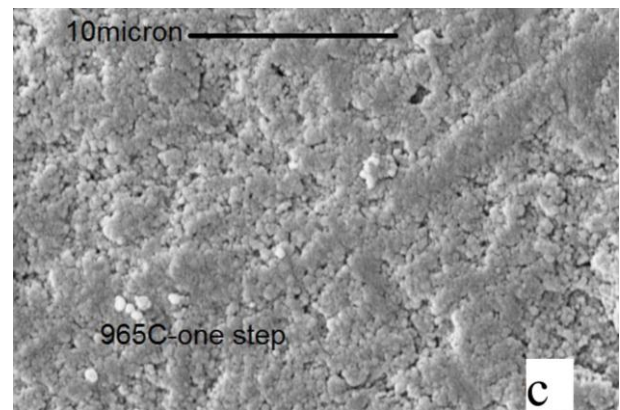
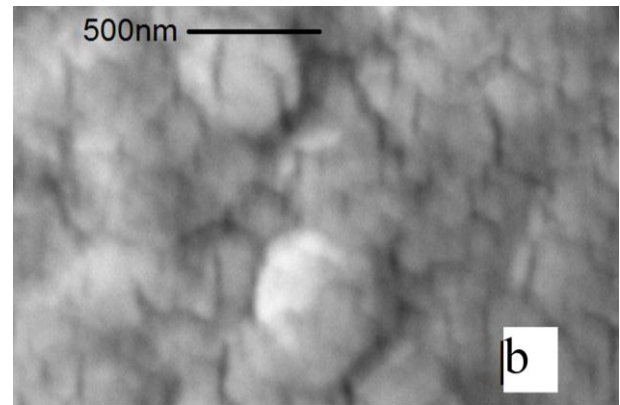
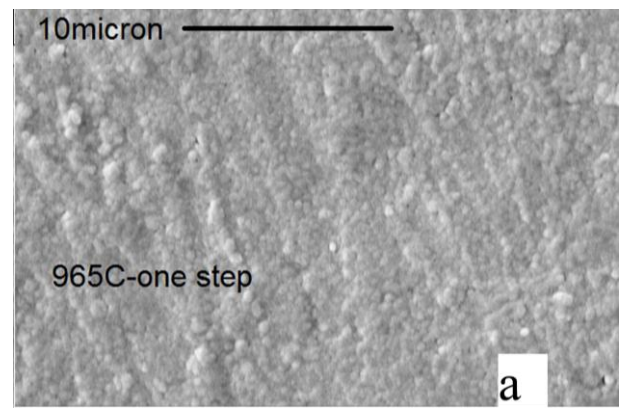
Figure 3 compares the relative density values of the samples sintered by both one- and two-step microwave heating. The obtained results revealed that one-step sintered samples were characterized by a higher density at all sintering temperatures than two-step sintered samples. At the sintering temperature of 1000 °C, the maximum density of 92% and 95% were obtained for one- and two-step sintered samples, respectively.



**Figure 3.** The relative densities and porosities of the one- and two-step microwave sintered samples

According to Fig. 3, the open porosity of the samples in the two-step heat-treatment process is more than that in the samples with one-step heat-treatment process. In addition, two-step heat treatment led to degraded crystallite phases and weak densification in the samples. Figure 4 makes a comparison between the microstructures of one- and two-step heating by microwave.

As observed in Figure 3, the two-step sintered samples did not achieve full densification. Of note, even at such a low temperature and a short holding time, the HAp grains were merged with each other [12-13]. At the triple junction points of the HAp grains, some nano pores were detected. Apparently, the appearance of pores would



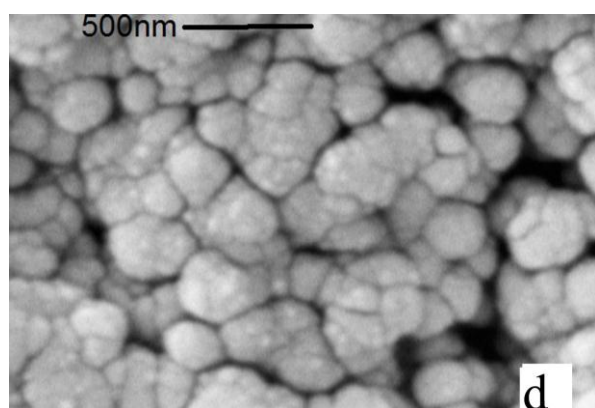


**Figure 4.** The micrographs of the microwave sintered samples at top one step heat treating at 965 °C by two different magnification (a)  $\times 1000$ , (b)  $\times 50000$ , (c) by two steps heat treating at 960-860 °C by  $\times 1000$  magnification, and (d) by two steps heat treating at 960-860 °C by  $\times 50000$  magnification

increase the diffusion distance between the HAp grains, thus reducing the driving force on the pore shrinkage of the sintered ceramics [6]. Therefore, in the case of the two-step heating, the porosity values decreased sharply. According to Figure 3, the dashed line curve corresponding to the two-step heating shrinkage shows a sharper trend than the one-step case. However, as observed in Figure 2, the crystallite size decreased (or degraded) in the case of two-step heating which can be related to the crystallite degradation, as approved by the XRD patterns demonstrated in Figure 1.

#### 4. CONCLUSION

Sintering the HAp samples by two-step heating using microwave confirmed that the relative density of all samples was similar; however, their open porosity was more than that of the samples which were heat-treated in one step. Two-step heating led to degraded crystallite (due to the OH vacancy) and weak densification.

#### ACKNOWLEDGEMENTS

The authors acknowledge the collaboration of Mrs. Zonozi and Ghofrani for their cooperation in carrying out the SEM and XRD analyses.

#### REFERENCES

1. Fang, Y., Agrawal, D. K., Roy, D. M., Roy, R., "Microwave sintering of hydroxyapatite ceramics", *Journal of Materials Research*, Vol. 9, No. 1, (1994), 180-187. <https://doi.org/10.1557/JMR.1994.0180>
2. Yang, Y., Ong, J. L., Tian, J., "Rapid sintering of hydroxyapatite

- by microwave processing", *Journal of Materials Science Letters*, Vol. 21, No. 1, (2002), 67-69. <https://doi.org/10.1023/A:1014250813564>
3. Ehsani, N., Sorrell, C. C., Ruys, A. J., "Microwave Hybrid Processing of Hydroxyapatite", *Journal of Biomimetics, Biomaterials & Tissue Engineering*, Vol. 18, No. 1, (2013), 108. <https://doi.org/10.4172/1662-100X.1000108>
4. Wu, Q., Zhang, X., Wu, B., Huang, W., "Effects of microwave sintering on the properties of porous hydroxyapatite scaffolds", *Ceramic International*, Vol. 39, No. 3, (2013), 2389-2395. <https://doi.org/10.1016/j.ceramint.2012.08.091>
5. Tovstonoh, H., Sych, O., Skorokhod, V., "Microwave sintering of biogenic hydroxyapatite ceramics for reconstructive surgery", *Processing of Applied Ceramics*, Vol. 8, No.1, (2014), 1-5. <https://doi.org/10.2298/PAC1401001T>
6. Gu, Y. W., Loh, N. H., Khor, K. A., Tor, S. B., Cheang, P., "Spark plasma sintering of hydroxyapatite powders", *Biomaterials*, Vol. 23, No. 1, (2002), 37-43. [https://doi.org/10.1016/S0142-9612\(01\)00076-X](https://doi.org/10.1016/S0142-9612(01)00076-X)
7. Venkateswarlu, K., Bose, A. C., Rameshbabu, N., "X-ray peak broadening studies of nanocrystalline hydroxyapatite by Williamson-Hall analysis", *Physica B: Condensed Matter*, Vol. 405, No. 20, (2010), 4256-4261. <https://doi.org/10.1016/j.physb.2010.07.020>
8. Chen, C., Huang, Z., Yuan, W., Li, J., Cheng, X., Chi, R. A., "Pressure effecting on morphology of hydroxyapatite crystals in homogeneous System", *CrystEngComm*, Vol. 13, No. 5, (2011), 1632-1637. <https://doi.org/10.1039/C0CE00090F>
9. Pajchel, L., Kolodziejski, W., "Solid-state MAS NMR, TEM, and TGA studies of structural hydroxyl groups and water in nanocrystalline apatites prepared by dry milling", *Journal of Nanoparticle Research*, Vol. 15, (2013), 1868. <https://doi.org/10.1007/s11051-013-1868-y>
10. Xu, G. F., Lloyd, I. K., Carmel, Y., Olorunoyemi, T., Wilson, O. C., "Microwave sintering of ZnO at ultra high heating rates", *Journal of Materials Research*, Vol. 16, No. 10, (2001), 2850-2858. <https://doi.org/10.1557/JMR.2001.0393>
11. Sinitsyna, O. V., Veresov, A. G., Kovaleva, E. S., Kolen'ko, Y. V., Putlyaev, V. I., Tretyakov, Y. D., "Synthesis of hydroxyapatite by hydrolysis of  $\alpha$ -Ca<sub>3</sub>(PO<sub>4</sub>)<sub>2</sub>", *Russian Chemistry Bulletin*, Vol. 54, No. 1, (2005), 79-86. <http://doi.org/10.1007/s11172-005-0220-9>
12. Țălu, S., "Special Issue: Characterizations of Three-Dimensional Surfaces at Micro/Nanoscale", *Applied Sciences*, Vol. 12, No. 15, (2022), 7729. <https://doi.org/10.3390/app12157729>
13. Mwema, F. M., Akinlabi, E. T., Oladijo, O. P., Fatoba, O. S., Akinlabi, S. A., Țălu, S., "Chapter two - Advances in manufacturing analysis: fractal theory in modern manufacturing", In Kumar, K., Davim, J. P., (Eds.), *Woodhead Publishing Reviews: Mechanical Engineering Series, Modern Manufacturing Processes*, Woodhead Publishing, Cambridge, UK, (2020), 13-39. <https://doi.org/10.1016/B978-0-12-819496-6.00002-6>



Materials and Energy Research Center

MERC

Contents lists available at [ACERP](#)

Advanced Ceramics Progress

Journal Homepage: [www.acerp.ir](http://www.acerp.ir)

Advanced Ceramics Progress

## Original Research Article

# Preparation of Nanocomposite of TiO<sub>2</sub> Nanoparticles and CuS Nanoflakes for Visible-Light Photocatalytic Decomposition of Nitenpyram Pesticide

Ghader Hosseinzadeh <sup>a, \*</sup><sup>a</sup> Associate Professor, Department of Chemical Engineering, Faculty of Engineering, University of Bonab, Bonab, East Azerbaijan, Iran\* Corresponding Author Email: [g.hosseinzadeh@ubonab.ac.ir](mailto:g.hosseinzadeh@ubonab.ac.ir) (G. Hosseinzadeh)URL: [https://www.acerp.ir/article\\_160987.html](https://www.acerp.ir/article_160987.html)

## ARTICLE INFO

## A B S T R A C T

## Article History:

Received 5 October 2022  
 Received in revised form 13 November 2022  
 Accepted 21 November 2022

## Keywords:

Nanocomposite  
 Nitenpyram  
 Photocatalyst  
 CuS  
 TiO<sub>2</sub>

In this study, a novel TiO<sub>2</sub>-CuS heterojunction nanocomposite was prepared from TiO<sub>2</sub> anatase nanoparticles and CuS nanoflakes through hydrothermal method and used, for the first time, as a visible-light photocatalyst for decomposition of agricultural insecticide Nitenpyram. Crystallinity, shape, and size of particles, and optical properties of the prepared nanocomposite were investigated using FESEM, XRD, Mott-Schottky, photoluminescence (PL), and UV-Visible spectroscopy analyses. The results indicated that the TiO<sub>2</sub>-CuS heterojunction nanocomposite was successfully prepared and compared to the pure CuS and TiO<sub>2</sub> semiconductors, it exhibited a better photocatalytic performance mainly due to the improvement in optical properties (increasing the ability of visible-light absorbance) and reduction of the photoinduced electron and hole recombination rate. According to the Mott-Schottky analysis and radical scavenger tests, superoxide radical was detected as the major oxidizing agent involved in photocatalytic degradation of Nitenpyram, and a type II charge transfer pathway was suggested to improve the photocatalytic activity.

<https://doi.org/10.30501/acp.2022.364273.1104>

## 1. INTRODUCTION

Nitenpyram is used as one of the most important commercial insecticides owing to its high insecticidal activity, suitable water solubility, and broad spectrum [1]. However, given the widespread use of insecticides in agriculture, they are frequently found in groundwater, soil, and rivers, hence recognized as a serious environmental pollution [2]. In this regard, various techniques including biodegradation with bacteria, membrane reactors, electrochemical degradation, and photocatalytic degradation have been employed to eliminate these compounds from the polluted

environment [3-7]. Among these techniques, advanced oxidation by photocatalysts is an attractive one that is mainly used for degradation of these contaminants [8,9].

TiO<sub>2</sub>, as a popular semiconductor, has attracted considerable attention for photocatalytic decomposition of different inorganic and organic pollutants. The superiority of TiO<sub>2</sub> to its counterparts lies in its unique characteristics including high stability, less toxicity, low cost, and high oxidation power of the photoinduced charge carriers [10]. However, due to its wide band gap, TiO<sub>2</sub> has low activity under visible light. Another notable drawback is its fast recombination of the photoinduced charge carriers [11]. Therefore, To overcome these

Please cite this article as: Hosseinzadeh, G., "Preparation of Nanocomposite of TiO<sub>2</sub> Nanoparticles and CuS Nanoflakes for Visible-Light Photocatalytic Decomposition of Nitenpyram Pesticide", *Advanced Ceramics Progress*, Vol. 8, No. 3, (2022), 22-28. <https://doi.org/10.30501/acp.2022.364273.1104>

2423-7485/© 2022 The Author(s). Published by MERC.

This is an open access article under the CC BY license (<https://creativecommons.org/licenses/by/4.0/>).

drawbacks, up to now, a variety of strategies have been developed namely doping with metal or nonmetal elements [12], morphology and surface engineering [13], and constructing heterojunction with other semiconductors [14]. Among these methods, heterojunction photocatalyst have attracted remarkable attention, leading to improved photocatalytic efficiency by expanding the absorption region to the visible-light range and decreasing the recombination rate of the photoinduced electron-hole pairs [15-17].

In recent decades, Copper (II) sulfide (CuS) semiconductor as a p-type semiconductor has gained considerable significance as an efficient photocatalyst for degradation of organic pollutants [13]. However, due to its narrow band gap, CuS enjoys rapid recombination of the photogenerated electron-hole pairs, hence low photocatalytic performance. To address this restriction, numerous methods have been developed to suppress the electron-hole recombination rate among which, this semiconductor is mainly used as the heterojunction composite with other semiconductors [14] such as ZnO/CuS [18], CuS/BiVO<sub>4</sub> [19], CuS/BaTiO<sub>3</sub> [20], and CuS/g-C<sub>3</sub>N<sub>4</sub> [21], to name a few.

In this study, a TiO<sub>2</sub>-CuS heterojunction nanocomposite was prepared with novel morphology from anatase TiO<sub>2</sub> nanoparticles, and CuS nanoflakes via hydrothermal routes and then used for the visible-light photocatalytic decomposition of Nitenpyram. Characterization of the synthesized samples was performed using FESEM, XRD, Mott-Schottky, photoluminescence (PL), and UV-Visible spectroscopy analysis.

## 2. MATERIALS AND METHODS

### 2.1. Materials

Titanium isopropoxide (Ti(OCH(CH<sub>3</sub>)<sub>2</sub>)<sub>4</sub>) triethanolamine, sodium hydroxide, ethanol, Cu(NO<sub>3</sub>)<sub>2</sub>·3H<sub>2</sub>O, thiourea, ethylene glycol were purchased from Merck in high purity.

### 2.2. Synthesis of TiO<sub>2</sub> Nanoparticles

To prepare TiO<sub>2</sub>-anatase nanoparticles, 7 mL of (Ti(OCH(CH<sub>3</sub>)<sub>2</sub>)<sub>4</sub>) and 14 mL of triethanolamine were dispersed in 30 mL water. Then, followed by increasing the pH of the solution up to 10 with 1 M sodium hydroxide solution, the final solution was stirred for 12 hours. The resulting gel was subjected to the hydrothermal process in a Teflon-lined autoclave for 24 hours at the temperature of 140 °C. The precipitated nanoparticle was extracted by centrifuging and followed by washing with water and ethanol for several times, it was dried at 60 °C.

### 2.3. Synthesis of CuS Nanoflakes

To prepare CuS nanoflakes, Cu(NO<sub>3</sub>)<sub>2</sub>·3H<sub>2</sub>O as a

precursor was dissolved in 15 mL of distilled water and in another beaker, 3 mmol of thiourea was dissolved in 15 mL of ethylene glycol. Next, the contents of these solutions were mixed together under ultrasonication. Then, the final mix was subjected to the hydrothermal process in a Teflon-lined autoclave for 12 hours at the temperature of 150 °C. The resultant nanoflakes were separated out by centrifuging and after washing with ethanol and deionized water for several times, they were dried at 60 °C.

### 2.4. Synthesis of TiO<sub>2</sub>-CuS Nanocomposite

In a typical process, for synthesis of the TiO<sub>2</sub>-CuS heterojunction nanocomposite, 0.5 g of anatase TiO<sub>2</sub> nanoparticles was mixed with 0.5 g of CuS nanoflakes and dispersed in 100 mL water by ultrasonication for 60 min. Then, the final suspension was transformed into a 150 mL Teflon lined stainless autoclave and subjected to the hydrothermal process for 20 h at the temperature of 180 °C. At the end of the process, the resulting nanocomposite was separated using a centrifuge, washed several times with deionized ethanol and water, and dried in a vacuum oven at 60 °C.

### 2.5. Photocatalytic Activity

For better evaluation of the photocatalytic performance of the fabricated samples, photocatalytic decomposition of Nitenpyram was done under 570 W Xenon lamp illumination. In this experiment, the reaction solution containing 0.05 g of the dispersed photocatalyst, 3 mg of Nitenpyram, and 100 mL of deionized water was mixed and kept in a dark under-stirring condition to develop adsorption-desorption equilibrium prior to irradiation. Then, the obtained suspension was irradiated with the visible light. After the time intervals, Degradation Percentage (DP) of Nitenpyram was analyzed using CARY 100 Bio VARIAN UV-Visible spectrophotometer.

## 3. RESULTS AND DISCUSSION

The crystallinity of the prepared samples were examined based on X-Ray Diffraction (XRD) analysis on X'Pert MPD diffractometer using Cu K $\alpha$  line radiation. The XRD patterns are illustrated in Figure 1.

For CuS nanoflakes, the peaks at  $2\theta = 27.61^\circ$ ,  $29.41^\circ$ ,  $31.81^\circ$ ,  $32.61^\circ$ ,  $48.01^\circ$ , and  $52.81^\circ$  can be indexed to the diffractions from (101), (102), (103), (006), (110), and (108) lattice planes, respectively, corresponding to the CuS hexagonal (covellite) structure (JCPDS 006-0464) [22].

For TiO<sub>2</sub> nanoparticles, the major diffraction peaks positioned at  $2\theta = 25.3^\circ$ ,  $37.6^\circ$ ,  $47.9^\circ$ ,  $54.5^\circ$ , and  $62.5^\circ$  can be indexed to the diffraction from (101), (004), (200), (105), and (204) lattice planes of the anatase titanium dioxide phase (JCPDS #21-1272), respectively [23]. In

the XRD spectrum of the TiO<sub>2</sub>-CuS heterojunction nanocomposite, the diffraction peaks of CuS and TiO<sub>2</sub> are vividly observed, indicating the successful preparation of the heterojunction nanocomposite. The existence of sharp diffraction peaks confirms the high crystallinity of the synthesized samples.

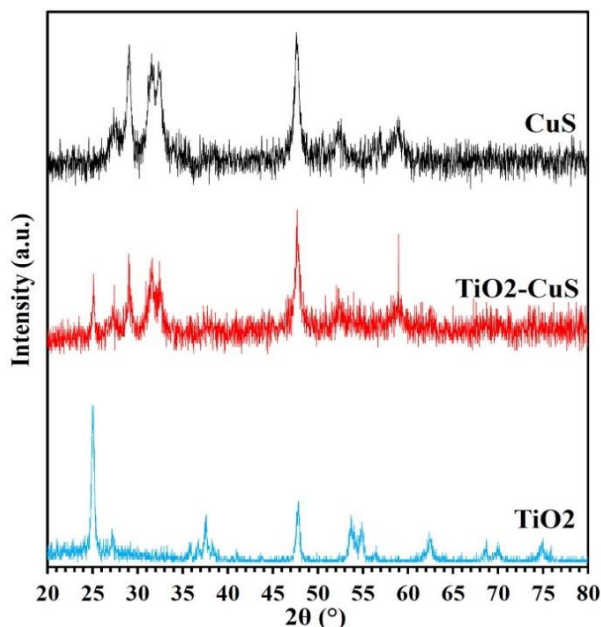


**Figure 1.** XRD patterns of the prepared samples

Once FE-SEM analysis is carried out on Tescan MIRA 3 FESEM, obtaining information about the size and morphology of the nanostructures that make up the nanocomposite is made possible. The FE-SEM results for the prepared TiO<sub>2</sub>-CuS nanocomposite are shown in Figure 2a where the TiO<sub>2</sub> nanoparticles of about 40 nm in size and CuS nanoflakes of about 20 nm in thickness can be identified. To confirm the presence of TiO<sub>2</sub> and CuS compounds in the TiO<sub>2</sub>-CuS nanocomposite, EDS analysis was carried out on the TiO<sub>2</sub>-CuS sample to identify the elemental composition and confirm the presence of CuS and TiO<sub>2</sub> in this sample. The peaks of Ti, S, O, and Cu elements are vividly observed in the EDS spectrum of TiO<sub>2</sub>-CuS sample in Figure 2b, confirming the successful preparation of the TiO<sub>2</sub>-CuS heterojunction.

The optical properties of the prepared samples were examined through UV-Vis Diffuse Reflectance Spectroscopy (UV-DRS) on Shimadzu UV-2550 UV-vis spectrophotometer. Figure 3 demonstrate the obtained UV-Vis diffuse reflectance spectra of the samples according to which, the absorption edge of the TiO<sub>2</sub>-CuS heterojunction shows a red-shift, compared to the bare TiO<sub>2</sub>; hence, composition of the TiO<sub>2</sub> with CuS can improve the visible-light capture efficiency of TiO<sub>2</sub>. The band gap energy ( $E_g$ ) of the samples was obtained based

on the Kubelka–Munk model [24]. As seen in Figure 3b, the obtained value of  $E_g$  for TiO<sub>2</sub> is 3.2 eV while the value of  $E_g$  for TiO<sub>2</sub>-CuS heterojunction sample is 2.7 eV, confirming the remarkable effect of heterojunction interface formation on the  $E_g$  of TiO<sub>2</sub> reduction which in turn enhances its visible-light photocatalytic performance.

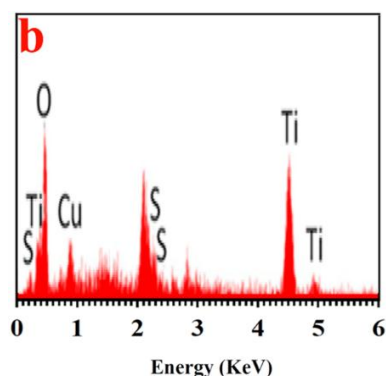
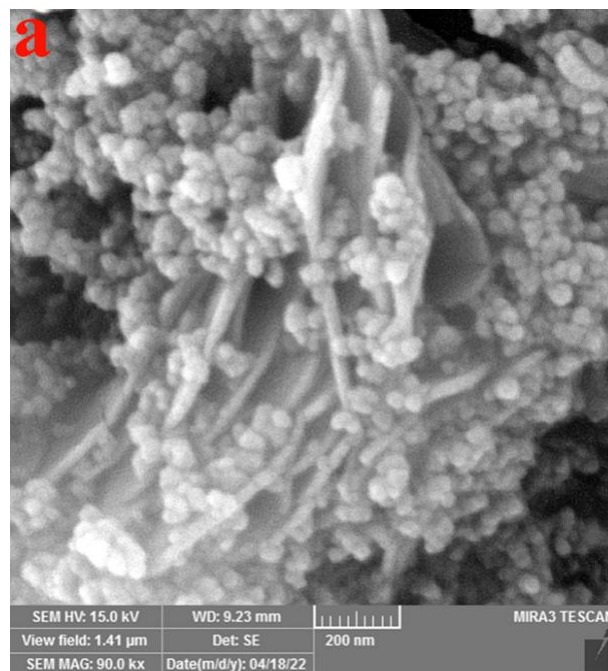


**Figure 2.** FE-SEM image (a) and EDS spectrum (b) of TiO<sub>2</sub>-CuS nanocomposite

PL spectroscopy can be used for predicting the separation of charge carriers on the prepared samples. A decrease in the PL intensity can be attributed to the reduction in the charge carriers' recombination rate, thus resulting in the enhancement of the photocatalytic activity [25]. The emission PL spectra of the obtained samples were derived from Varian Cary-Eclipse 500 fluorescence spectrometer at the excitation wavelength of 300 nm.

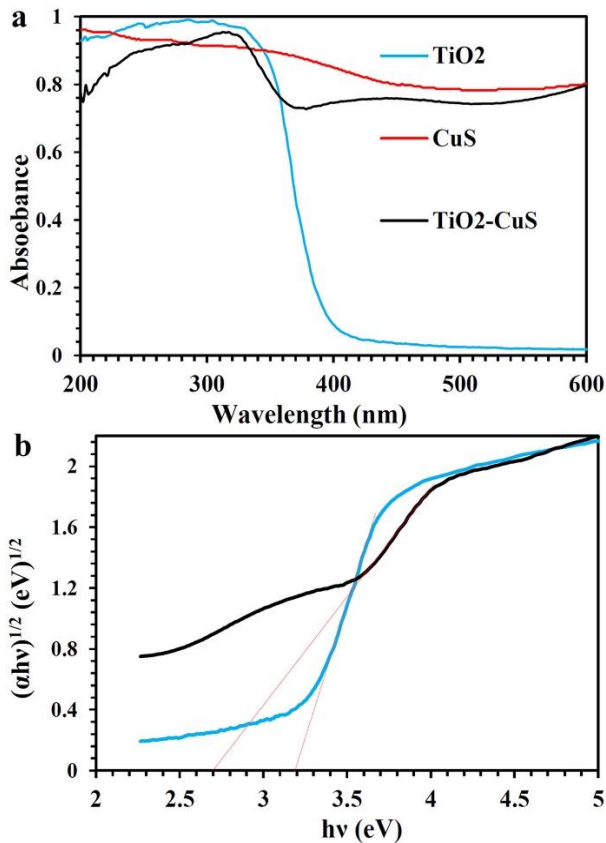


**Figure 3.** (a) UV-Visible DRS spectra and (b) the  $h\nu$  vs  $(\alpha h\nu)^{1/2}$  plots for the estimation of  $E_g$

As shown in Figure 4, the PL emission intensity of the  $\text{TiO}_2$ -CuS heterojunction nanocomposite followed a decreasing trend, compared to the bare  $\text{TiO}_2$  sample. Such decrease in the PL emission intensity can be attributed to the suppressed recombination rate of photoinduced charge carriers. In this regard, due to the decreased recombination rate of the charge carriers on the  $\text{TiO}_2$ -CuS heterojunction, this sample exhibited enhanced photocatalytic performance.

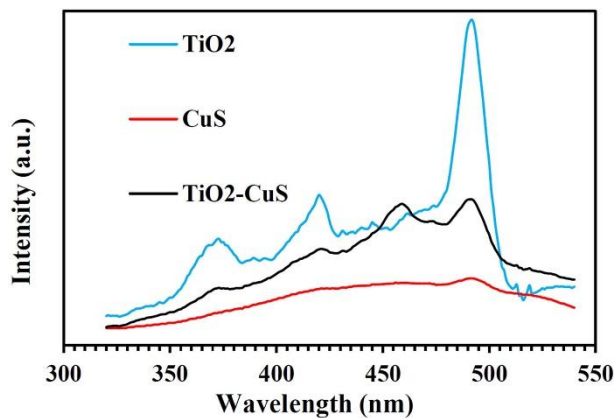


**Figure 4.** Photoluminescence spectra of the  $\text{TiO}_2$ , CuS, and  $\text{TiO}_2$ -CuS samples

The flat-band potential ( $E_{\text{FB}}$ ), conduction band potential ( $E_{\text{C}}$ ), and valance band potential ( $E_{\text{V}}$ ) of the  $\text{TiO}_2$  and CuS samples were estimated based on Mott-Schottky test, as shown in Figure 5. The positive slope of the linear part of the Mott-Schottky curve of  $\text{TiO}_2$  sample reveals that this sample is an n-type semiconductor. However, the negative slope of linear part of the Mott-Schottky curves of CuS sample, indicating that CuS is a p-type semiconductor [26,27]. As observed in Figures 5a and 5b,  $E_{\text{FB}}$  values of CuS and  $\text{TiO}_2$  were measured as approximately +0.5 V and -0.63 V (vs. Ag/AgCl) (+0.7 V and -0.43 V vs. NHE), respectively. As reported in the literature, for n-type semiconductor, the value of  $E_{\text{FB}}$  is 0.1 V lower than  $E_{\text{C}}$  and for p-type semiconductor, it is about  $\sim 0.1$  eV higher than  $E_{\text{V}}$  [26]. As a result, the  $E_{\text{C}}$  value of the CuS and  $\text{TiO}_2$  samples are equal to about +0.8 and -0.53 eV vs. NHE, respectively. In addition, the  $E_{\text{V}}$  value of the CuS and  $\text{TiO}_2$  samples was estimated based on  $E_{\text{V}} = E_{\text{C}} + E_{\text{g}}$  and consequently, the  $E_{\text{V}}$  value of these samples were obtained as 2.67 and 3.4 eV vs. NHE, respectively.

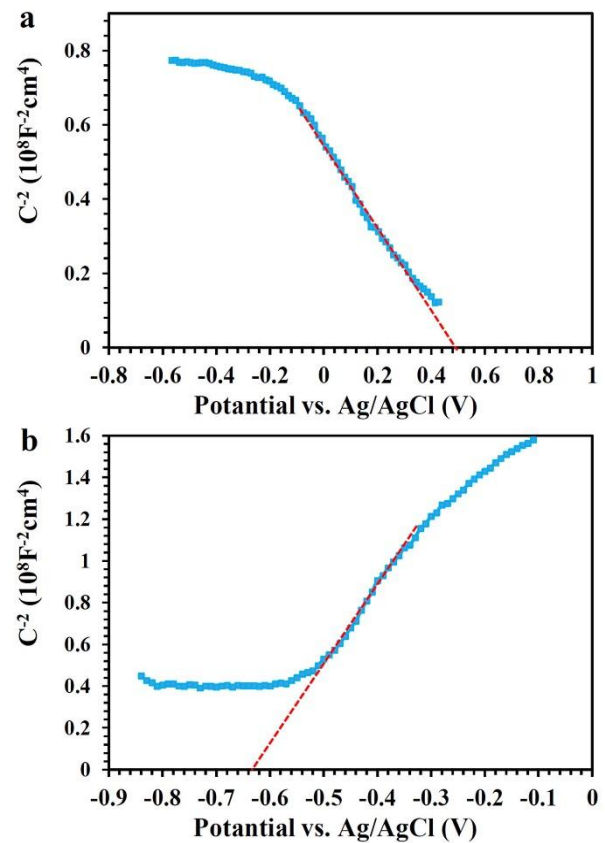


**Figure 5.** Mott-Schottky (MS) plots of (a) CuS and (b)  $\text{TiO}_2$  samples

The photocatalytic activities of the fabricated photocatalysts were evaluated by comparing the photocatalytic decomposition of Nitrophenol over the

synthesized samples under visible-light illumination. As shown in Figure 6, in the case of the absence of photocatalyst (Blank), no degradation of Nitenpyram is reported, confirming the stability of this insecticide under visible-light illumination. However, remarkable degradation was observed in the presence of  $\text{TiO}_2$ , CuS, and  $\text{TiO}_2$ -CuS heterojunction nanocomposite, and about 52%, 24%, and 100% of Nitenpyram was decomposed in 60 min of irradiation, respectively. Due to the improvement in the visible-light capturing and also the retarded recombination rates of electron-hole pairs on the  $\text{TiO}_2$ -CuS heterojunction samples, this sample shows remarkably enhanced photocatalytic performance.

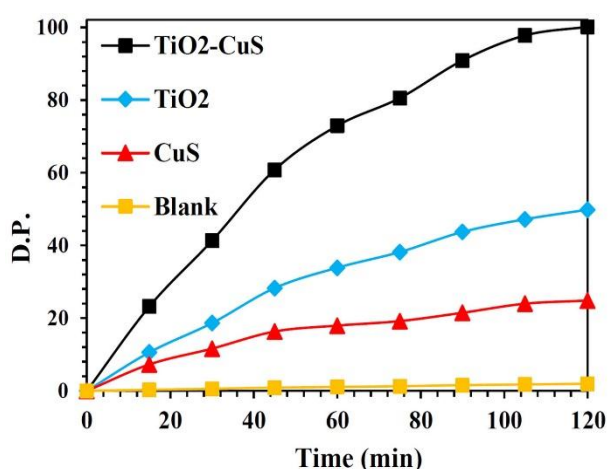
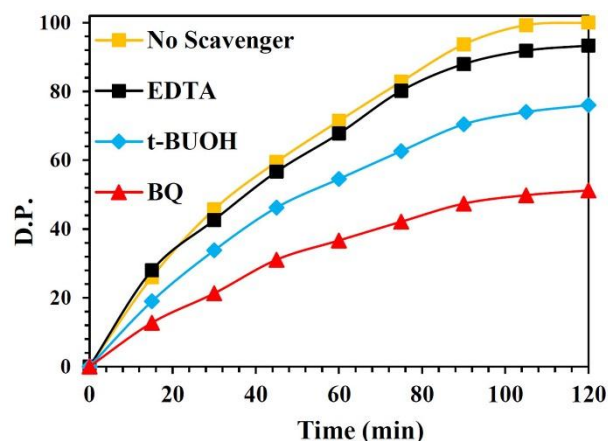


**Figure 6.** Visible-light photocatalytic degradation of Nitenpyram by using the synthesized samples

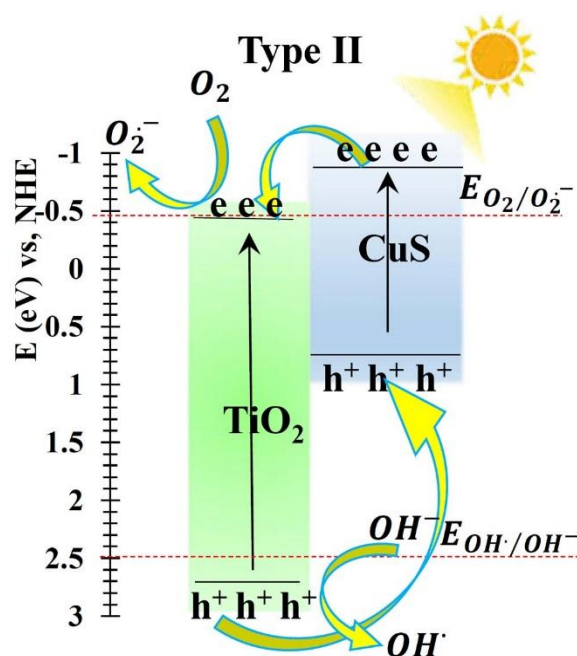
To further evaluate the roles of superoxide radical ( $\text{O}_2^{\cdot-}$ ), hydroxyl radical ( $\text{OH}^{\cdot}$ ), and hole on the photocatalytic decomposition of Nitenpyram on the  $\text{TiO}_2$ -CuS nanocomposite, benzoquinone (BQ), tert-Butyl alcohol (t-BUOH), and Ethylenediaminetetraacetic acid (EDTA) were added to the reaction solution as the scavengers of these species, respectively [28]. As demonstrated in Figure 7, the highest reduction in the photocatalytic efficiency was witnessed in the presence of BQ, confirming the major role of superoxide radicals during the photocatalytic decomposition of Nitenpyram. Of note, the photocatalytic degradation was also retarded in the presence of t-BUOH. Therefore, hydroxyl and superoxide radicals are the major oxidizing species responsible for photocatalytic activity of  $\text{TiO}_2$ -CuS nanocomposite under visible-light illumination.

Figure 8 shows the schematic diagram of the band alignment and type II charge carriers transfer mechanism for the photocatalytic performance of the  $\text{TiO}_2$ -CuS heterojunction during the visible-light illumination of the heterojunction photocatalyst. When light is irradiated onto this sample, the electron-hole pairs are generated in these semiconductors.

The photo-induced electron on the CB of CuS migrates to the CB of  $\text{TiO}_2$  and at the same time, the hole on the VB of  $\text{TiO}_2$  migrates to the VB of CuS [29]. Consequently, recombination of charge carriers considerably decreased, and the lifetime of the photogenerated electrons and holes remarkably increased. As a result, more  $\text{OH}^{\cdot}$  and  $\text{O}_2^{\cdot-}$  radicals were produced, and the oxidizing power of the photogenerated holes and electrons was enhanced, hence photocatalytic efficiency improvement.



**Figure 7.** Activities of  $\text{TiO}_2$ -CuS nanocomposite for the visible-light photocatalytic decomposition of Nitenpyram in existence of various scavengers



**Figure 8.** Type II mechanism for the photocatalytic performance of  $\text{TiO}_2$ -CuS nanocomposite

#### 4. CONCLUSION

In the present research, a novel type II heterojunction nanocomposite was synthesized through one-step hydrothermal method from TiO<sub>2</sub> nanoparticles and CuS nanoflakes and then used as a visible-light photocatalyst for decomposition of Nitenpyram insecticide. Based on the obtained results, TiO<sub>2</sub>-CuS heterojunction nanocomposite exhibited the best photocatalytic performance owing to a decrease in the electron-hole recombination rate and an increasing in the visible-light capturing. According to the results from Mott-Schottky tests and radical trapping experiments, a type II charge transfer mechanism was proposed for the degradation of Nitenpyram, and superoxide radicals were recognized as the major oxidizing agents involved in the degradation reaction.

#### ACKNOWLEDGEMENTS

The author would like to acknowledge University of Bonab for providing the financial support.

#### REFERENCES

- Liu, J., Xiong, W. H., Ye, L. Y., Zhang, W. S., Yang, H., "Developing a novel nanoscale porphyrinic metal-organic framework: a bifunctional platform with sensitive fluorescent detection and elimination of nitenpyram in agricultural environment", *Journal of Agricultural and Food Chemistry*, Vol. 68, No. 20, (2020), 5572-5578. <https://doi.org/10.1021/acs.jafc.0c01313>
- DiBartolomeis, M., Kegley, S., Mineau, P., Radford, R., Klein, K., "An assessment of acute insecticide toxicity loading (AITL) of chemical pesticides used on agricultural land in the united states", *PloS One*, Vol. 14, No. 8, (2019), e0220029. <https://doi.org/10.1371/journal.pone.0220029>
- Priya, R., Ramesh, D., Khosla, E., "Biodegradation of pesticides using density-based clustering on cotton crop affected by xanthomonas malvacearum", *Environment, Development and Sustainability*, Vol. 22, No. 2, (2020), 1353-1369. <https://doi.org/10.1007/s10668-018-0251-7>
- Dumée, L. F., Maina, J. W., Merenda, A., Reis, R., He, L., Kong, L., "Hybrid thin film nano-composite membrane reactors for simultaneous separation and degradation of pesticides", *Journal of Membrane Science*, Vol. 528, (2017), 217-224. <https://doi.org/10.1016/j.memsci.2017.01.041>
- Narayanan, N., Gupta, S., Gajbhiye, V. T., "Decontamination of pesticide industrial effluent by adsorption-coagulation-flocculation process using biopolymer-nanoorganoclay composite", *International Journal of Environmental Science and Technology*, Vol. 17, No. 12, (2020), 4775-4786. <https://doi.org/10.1007/s13762-020-02785-y>
- Wang, R., Pan, J., Qin, M., Guo, T., "Molecularly imprinted nanocapsule mimicking phosphotriesterase for the catalytic hydrolysis of organophosphorus pesticides", *European Polymer Journal*, Vol. 110, (2019), 1-8. <https://doi.org/10.1016/j.eurpolymj.2018.10.045>
- Bhat, A. P., Gogate, P. R., "Degradation of nitrogen-containing hazardous compounds using advanced oxidation processes: A review on aliphatic and aromatic amines, dyes, and pesticides", *Journal of Hazardous Materials*, Vol. 403, (2021), 123657. <https://doi.org/10.1016/j.jhazmat.2020.123657>
- Azari, B., Pourahmad, A., Sadeghi, B., Mokhtary, M., "Incorporation of zinc oxide nanoparticles in RHA-MTW zeolite and its application for degradation of dye", *Journal of Nanoanalysis*, Vol. 7, No. 3, (2020), 179-189. [https://jnanoanalysis.tms.iau.ir/article\\_680020.html](https://jnanoanalysis.tms.iau.ir/article_680020.html)
- Rostami, M., Hassani Joshaghani, A., Mazaheri, H., Shokri, A., "Photo-degradation of p-nitro toluene using modified bentonite based nano-TiO<sub>2</sub> photocatalyst in aqueous solution", *International Journal of Engineering*, Vol. 34, No. 4, (2021), 756-762. <https://doi.org/10.5829/ije.2021.34.04a.01>
- Lee, S. Y., Park, S. J., "TiO<sub>2</sub> photocatalyst for water treatment applications", *Journal of Industrial and Engineering Chemistry*, Vol. 19, No. 6, (2013), 1761-1769. <https://doi.org/10.1016/j.jiec.2013.07.012>
- Rahmi, R., Lubis, S., Az-Zahra, N., Puspita, K., Iqhrammullah, M., "Synergetic photocatalytic and adsorptive removals of metanil yellow using TiO<sub>2</sub>/grass-derived cellulose/chitosan (TiO<sub>2</sub>/GC/CH) film composite", *International Journal of Engineering*, Vol. 34, No. 8, (2021), 1827-1836. <https://doi.org/10.5829/ije.2021.34.08b.03>
- Basavarajappa, P. S., Patil, S. B., Ganganagappa, N., Reddy, K. R., Raghu, A. V., Reddy, C. V., "Recent progress in metal-doped TiO<sub>2</sub>, non-metal doped/codoped TiO<sub>2</sub> and TiO<sub>2</sub> nanostructured hybrids for enhanced photocatalysis", *International Journal of Hydrogen Energy*, Vol. 45, No. 13, (2020), 7764-7778. <https://doi.org/10.1016/j.ijhydene.2019.07.241>
- Zhao, W., Adeel, M., Zhang, P., Zhou, P., Huang, L., Zhao, Y., Ahmad, M. A., Shakoor, N., Lou, B., Jiang, Y., Lynch, I., "A critical review on surface-modified nano-catalyst application for the photocatalytic degradation of volatile organic compounds", *Environmental Science: Nano*, Vol. 9, No. 1, (2022), 61-80. <https://doi.org/10.1039/D1EN00955A>
- Meng, A., Zhang, L., Cheng, B., Yu, J., "Dual cocatalysts in TiO<sub>2</sub> photocatalysis", *Advanced Materials*, Vol. 31, No. 30, (2019), 1807660. <https://doi.org/10.1002/adma.201807660>
- Yang, H., "A short review on heterojunction photocatalysts: Carrier transfer behavior and photocatalytic mechanisms", *Materials Research Bulletin*, Vol. 142, (2021), 111406. <https://doi.org/10.1016/j.materresbull.2021.111406>
- Bahadoran, A., Farhadian, M., Hoseinzadeh, G., Liu, Q., "Novel flake-like Z-Scheme Bi<sub>2</sub>WO<sub>6</sub>-ZnBi<sub>2</sub>O<sub>4</sub> heterostructure prepared by sonochemical assisted hydrothermal procedures with enhanced visible-light photocatalytic activity", *Journal of Alloys and Compounds*, Vol. 883, (2021), 160895. <https://doi.org/10.1016/j.jallcom.2021.160895>
- Kohestani, H., Ezoji, R., "Synthesis and characterization of TiO<sub>2</sub>/CuO/WO<sub>3</sub> ternary composite and its application as photocatalyst", *International Journal of Engineering*, Vol. 34, No. 3, (2021), 721-727. <https://doi.org/10.5829/ije.2021.34.03c.17>
- Kaushik, B., Yadav, S., Rana, P., Solanki, K., Rawat, D., Sharma, R. K., "Precisely engineered type II ZnO-CuS based heterostructure: A visible light driven photocatalyst for efficient mineralization of organic dyes", *Applied Surface Science*, Vol. 590, (2022), 153053. <https://doi.org/10.1016/j.apsusc.2022.153053>
- Lai, C., Zhang, M., Li, B., Huang, D., Zeng, G., Qin, L., Liu, X., Yi, H., Cheng, M., Li, L., Chen, Z., Chen, L., "Fabrication of CuS/BiVO<sub>4</sub> (0 4 0) binary heterojunction photocatalysts with enhanced photocatalytic activity for ciprofloxacin degradation and mechanism insight", *Chemical Engineering Journal*, Vol. 358, (2019), 891-902. <https://doi.org/10.1016/j.cej.2018.10.072>
- Wang, Y., Li, R., Sun, X., Xian, T., Yi, Z., Yang, H., "Photocatalytic application of ag-decorated CuS/BaTiO<sub>3</sub> composite photocatalysts for degrading RhB", *Journal of Electronic Materials*, Vol. 50, No. 5, (2021), 2674-2686.

- <https://doi.org/10.1007/s11664-021-08787-x>
21. Goudarzy, F., Zolgharnein, J., Ghasemi, J. B., "Determination and degradation of Carbamazepine using g-C<sub>3</sub>N<sub>4</sub>@CuS nanocomposite as sensitive fluorescence sensor and efficient photocatalyst", *Inorganic Chemistry Communications*, Vol. 141, (2022), 109512. <https://doi.org/10.1016/j.inoche.2022.109512>
  22. Lee, J. H., Kim, T., Kim, E. R., Cho, E. B., Jung, S. C., "Microwave-assisted synthesis of various Cu<sub>2</sub>O/Cu/TiO<sub>2</sub> and Cu<sub>x</sub>S/TiO<sub>2</sub> composite nanoparticles towards visible-light photocatalytic applications", *Materials Chemistry and Physics*, Vol. 259, (2021), 123986. <https://doi.org/10.1016/j.matchemphys.2020.123986>
  23. Jesus, M. A. M. L., Ferreira, A. M., Lima, L. F. S., Batista, G. F., Mambrini, R. V., Mohallem, N. D. S., "Micro-mesoporous TiO<sub>2</sub>/SiO<sub>2</sub> nanocomposites: Sol-gel synthesis, characterization, and enhanced photodegradation of quinoline", *Ceramics International*, Vol. 47, No. 17, (2021), 23844-23850. <https://doi.org/10.1016/j.ceramint.2021.05.092>
  24. Landi Jr, S., Segundo, I. R., Freitas, E., Vasilevskiy, M., Carneiro, J., Tavares, C. J., "Use and misuse of the Kubelka-Munk function to obtain the band gap energy from diffuse reflectance measurements", *Solid State Communications*, Vol. 341, (2022), 114573. <https://doi.org/10.1016/j.ssc.2021.114573>
  25. Liqiang, J., Yichun, Q., Baiqi, W., Shudan, L., Baojiang, J., Libin, Y., Wei, F., Honggang, F., Jiazhong, S., "Review of photoluminescence performance of nano-sized semiconductor materials and its relationships with photocatalytic activity", *Solar Energy Materials and Solar Cells*, Vol. 90, No. 12, (2006), 1773-1787. <https://doi.org/10.1016/j.solmat.2005.11.007>
  26. Gelderman, K., Lee, L., Donne, S. W., "Flat-band potential of a semiconductor: Using the Mott-Schottky equation", *Journal of Chemical Education*, Vol. 84, No. 4, (2007), 685. <https://doi.org/10.1021/ed084p685>
  27. Hosseinzadeh, G., Zinatloo-Ajabshir, S., Yousefi, A., "Innovative synthesis of a novel ZnO/ZnBi<sub>2</sub>O<sub>4</sub>/graphene ternary heterojunction nanocomposite photocatalyst in the presence of tragacanth mucilage as natural surfactant", *Ceramics International*, Vol. 48, No. 5, (2022), 6078-6086. <https://doi.org/10.1016/j.ceramint.2021.11.146>
  28. Khalid, N., Ishtiaq, H., Ali, F., Tahir, M. B., Naeem, S., Ul-Hamid, A., Ikram, M., Iqbal, T., Kamal, M. R., Alrobei, H., Alzaid, M., Dahshan, A., "Synergistic effects of Bi and N doped on ZnO nanorods for efficient photocatalysis", *Materials Chemistry and Physics*, Vol. 289, (2022), 126423. <https://doi.org/10.1016/j.matchemphys.2022.126423>
  29. Kim, D., Yong, K., "Boron doping induced charge transfer switching of a C<sub>3</sub>N<sub>4</sub>/ZnO photocatalyst from Z-scheme to type II to enhance photocatalytic hydrogen production", *Applied Catalysis B: Environmental*, Vol. 282, (2021), 119538. <https://doi.org/10.1016/j.apcatb.2020.119538>



Materials and Energy Research Center  
MERC

Contents lists available at [ACERP](#)

Advanced Ceramics Progress

Journal Homepage: [www.acerp.ir](http://www.acerp.ir)



## Original Research Article

# Cu/Co Bilayers: Study of the Surface Topography, Optical Dispersion Parameters, and Transitions of Carriers

Vali Dalouji <sup>a,\*</sup>, Nasim Rahimi <sup>b</sup>, Ali Reza Souri <sup>c</sup>

<sup>a</sup> Associate Professor, Department of Physics, Faculty of Science, Malayer University, Malayer, Hamadan, Iran

<sup>b</sup> PhD Student, Department of Physics, Faculty of Science, Malayer University, Malayer, Hamadan, Iran

<sup>c</sup> Assistant Professor, Department of Materials Engineering, Faculty of Engineering, Malayer University, Malayer, Hamadan, Iran

\* Corresponding Author Email: [dalouji@yahoo.com](mailto:dalouji@yahoo.com) (V. Dolouji)

URL: [https://www.acerp.ir/article\\_160034.html](https://www.acerp.ir/article_160034.html)

## ARTICLE INFO

### Article History:

Received 10 October 2022  
Received in revised form 1 November 2022  
Accepted 5 November 2022

### Keywords:

Cu-Co Films  
Bearing Area Percentage  
Z-X Topography  
Fractal Dimensions  
Optical Band Gap

## ABSTRACT

In this study, Cu and Cu-Co films were prepared using DC Magnetron sputtering system on silicon substrates. Any increase in the roughness and thickness of films would intensify the scattering of the sputtered atoms and consequently, the atoms would lose enough time to find the lowest energy required by each nanoparticle (NP). The height changes on the surface of the scanned films are indicative of the topological phase of the films. According to the results, the films were not smooth that made them undergo a second phase change. The address layer and thickness changes did not have much effect on the degree of isolation. For this reason, the graphs demonstrated close and identical results. All samples display strong light absorption over the entire spectral range, suggesting that they could bid all light-absorber materials. At the peak of approximately 2.7, the cross-point of  $d(\alpha hv)/d(hv)$  curves yielded optical band gap ( $E_g$ ) values of 2.68 eV, 2.76 eV, 2.85 eV, and 2.73 eV corresponding to the Samples 1 to 4, respectively. The optical conductivity of the films increased upon increasing the energy. The SEM images confirmed that the obtained cobalt nanocrystals was approximately spherical in shape with an average diameter less than 80 nm.

<https://doi.org/10.30501/acp.2022.364382.1107>

## 1. INTRODUCTION

In recent years, considerable attention has been drawn to the synthesis of thin multilayer metallic films and their properties given their wide applications in biocompatible materials as well as electronic and micromechanical devices. As a matter of fact, the properties of thin films are usually substantially influenced by their microstructure and surface morphology. In this respect, investigation of the surface morphology of multilayer

metals plays an important role not only in understanding the growing processes of thin films but also in determining the structure of thin films in order to obtain more favorable physical and chemical properties [1]. AFM analysis is probably the best and most commonly used method for characterizing thin film systems. On the contrary, Direct Current (DC) magnetron-sputtering method has gained more significance in fabricating pure Cu thin films owing to its advantageous characteristics such as high growth rate, low-temperature deposition,

Please cite this article as: Dalouji, V., Rahimi, N., Souri, A. R., "Cu/Co Bilayers: Study of the Surface Topography, Optical Dispersion Parameters, and Transitions of Carriers", *Advanced Ceramics Progress*, Vol. 8, No. 3, (2022), 29-38. <https://doi.org/10.30501/acp.2022.364382.1107>

2423-7485/© 2022 The Author(s). Published by MERC.

This is an open access article under the CC BY license (<https://creativecommons.org/licenses/by/4.0/>).



and good reproducibility [2]. In this study, Cu thin films with a Face-Centered Cubic (FCC) structure were prepared using the DC magnetron-sputtering method. The findings revealed the relation between the Cu-Co films' topological characterizations and band-to-band transitions of the carriers. In addition, the role of Co thickness in improving the quality of Cu films was highlighted. Generally, Cu-Co alloy coatings can be deposited on a substrate surface to produce functional coating/substrate systems presenting enhanced properties. These coatings have several interesting applications depending on the cobalt content in the used alloy and substrate. For instance, low cobalt Cu-Co alloys are characterized by giant magnetoresistance properties. When deposited on silicon, copper, or platinum substrates, these alloys can be used in sensor technology and data storage systems [3]. On the contrary, Cu-Co alloy coatings with high cobalt content produced on other substrates are appropriately utilized for catalytic purposes [4] and anticorrosive coatings [5]. Production of these coatings via electrodeposition can be an appropriate option to decrease the deposition process costs. The difference between the reduction potentials of Cu (II) and Co (II) ions is about -0.60 V, and the simultaneous reduction of both cations on the cathode can only be achieved by using a complexing agent [6]. Despite its toxicity, cyanide has been, for a long time, the most used material in the electrodeposition of copper alloys [6]. In order to reduce the toxicity risk, environmentally-friendly compounds can be used as alternative complexing agents for producing alloy coatings [7]. The use of less toxic electrolytes may also decrease the costs of the electroplating industries, which are directly related to the treatment of effluents as well as the use of reinforced exhaust equipment. Cu-Co alloy coatings can be deposited through either DC or Pulsed Current (PC). Each process affects the mass transport, current distribution, and electrical double layer differently, thus producing coatings with diverse composition, surface roughness, and morphology [8]. Despite the cost and simplicity of the DC, several studies emphasized the utilization of pulsed current in the alloy electrodeposition owing to its beneficial characteristics that in turn could enhance the adhesion, density, resistivity, and ductility of the coatings. In addition, layers with lower porosity, morphological uniformity, and more refined grains can also be achieved [9].

## 2. MATERIALS AND METHODS

In this study, Cu and Cu-Co nanoparticles (NPs) were prepared using DC Magnetron sputtering system on silicon substrates. Silicon was located on the grounded electrode, and Cu and Co targets were attached to the DC source. The Cu and Cu-Co NPs were 8 cm in diameter. The chamber was vacuumed at the base pressure of

$10.7 \times 10^{-3}$  Pa prior to the deposition and then, the pressure increased up to 2.5 Pa by acetylene gas. Film deposition was carried out at room temperature ( $297 \pm 1$ ) while maintaining a constant distance from the electrodes. In the first stage, captured for 15min at the applied voltage of 500 V, the substrate was covered with the material sputtered from the Cu target. The target was replaced with Co, and the deposition process continued at the same voltage for another seven and ten minutes to obtain a Co-Cu bilayer thin film with varying Co thickness values. To remove any possible impurities, substrates were cleaned with distilled water and placed in ethanol and acetone in an ultrasonic cleaner for 10 min. The thickness of the thin films was measured as 100 nm using a quartz crystal monitor during deposition. Transmittance and reflectance measurements of films were done using a Varian Cary-500 spectrophotometer in the range of 200-2700 nm (Varian Inc, CA, USA). AFM was used to image the residual NPs film surface morphology (Veeco-Autoprobe).

## 3. RESULTS AND DISCUSSION

The surface morphology of the films was studied using AFM. It was used in the non-contact AFM mode to study the surface morphology and size of medium film NPs. Figure 1 presents the AFM images of the films according to which, upon adding Co with different thickness values to the Cu NPs, the surface becomes rough, hence the appearance of brighter spots in the AFM images. The AFM images highlight the notable effect of Co thickness on the surface morphology of the film. Following by doping of the Cu-Co thin films, NPs became close to each

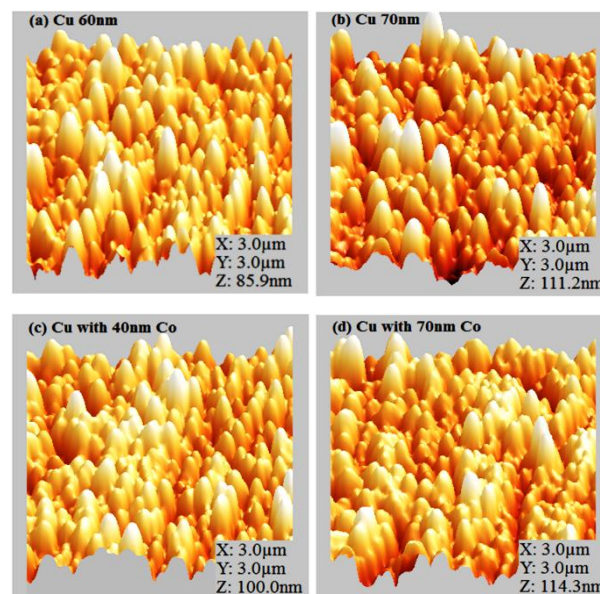


**Figure 1.** AFM images of (a) Cu 60 nm, (b) Cu 70 nm, (c) Cu with 40 nm Co, and (d) Cu with 70 nm Co

other and upon increasing the thickness of Co, the size of the NPs decreased. The RMS roughness of the thin layer with 60 nm Cu, 70 nm Cu, Cu with 40 nm Co, and Cu with 70 nm Co was obtained as 12.2, 15.04, 14.09, and 15.8 nm, respectively.

This increase in the roughness, as the thickness increased, would in turn increase the scattering of the sputtered atoms, and the atoms lose enough time to find the lowest energy for each NP. It should be noted that before the NPs move to the lowest level of energy, the next sputtered particles reach these particles; and the size of these particles increases. As observed, upon increasing the Cu and Co content, the surface becomes rough. The absorption coefficient of the films with 40 and 70 nm Co was higher than all concentration values, resulting in less light scattering. As a result, an increase in the cobalt concentration affected the index of the absorption coefficient of the Cu-Co thin films.

The lateral size of the NP on the film surface can be estimated through the AFM images generally used for elaborating many other physical properties. The lateral size of the NPs for films with 60 nm Cu, 70 nm Cu, Cu with 40 nm Co, and Cu with 70 nm Co were obtained as approximately 40.94, 42.35, 43.76, and 39.53 nm, respectively. Upon increasing the Cu thickness of films up to 70 nm, the lateral sizes of the NPs on the surface of the films first increased and then decreased by increasing the Co thickness of films up to 70 nm. Figure 2 shows the variations in the lateral sizes of the NPs on the surface versus different film thickness values.

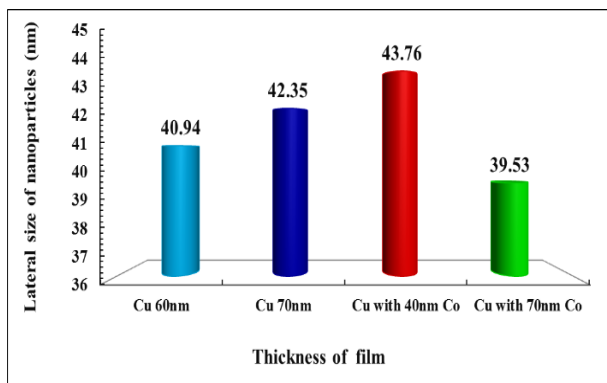


**Figure 2.** Variations of nanoparticle size on the surface of thin films with different thicknesses

Figure 3 shows the variations in the height of the thin films on the surface versus the X and Z axes for the four samples (Cu 60 nm, Cu 70 nm, Cu with 40 nm Co, and Cu with 70 nm Co). The scanning dimensions of the surface of the films was  $3 \times 3 \mu\text{m}^2$  by the AFM; therefore, the maximum numerical value on the X-axis was calculated as  $3 \mu\text{m}$ . The height changes on the surface of the scanned films confirmed the topological phase change of the films with thick layers of Cu 70 nm and Cu

with 40 nm Co films. For the Cu 60 nm and Cu with 40 nm Co thin films, the Z values were about 50 nm while for the Cu 70 nm and Cu with 70 nm Co thin films, these values were about 30 nm. These results show that the films are not smooth and thus they may have a second phase change. The Cu 70 nm NPs have less fluctuations than the others, and the peaks have a milder slope than those of the other samples. The Z ratio of X is closely related and has many peaks.

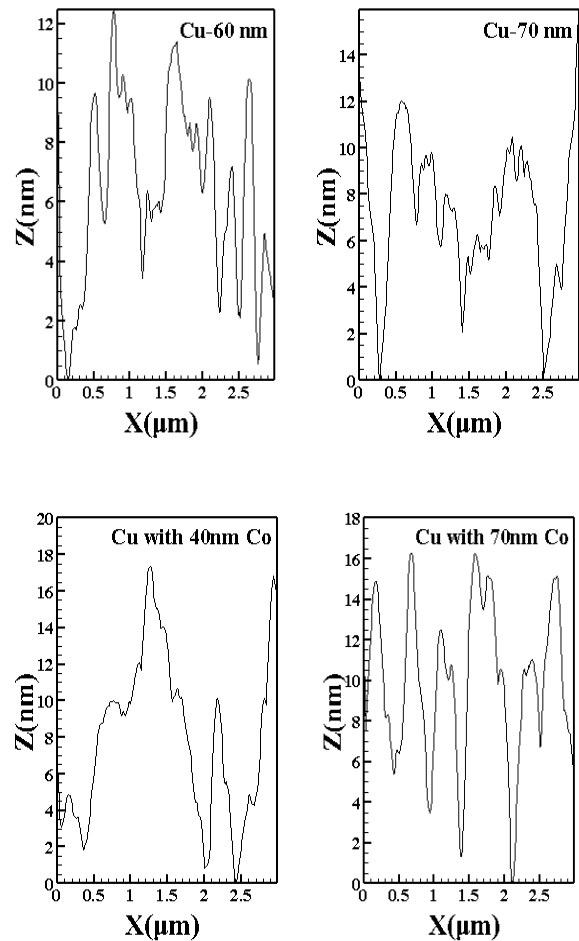


**Figure 3.** Z-height variations of nanoparticles on the surface versus the x-axis for films with different thickness values

Figure 4 shows the PSD spectra extracted from the scanned area of  $3 \times 3 \mu\text{m}^2$  obtained from AFM images of the samples. As observed, all the PSD points include a high spatial frequency region. In Dynamic Scaling Theory (DST), Power Spectral Densities (PSDs) analyses precisely show how the roughness varies with the length scale. The AFM pictures can be divided into pixels as a small square area where the vectors  $h(x_i)$  and  $h(y_j)$  are the height at  $(x_i, y_j)$  positions. Then, the one-dimensional average of PSDs can be obtained through the following formula:

$$(n)=2L/N$$

$$[\langle \sum_{i=1}^{N/2} (\text{FFT}(h(x_i))^2) \rangle_y + \langle \sum_{i=1}^{N/2} \Sigma (\text{FFT}(h(y_j))^2) \rangle_x] \quad (1)$$

where FFT is the fast Fourier transform between the real and mutual spaces.

Due to the dynamical scaling theory, the relation  $P(k)$  and frequency  $k$  are given below for a system with lateral size  $L$  [10]:

$$P(k) \propto k^{-\beta} \quad (2)$$

Generally,  $\beta$  is obtained from the slope of the log-log in the PSD spectra of high spatial frequency. The fractal dimensions  $D_f$  of the films are obtained by finding the  $\beta$  slope value of the log-log diagram [10]:

$$D_f = 4 + \beta/2 \quad (3)$$

Figure 4 illustrates the graphs of the spectral density change of the spatial frequency for the four samples (Cu 60 nm, Cu 70 nm, Cu with 40 nm Co, and Cu with 70 nm Co). The spectral compaction power of all samples reflects the inverse current power variations, especially in the high spatial frequency region, indicating the attendance of the fractal components in outstanding the topographies. These quantities determine the relative amounts of the surface disorder at different distance scales. The spectral performance diagrams of the samples are consistent. However, with an increase in the thickness, the performance of the spectral compaction power would be considerably improved mainly due to the increases in the size of the NPs with the maximum values in the Cu with 40 and 70 nm Co thin films.

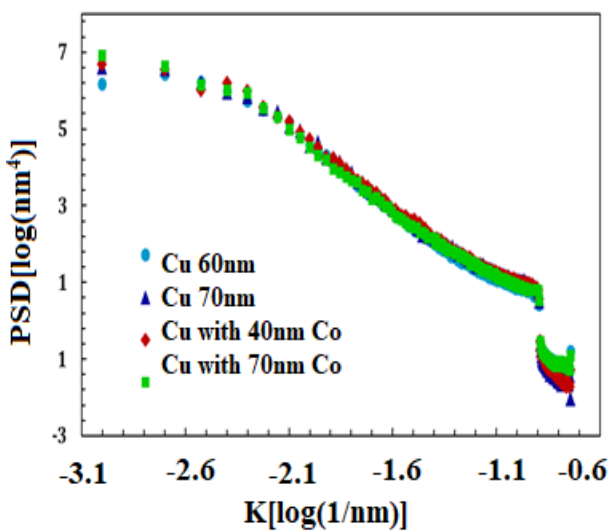


Figure 4. Variations of the power spectral density of the films versus frequency  $k$  of the samples

Figure 5 lists the values of the fractal dimensions of the films for the four samples (Cu 60 nm, Cu 70 nm, Cu with 40 nm Co, and Cu with 70 nm Co) with different thickness values, clearly indicating the dependency of the values of the fractal dimensions on the thickness. The values of the fractal dimensions of Cu 60 nm, Cu 70 nm, Cu with 40 nm Co, and Cu with 70 nm Co thin films were estimated to be 2.72, 2.80, 2.87, and 2.68, respectively. Therefore, it can be concluded that the fractal dimensions of films would increase with an increase in the thickness and doping; however, in the case of Cu with 70 nm Co, the dimensions decreased.

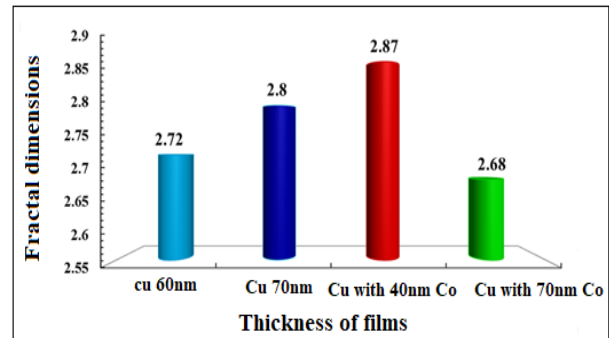
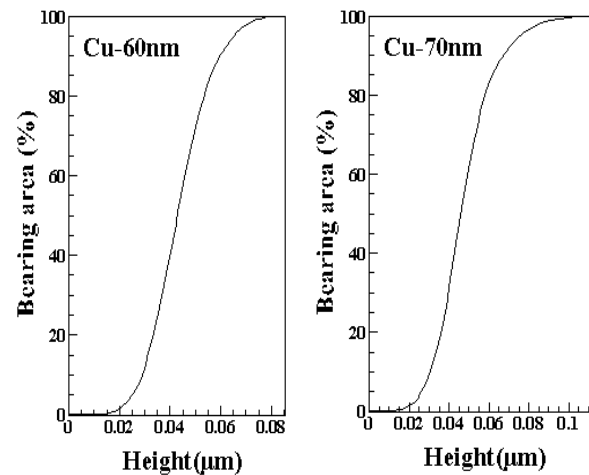
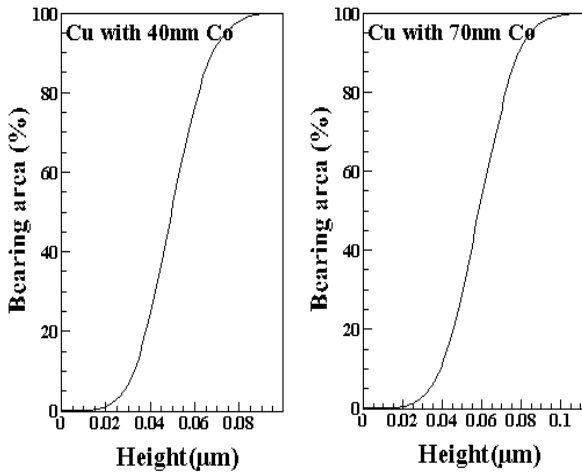


Figure 5. The fractal dimensions of the films at different thickness values

Figure 6 shows the bearing area relative to the height and in fact, it shows the amount of vacuum, zero-coverage (cavity, lower curve of the graph), single-layer (upper curve of the graph), and isolation (we are between the cavity and single-layer) layers.

Figure 6 shows the changes in the bearing area of the four samples. The Cu 60 nm and Cu with 40 nm Co have a cavity coverage of less than 10 % and layer content of about 100 %, which has about 90 % monolayer height. In the vacuum case, the coating is zero, and the content of the Cu 70 nm and Cu with 40 nm Co films are about 95 %, 90 % of which is isolated. The address layer and





**Figure 6.** Variations of the bearing area versus height of the films versus height of the samples

Thickness changes did not have much effect on the degree of isolation; hence, both graphs show close and identical results.

The spectral transmittance  $T$  and reflectance  $R$  of films were measured at normal incidence in the wavelength range of 200-2700 nm. Figures 7(a,b) show the optical transmission and reflection spectra for the four samples in the wavelength range of 650-2700 nm. The obtained spectra exhibit a typical behavior with a well-defined absorption band edge. In this part of the spectrum, metal-free electrons reflectivity is very small which is also affected by light absorption from integrand electronic transitions [11]. As Co thickness increased, more bound electrons became available for excitation, hence a decrease in transmittance. Instead, at long wavelengths, region-free electron reflectivity is high [12], and the optical transmittance diminution with increased Co thickness can be justified by the simple classical Drude model. The thin films have high reflectivity in the wavelength above 700 nm, proving that copper is a good candidate as a substrate for photo-thermal applications. To evaluate the optical absorption properties of the four Cu and Cu samples with Co different thicknesses, the UV-Vis-NIR absorption spectra were investigated. The optical band gap ( $E_g$ ) energy of the thin films was determined using the formula  $A=1-T-R$ . Figure 7(c) shows the optical absorbance spectra of Cu and Cu-doped Co thin films. All samples display strong light absorption over the entire spectral range, suggesting that they could be all light absorber materials. The results revealed that the Cu with 70 nm Co had a very broad absorption band and higher intensity. The absorption peak of the Cu with 70 nm Co was located at 1134 nm. Followed by Co doping, a different enhanced capacity for light absorption was obtained; however, increasing the Cu thickness would reduce the absorption, as depicted in Figure 7(c).

A review of the transmission variation versus photon

wavelength reveals that the first derivative  $dT/d\lambda$  exhibits some peaks whose center  $\lambda_g$  can be related to the gap energy  $E_g=hc/\lambda_g$ . However, the width of these peaks does not correspond to an ideal material. In fact, for an ideal material, the transmission for wavelengths less than

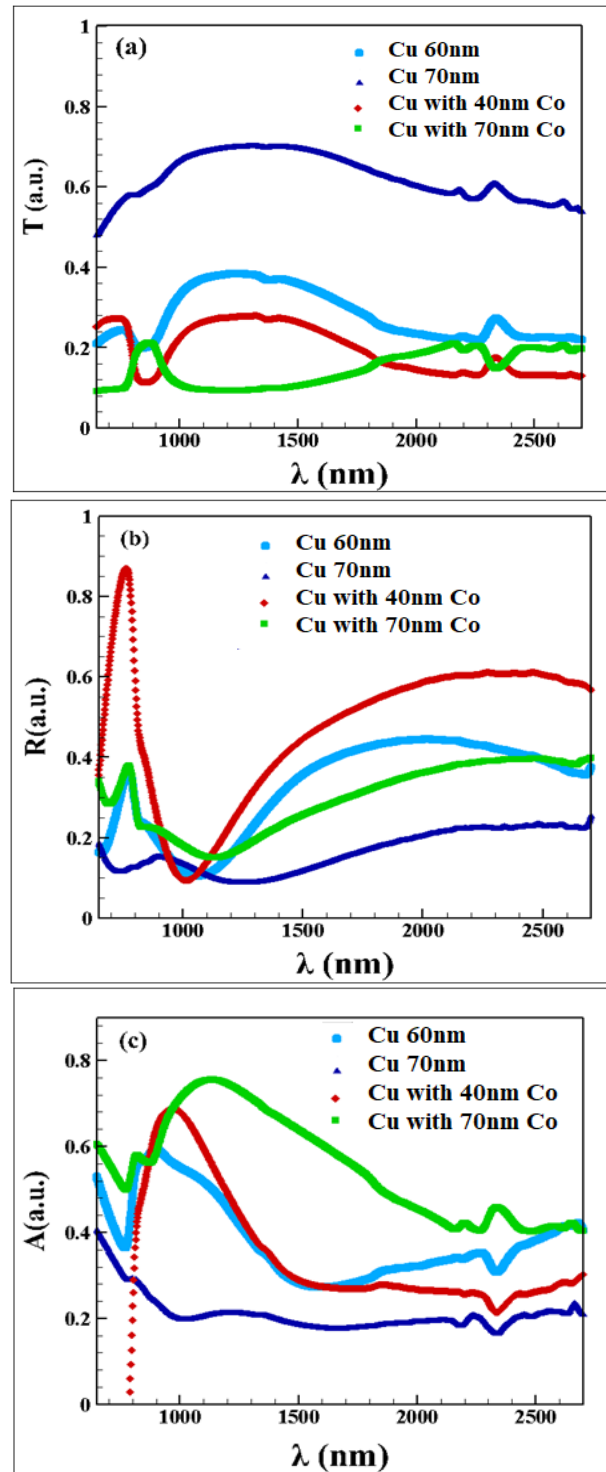


**Figure 7.** (a) Transmission spectra, (b) Reflection spectra, and (c) Absorbance spectra versus photon wavelength of the samples

$\lambda_g(E)$  is zero [13]. Therefore, to calculate the absorption band edge of the film, the first derivative of the optical reflection ( $dR/d\lambda$ ) should be estimated.

Figures 8(a,b) plot the curves of ( $dT/d\lambda$ ) and ( $dR/d\lambda$ ) versus wavelength. The values of the  $dT/d\lambda$  peaks were estimated to be 3.1 eV, 2.77 eV, 3.46 eV, and 2.88 eV for films of different thicknesses of copper and Cu-Co, respectively. The values of  $dR/d\lambda$  peaks were estimated to be 2.32 eV, 2.39 eV, 2.57 eV, and 2.15 eV for films Cu 60 nm, Cu 70 nm, Cu with 40 nm Co, and Cu with 70 nm Co over layer, respectively. The variations of the optical gap have a direct relationship with the absorption edge, concentration of the donor carrier, and impurity energy levels. Increasing the impurity of the energy levels caused a shift from the absorption edge to higher energy which in turn increased the  $E_g$  and NPs size as well.

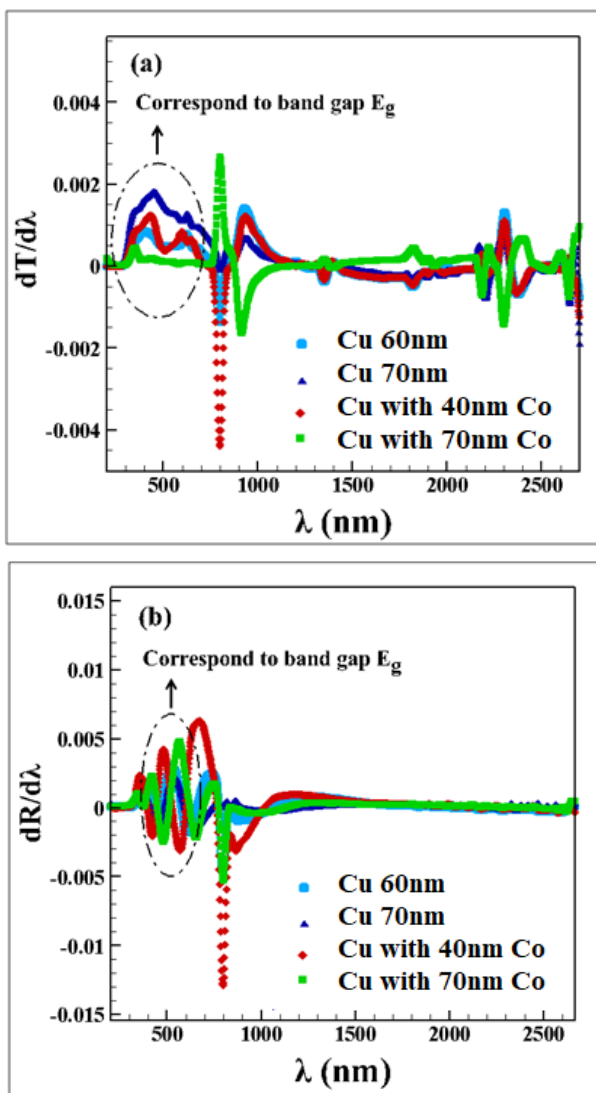


**Figure 8.** variations of (a)  $dR/d\lambda$  and  $dT/d\lambda$  versus (b) photon wavelength of the samples

The real and imaginary parts of the dielectric constant  $\sigma_1$  and  $\sigma_2$  were taken into account to predict the spectral behavior of the optical conductivity based on the following relations [13]:

$$\sigma^*(\omega) = \sigma_1(\omega) + i\sigma_2(\omega) \quad (4)$$

where

$$\sigma_1(\omega) = \omega\epsilon_2\epsilon_0 \quad \text{and} \quad \sigma_2(\omega) = \omega\epsilon_1\epsilon_0 \quad (5)$$

In the above relation,  $\omega$  stands for the angular frequency, and  $\epsilon_0$  the vacuum permittivity of the free space. The optical conductivity parameters  $\sigma_1(\omega)$  and  $\sigma_2(\omega)$  can be used to detect any further allowed integrand optical transitions. Figure 9 shows the dependence of the real and imaginary parts of the optical conductivity on the wavelength. According to the observations, the optical conductivity of films increased upon increasing energy. This increase results from the electrons excited by photon energy. The  $E_g$  values can be estimated from the cross-point between the curves of the real and imaginary parts of the optical conductivity to the photon energy axis. The optical conductivity does not follow any certain trend with atomic number ions in the complexes. The  $E_g$  value is estimated from the cross-point between the curves of the real and imaginary parts of the optical conductivity to the photon energy axis. The optical conductivity does not follow any certain trend with atomic numbering in the complexes.

Figure 9 shows the spectral behavior of the real and imaginary optical conductivities in the photon energy range 2. The optical energy band gap of the samples were obtained as 1.73 eV, 2.39 eV, 2.59 eV, and 2.02 eV, respectively.

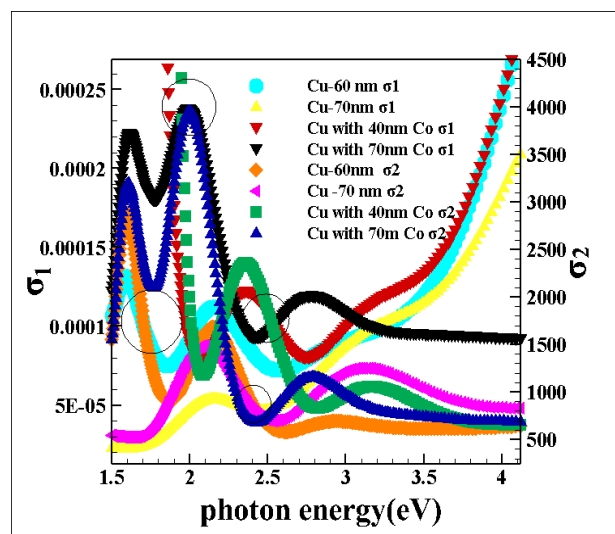


**Figure 9.** The dependency of  $\sigma_1(\omega)$  and  $\sigma_2(\omega)$  of the films as a function of the incident photon energy

Mott and Davis devised a formula to calculate the absorption coefficient  $\alpha(\nu)$  as a function of photon energy, as shown below [13]:

$$\alpha(\nu) = C(h\nu - E_{opt})^m / (h\nu) \quad (6)$$

In direct transitions, we have  $m=1/2$  and  $3/2$  for the allowed and forbidden transitions, respectively, while in indirect transitions, we have  $m=2$  or  $3$  for allowed and forbidden transitions, respectively. In this formula,  $C$  and  $E_{opt}$  are the constant and optical band gaps, respectively. The type of transition can be determined based on the value of  $m$  obtained from the applied differential method [13].

$$d[\text{Ln}(\alpha h\nu)]/d[h\nu] = m/(h\nu - E_{opt}) \quad (7)$$

The differential curve has a discontinuity at the particular energy value (which gives the optical band gap  $E_{opt}$ ). In order to determine the transition type, the  $E_{opt}$  values are calculated by extrapolation of the linear parts of  $(\alpha h\nu)^{1/m}$  versus  $h\nu$  curves to  $(\alpha h\nu)^{1/m}=0$  for different values of  $m$ . A comparison was made between the differential curve and  $E_g$  values considering the different values of  $m$  to determine the transition type.

Figure 10(a) shows the plot of  $d(\alpha h\nu)/d(h\nu)$  versus  $h\nu$ . In the plot of  $d(\alpha h\nu)/d(h\nu)$  versus  $h\nu$ , there are a number of peaks that are cross-point to the sensual energy, and photon energy values in the films remain nearly constant. The cross-point of  $d(\alpha h\nu)/d(h\nu)$  curves, where the peak is at about at 2.7, result in the  $E_g$  values of 2.68 eV, 2.76 eV, 2.85 eV, and 2.73 eV for the Samples 1 to 4, respectively.

Figure 10(b) illustrates the plot of  $\text{Ln}(\alpha h\nu)$  versus  $\text{Ln}(h\nu - E_g)$ .

In addition, the Wemple–DiDomenico single oscillator model was used to study the dispersion behavior of the refractive index, as expressed by the relation given below [14]:

$$n^2(h\nu) = 1 + E_d E_o / E_o^2 - (h\nu)^2 \quad (8)$$

where  $n$  is the refractive index,  $h$  the Planck constant,  $\nu$  the frequency,  $h\nu$  the photon energy,  $E_o$  the average excitation energy for electronic transitions, and  $E_d$  the dispersion energy which is a measure of the strength for the interband optical transitions.

Figure 11(a) shows the graph between  $(n^2-1)^{-1}$  versus  $(h\nu)^2$  based on which, the straight-line fitting gives the intercept  $(E_o/E_d)$  and slope  $(E_o E_d)^{-1}$ . Table 1 shows the values of  $E_o$  and  $E_d$  from the slope and intercept. As proposed by Tanaka, the first approximate value of the  $E_g$  was also derived from the WDD model based on  $2E_g \approx E_o$ . An increase in  $E_o$  in indicative of an increase in

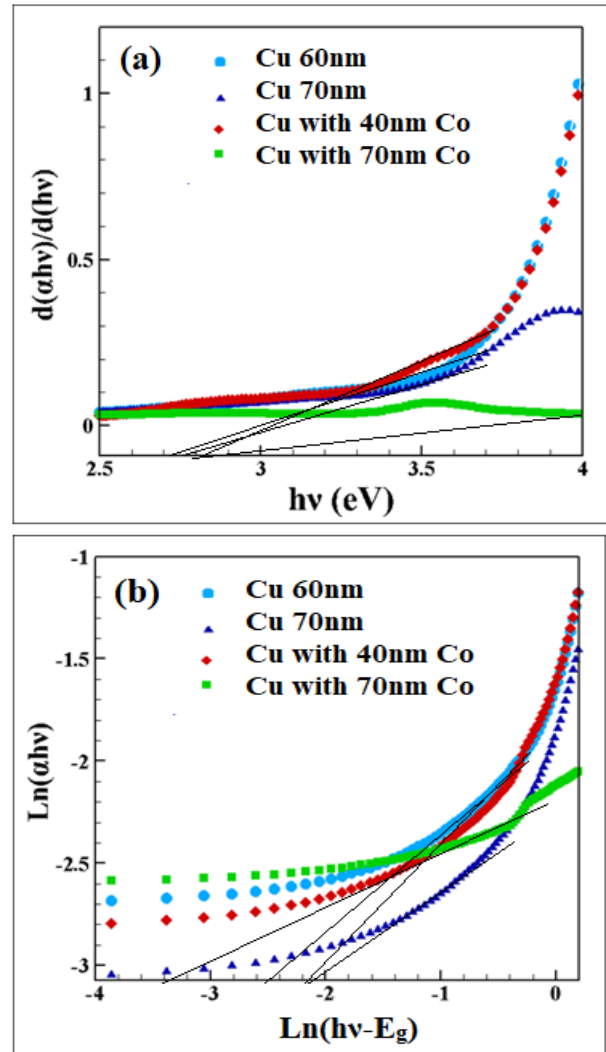


**Figure 10.** (a) variation of  $d(\alpha h\nu)/d(h\nu)$  of the films versus  $h\nu$  and (b) Variation of  $\text{Ln}(\alpha h\nu)$  versus  $\text{Ln}(h\nu - E_g)$  of the samples

the interband transition. It also corresponds to the distance between the center of gravity of the valence and conduction bands. Further, an increase in  $E_d$  with annealing temperature is due to the increase in the diffusion of atoms to the interstitial sites.

There is also an important parameter called the oscillator strength  $f$  of the films that can be obtained as:

$$f = E_o E_d \quad (9)$$

Table 1 presents the values of oscillator strength, indicating an increase in the strength with annealing. Obviously, this value is almost in agreement with that obtained from the Tauc extrapolation model. The static refractive index  $E_o$  (incident photon energy equal zero) of all the studied films was obtained through the following equation:

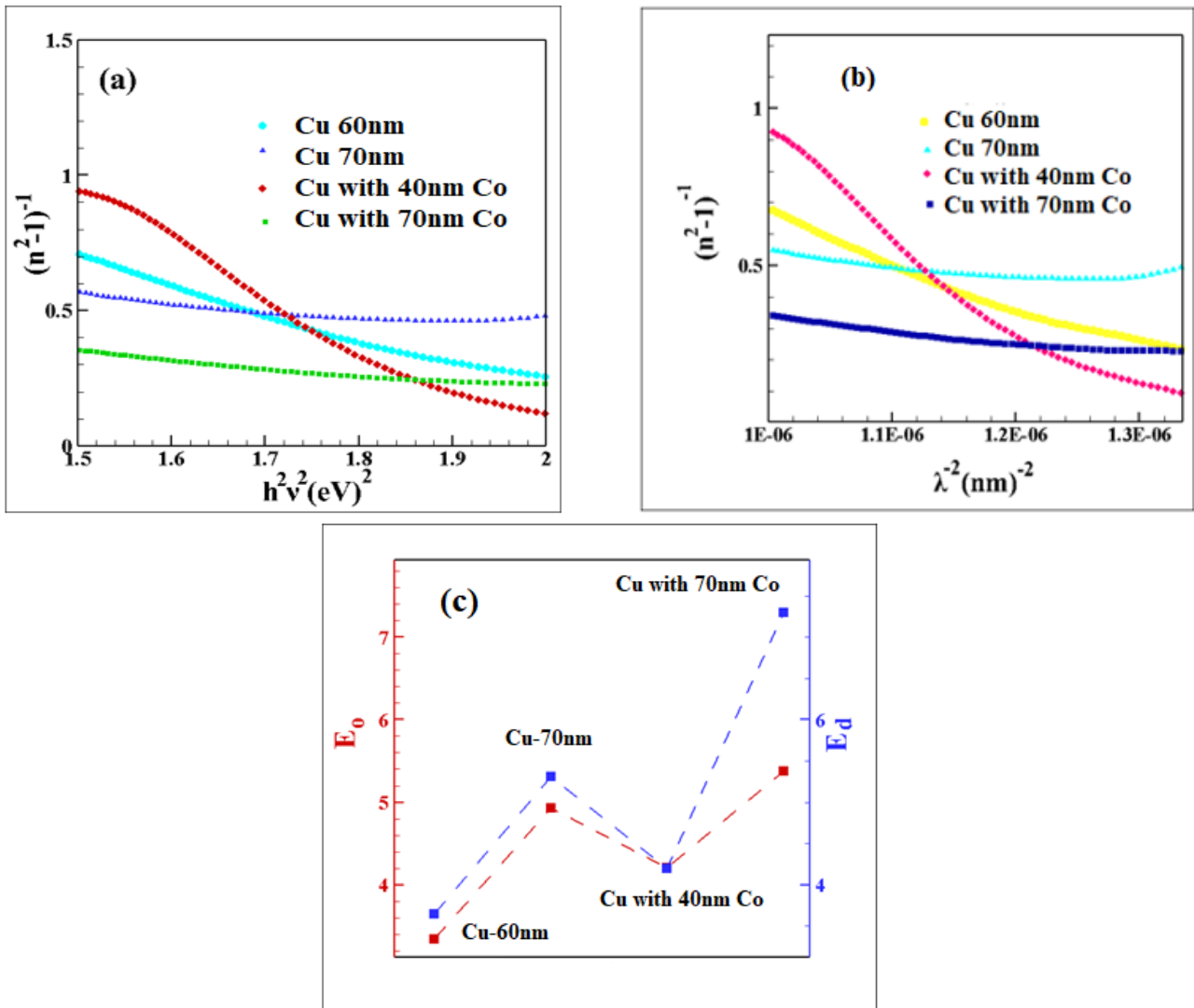


**Figure 11.** (a) The plots of  $(n^2-1)^{-1}$  versus  $(hv)^2$ , (b) The plots of  $(n^2-1)^{-1}$  versus  $\lambda^{-2}$ , and (c) the variation of both the  $E_o$  and  $E_d$  with the doping and thickness of the samples

**Table 1.** The Wemple–Didomenico optical dispersion parameters of the samples

Samples	$E_o$ (eV)	$E_d$ (eV)	$\lambda_o$ ( $\mu\text{m}$ )	$n_o$	$M_{-1}$	$M_{-3}$ ( $\text{eV}^{-2}$ )	$S_o$ ( $\mu\text{m}$ ) <sup>2</sup>	$f=E_oE_d$ (eV) <sup>2</sup>
Cu- 60 nm	3.34	3.64	0.41	0.30	3.05	1.089	0.68	12.158
Cu- 70 nm	4.93	5.31	0.67	0.23	3.26	1.077	1.47	26.178
Cu with 40 nm Co	4.21	4.20	0.20	0.41	3.35	0.998	1.18	17.682
Cu with 70 nm Co	5.38	7.30	0.10	0.25	3.12	1.357	1.10	39.274

$$n_0^2 = (1 + E_d/E_o) \tag{10}$$

Average oscillator wavelength  $\lambda_o$  and oscillator length strength  $S_o$  of all the studied films were obtained from the following equation:

$$(n_0^2-1/n^2-1) = 1 - \frac{\lambda_o}{(\lambda)^2} \tag{11}$$

Average oscillator wavelength values were calculated from the linear parts of the plots of  $1/(n^2-1)$  versus  $\lambda^{-2}$  (Figure 11(b)). Relation (11) can also be written as:

$$n^2-1 = [S_o/1-(\lambda_o/\lambda)^2]\lambda_o^2 \quad (12)$$

where  $S_o=(n_o^2-1)/\lambda_o^2$  and the optical moments  $M_{-1}$  and  $M_{-3}$  of the optical spectra for all films are written as follows:

$$E_o^2 = \frac{M_{-1}}{M_{-3}}, E_d^2 = \frac{M_{-1}^3}{M_{-3}} \quad (13)$$

Based on the above analyses, the values of the indirect band gap for the for the Cu 60 nm, Cu 70 nm, Cu with 40 nm Co, and Cu with 70 nm Co thin films were obtained as 1.73 eV, 2.39 eV, 2.51 eV, and 2.02 eV, respectively. The values of the indirect band gap calculated through

the Taus model were in conformity with the calculated band gap using WDD analyses. Table 1 lists the dispersion parameters obtained from the WDD model.

Scanning Electron Microscope (SEM) is a type of electron microscope that produces images of a sample by scanning the surface with a focused beam of electrons. The SEM images of Cu with the thickness of 70 nm and Cu-Co bilayers with 40 nm Co are shown in Figures 12(a,b), respectively.

The given images of both samples are in good agreement with the presented AFM images. According to these images, the obtained cobalt nanocrystals have an approximately spherical shape with an average diameter less than 80 nm [15,16].

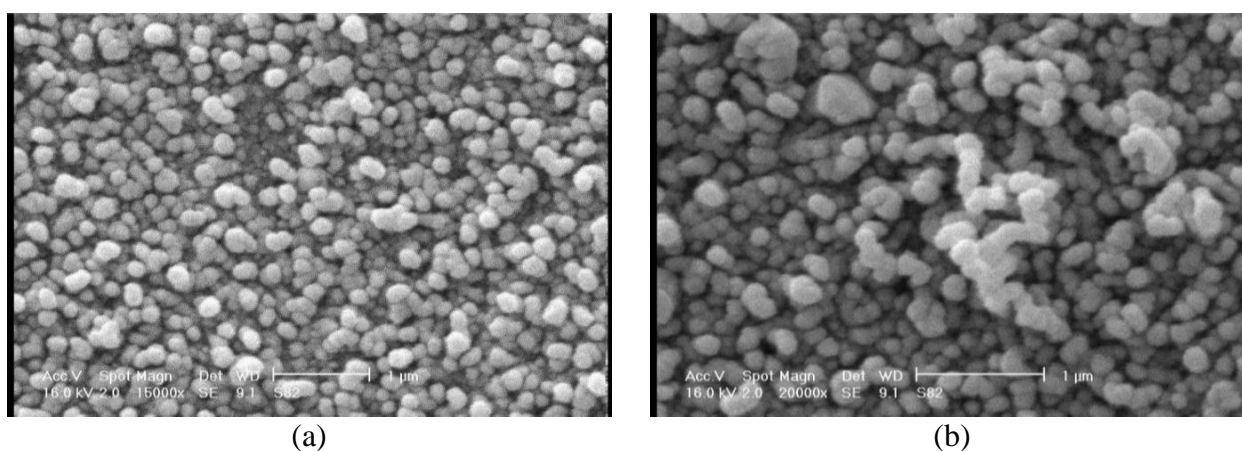


**Figure 12.** SEM images of samples (a) Cu and (b) Cu-Co bilayers with 40 nm Co

#### 4. CONCLUSION

The lateral size values of the NPs for the films with 60 nm Cu, 70 nm Cu, and Cu with 40 nm Co, and 70 nm Co were obtained as about 40.94, 42.35, 43.76, and 39.53 nm, respectively. The shown SEM images of both samples were in good agreement with the obtained AFM images. The cross-point of  $d(\alpha hv)/d(hv)$  curves resulted in the  $E_g$  values of 2.68 eV, 2.76 eV, 2.85 eV, and 2.73 eV for the samples, respectively, at the peak of about 2.7. No certain trend was observed in the optical conductivity with atomic numbering in the complexes. For films Cu 60 nm, Cu 70 nm, Cu with 40 nm Co, and Cu with 70 nm Co, the values of  $dT/d\lambda$  peaks were estimated to be 3.1 eV, 2.77 eV, 3.46 eV, and 2.88 eV, respectively, while the values of  $dR/d\lambda$  peaks were estimated to be 2.32 eV, 2.39 eV, 2.57 eV, and 2.15 eV, respectively. The absorption peak of the Cu with 70 nm Co was observed at 1134 nm. Followed by Co doping, a different enhanced capacity for light absorption was witnessed; however, increasing the copper thickness reduced absorption.

#### ACKNOWLEDGMENTS

The authors would like to acknowledge the financial support of Malayer University for this research.

#### REFERENCES

1. Arman, A., Țălu, Ș., Luna, C., Ahmadpourian, A., Naseri, M., Molamohammadi, M., "Micromorphology characterization of copper thin films by AFM and fractal analysis", *Journal of Materials Science: Materials in Electronics*, Vol. 26, No. 12, (2015), 9630-9639. <https://doi.org/10.1007/s10854-015-3628-5>
2. Sobola, D., Țălu, Ș., Soleymani, S., Grmela, L., "Influence of scanning rate on quality of AFM image: Study of surface statistical metrics", *Microscopy Research and Technique*, Vol. 80, No. 12, (2017), 1328-1336. <https://doi.org/10.1002/jemt.22945>
3. El Kasmi, A., Waqas, M., Mountapmbeme Koutou, P., Tian, Z., "Cu-promoted cobalt oxide film catalyst for efficient gas emissions abatement", *Journal of Thermal Science*, Vol. 28, No. 2, (2019), 225-231. <https://doi.org/10.1007/s11630-019-1093-9>
4. Dalouji, V., Rahimi, N., S Goudarzi, S., "Skin depth, optical density, electron-phonon interaction, steepness parameter, band tail width, carriers transitions and dissipation factors in Cu-Co bilayer films", *Mechanics of Advanced Materials and*

- Structures*, (2021), 1-14. <https://doi.org/10.1080/15376494.2021.1983678>
5. Jiang, W., Shen, L., Xu, M., Zhu, J., Tian, Z., "Roughness, Hardness and Giant Magneto Resistance of Cu/Co Multilayers Prepared by Jet electrochemical deposition", *International Journal of Electrochemical Science*, Vol. 13, (2018), 9669-9680. <https://doi.org/10.20964/2018.10.24>
  6. Souza, T. M. D., Lago, D. C. B. D., Senna, L. F. D., "Electrodeposition of Co-rich Cu-Co alloys from sodium tartrate baths using direct (DC) and single pulsed current (SPC)", *Materials Research*, Vol. 22, No. 3, (2019), e20180272. <https://doi.org/10.1590/1980-5373-MR-2018-0272>
  7. Li, B., Du, S., Mei, T., "Pulse electrodeposited Ni-Cu/TiN-ZrO<sub>2</sub> nanocomposite coating: microstructural and electrochemical properties", *Materials Research Express*, Vol. 6, No. 9, (2019), 096433. <https://doi.org/10.1088/2053-1591/ab31e9>
  8. Ghaderi, A., Shafiekhani, A., Solaymani, S., Tãlu, Ş., da Fonseca Filho, H. D., Ferreira, N. S., Matos, R. S., Zahrabi, H., Dejam, L., "Advanced microstructure, morphology and CO gas sensor properties of Cu/Ni bilayers at nanoscale", *Scientific Reports*, Vol. 12, No. 1, (2022), 1-9. <https://doi.org/10.1038/s41598-022-16347-4>
  9. Mozaffari, N., Solaymani, S., Achour, A., Kulesza, S., Bramowicz, M., Nezafat, N. B., Tãlu, S., Mozaffari, N., Rezaee, S., "New insights into SnO<sub>2</sub>/Al<sub>2</sub>O<sub>3</sub>, Ni/Al<sub>2</sub>O<sub>3</sub>, and SnO<sub>2</sub>/Ni/Al<sub>2</sub>O<sub>3</sub> composite films for CO adsorption: building a bridge between microstructures and adsorption properties", *The Journal of Physical Chemistry C*, Vol. 124, No. 6, (2020), 3692-3701. <https://doi.org/10.1021/acs.jpcc.9b11148>
  10. Rahimi, N., Dalouji, V., Souri, A., "Studying the optical density, topography, and structural properties of CZO and CAZO thin films at different annealing temperatures", *Advanced Ceramics Progress*, Vol. 6, No. 2, (2020), 17-23. <https://doi.org/10.30501/acp.2020.107466>
  11. Yu, S., Liu, Y., Zheng, H., Li, L., Sun, Y., "Improved performance of transparent conducting AZO/Cu/AZO multilayer thin films by inserting a metal Ti layer for flexible electronics", *Optics Letters*, Vol. 42, No. 15, (2017), 3020-3023. <https://doi.org/10.1364/OL.42.003020>
  12. Bhowmik, D., Bhattacharjee, S., "Optical, structural, and electrical properties of modified indium-tin-oxide (ITO) films on glass surface by low energy ion implantation", *Applied Physics A*, Vol. 128, No. 7, (2022), 605. <https://doi.org/10.1007/s00339-022-05746-z>
  13. Rahimi, N., Dalouji, V., Rezaee, S., "Effect of annealing processing on morphology, spectroscopy studies, Urbach disordering energy, and WDD dispersion parameters in Cu-Al doped zinc oxide films", *Journal of Dispersion Science and Technology*, Vol. 43, No. 7, (2022), 990-999. <https://doi.org/10.1080/01932691.2020.1847657>
  14. Dalouji, V., Abbasi, P., Rahimi, N., "Effect of annealing temperature on photoluminescence spectra, gap states using different models and optical dispersion parameters in copper-doped ZnO films", *Molecular Simulation*, Vol. 46, No. 18, (2020), 1542-1549. <https://doi.org/10.1080/08927022.2020.1856839>
  15. Hedayati, K., Azarakhsh, S., Ghanbari, D., "Synthesis and magnetic investigation of cobalt ferrite nanoparticles prepared via a simple chemical precipitation method", *Journal of Nanostructures*, Vol. 6, No. 2, (2016), 127-131. <https://doi.org/10.7508/jns.2016.02.004>
  16. Hedayati, K., Azarakhsh, S., Saffari, J., Ghanbari, D., "Photo catalyst CoFe<sub>2</sub>O<sub>4</sub>-CdS nanocomposites for degradation of toxic dyes: investigation of co-cativity and magnetization", *Journal of Materials Science: Materials in Electronics*, Vol. 27, No. 8, (2016), 8758-8770. <https://doi.org/10.1007/s10854-016-4900-z>

## AIMS AND SCOPE

*Advanced Ceramics Progress* (ACERP) as an ISC international journal is devoted to elucidating the fundamental aspects of chemistry and physics occurring at a wide range of oxide and nonoxide ceramics and composite materials and their processing, microstructure, properties, and applications. The journal provides a unique venue for publishing new exciting research, focusing on dynamic growth areas in this field.

## INSTRUCTIONS FOR AUTHORS

Submission of manuscript represents that it has neither been published nor submitted for publication elsewhere and is result of research carried out by author(s).

Authors are required to include a list describing all the symbols and abbreviations in the manuscript. Use of the international system of measurement units is mandatory.

- On-line submission of manuscripts results in faster publication process and is recommended. Instructions are given in the ACERP web site: [www.acerp.ir](http://www.acerp.ir)
- References should be numbered in brackets and appear in sequence through the text. List of references should be given at the end of the manuscript.
- Figures' captions are to be indicated under the illustrations. They should sufficiently explain the figures.
- Illustrations should appear in their appropriate places in the text.
- Tables and diagrams should be submitted in a form suitable for reproduction.
- Photographs and figures should be of high quality saved as jpg files (resolution > 600 dpi).
- Tables, illustrations, figures and diagrams will be normally printed in single column width (8 cm). Exceptionally large ones may be printed across two columns (17 cm).

## PAGE CHARGES AND REPRINTS

ACERP subscribers do not need to make any payment for publication and reprints.

## AUTHORS CHECKLIST

- Author(s), bio-data including academic degree, affiliation(s), ORCID(s), and e-mail addresses.
- Manuscript including title, abstract, key words, illustrations, tables with tables' captions, figures with figures' captions, acknowledgement, and list of references.
- MS Word files of the manuscript in the ACERP template and all figures (resolution > 600 dpi).
- Similarity check of the manuscript, copyright forms, and conflict of interest forms

Advanced Ceramics Progress,  
P.O. Box 31787-316, Meshkin Dasht, Alborz, I. R. Iran  
Materials and Energy Research Center, Imam Khomeini Blvd, Meshkin Dasht, Alborz, I. R. of Iran  
P.O. Box 14155-4777, Tehran, I. R. Iran  
No. 5, Ahuramazda St., Alvand Ave., Argentine Sq., Tehran, Tehran, I. R. of Iran

# Advanced Ceramics Progress

Volume 8, Number 3, Summer 2022

## CONTENTS

<b>Zahra Abdi</b> <b>Adrine Malek Khachatourian</b> <b>Ali Nemati</b>	Studying the Effect of Calcination on the Optical and Magnetic Properties of NiFe <sub>2</sub> O <sub>4</sub> @ZnO:Ti Nanoparticles	1-7
<b>Maryam Hajiebrahimi</b> <b>Sanaz Alamdari</b> <b>Omid Mirzaee</b> <b>Mohammad Tajally</b>	Luminescence Investigation of Ce Doped ZnO/CdWO <sub>4</sub> Nanocomposite	8-12
<b>Elmira Sadeghilar</b> <b>Soghra Mirershadi</b> <b>Farhad Sattari</b>	Design and Study of the Photodetection Performance of Photodetector Based on CH <sub>3</sub> NH <sub>3</sub> PbBr <sub>3</sub> Organic-Inorganic Hybrid	13-17
<b>Aida Faeghinia</b> <b>Touradj Ebadzadeh</b>	The Effect of Microwave Settings on HAp Sintering	18-21
<b>Ghader Hosseinzadeh</b>	Preparation of Nanocomposite of TiO <sub>2</sub> Nanoparticles and CuS Nanoflakes for Visible-Light Photocatalytic Decomposition of Nitenpyram Pesticide	22-28
<b>Vali Dalouji</b> <b>Nasim Rahimi</b> <b>Ali Reza Souri</b>	Cu/Co Bilayers: Study of the Surface Topography, Optical Dispersion Parameters, and Transitions of Carriers	29-38



Journal Home Page: [www.acerp.ir](http://www.acerp.ir)